

Non-hydrostatic computations of nearshore hydrodynamics

M.Sc. Thesis



R. P. M. Jacobs

Caption : An Australian beach where surfers ignore the danger sign because in fact the rip current is very useful in taking their surfboards beyond the breaker zone

Cover photograph by : Matthew Celia (2008)

Title : M.Sc. Thesis Delft University of Technology
Non-hydrostatic computations of nearshore hydrodynamics

Author : R. P. M. Jacobs

Date : June 2010

Graduating Committee : Prof. dr. ir. G. S. Stelling
Prof. dr. ir. J. A. Battjes
Dr. ir. M. Zijlema
Dr. ir. J. van Thiel de Vries
ir. P. B. Smit

Acknowledgements

This thesis concludes the M.Sc. Civil Engineering program at the Delft University of Technology. Writing this thesis was challenging, not only for the subject at hand, but also for the individual process one has to go through, which can feel quite lonely at times and requires a substantial amount of discipline.

Numerical modelling can be very frustrating at times but can also be very satisfying and, if the chronological order of both experiences is in the same order as above, one usually forgets the frustrating part immediately. My experience of numerical modelling is therefore an experience I cherish and something that I regard as very useful for my future career.

There are a number of people that I would like to thank for their guidance, help and support while writing this thesis. Firstly, I would like to thank my parents as they have always supported me in my studies and endeavors. Secondly, I would like to thank my girlfriend Sinéad who has always offered me positive encouragement.

Finally, I would like to thank my supervisor Pieter Smit who helped me overcome the many obstacles I encountered while writing this thesis. I would also like to extend my gratitude to the other members of the graduating committee who provided me with constructive criticism and recommendations.

To end, I would like to say that working on this thesis has given me a deeper insight into the career path I wish to take.

Robert Jacobs

June 2010

Abstract

The nearshore zone is an active zone that can be quite inhospitable to humans due to violent wave breaking and strong rip currents. Rip currents are shore normal jet-like currents that typically extend from near the shoreline out past the line of breaking waves. Observations have concluded that a rip current system generally consists of 4 parts. Part 1 is the shoreward mass transport due to the waves carrying water through the breaker zone in the direction of wave propagation. Part 2 is the movement of this water mass parallel to the coast known as a longshore current. Part 3 is the rip current itself, a seaward flow of water through a narrow rip channel. And part 4 is an alongshore movement outside the breaker zone of the expanding rip head.

With the use of the numerical model XBeach, in which a non-hydrostatic model based upon the numerical scheme as developed by *Stelling and Zijlema (2003)* was implemented, the fluid motions in the nearshore zone are simulated. The method of *Stelling and Zijlema* utilizes an edge based compact difference scheme for the approximation of the vertical gradient of the non-hydrostatic pressure. This ensures accurate wave breaking and dispersion characteristics, which is important for an accurate simulation of the nearshore hydrodynamics.

Two test cases are used to verify the model for replication of the hydrodynamics in the nearshore zone. The first case consists of irregular wave breaking in a laboratory barred surf zone. The second case is a wave induced and bathymetry driven rip current in a directional wave basin.

The numerical model is further developed with the addition of an eddy viscosity model and a non-reflecting boundary condition. With these additions the depth averaged model gave very satisfactory results for both cases.

The XBeach model is an accurate and efficient simulation package for the dynamics in the nearshore zone. This study shows that application to real world situations should give realistic and accurate results. Therefore the model could be applied in coastal engineering applications and in the research for energy extraction methods from wave induced currents.

Table of Contents

| | |
|---|-----|
| Acknowledgements | iii |
| Abstract | v |
| List of figures | xi |
| List of tables | xv |
| 1 Introduction..... | 1 |
| 1.1 Objective..... | 1 |
| 1.2 Readers guide..... | 2 |
| 2 Nearshore Hydrodynamics..... | 3 |
| 2.1 Introduction | 3 |
| 2.2 Nearshore zone..... | 3 |
| 2.3 Wave propagation | 4 |
| 2.4 Rip Current Systems..... | 4 |
| 2.4.1 Introduction | 4 |
| 2.4.2 Rip current parts..... | 5 |
| 2.4.3 Rip current characteristics..... | 7 |
| 2.4.4 Rip current forcing mechanisms..... | 8 |
| 2.4.5 Rip current flow..... | 12 |
| 3 Numerical modelling of nearshore hydrodynamics..... | 15 |
| 3.1 Introduction | 15 |
| 3.2 Nearshore modelling..... | 15 |
| 3.3 Boussinesq models..... | 15 |
| 3.4 Non-hydrostatic models | 16 |
| 4 Model description | 17 |
| 4.1 Introduction | 17 |
| 4.2 Governing equations | 17 |
| 4.3 Grid schematization..... | 18 |
| 4.4 Boundary conditions..... | 20 |
| 4.4.1 Free surface and bottom | 21 |
| 4.4.2 Closed boundaries | 21 |
| 4.4.3 Open boundary..... | 21 |
| 4.5 Wave breaking | 23 |

| | | |
|-------|---|----|
| 4.6 | Smagorinsky eddy viscosity model..... | 24 |
| 4.6.1 | Discretisation of the Smagorinsky model..... | 25 |
| 5 | Validation and verification | 26 |
| 5.1 | Irregular wave breaking in a laboratory barred surf zone..... | 26 |
| 5.1.1 | Introduction | 26 |
| 5.1.2 | Boundary condition | 27 |
| 5.1.3 | Setup..... | 29 |
| 5.1.4 | Computations without viscosity | 29 |
| 5.1.5 | Computations with a constant eddy viscosity..... | 32 |
| 5.1.6 | Computations with a constant eddy viscosity and a new boundary condition..... | 34 |
| 5.1.7 | Computations with a Smagorinsky eddy viscosity model..... | 36 |
| 5.2 | Experiments on rip currents and nearshore circulation..... | 41 |
| 5.2.1 | Introduction | 41 |
| 5.2.2 | Topography | 42 |
| 5.2.3 | Boundary conditions | 42 |
| 5.2.4 | Numerical setup..... | 43 |
| 5.2.5 | Results | 44 |
| 5.3 | Conclusions | 52 |
| 6 | Conclusions and recommendations..... | 54 |
| 6.1 | Conclusions | 54 |
| 6.1.1 | Numerical model..... | 54 |
| 6.1.2 | Application to the nearshore zone..... | 54 |
| 6.2 | Recommendations..... | 55 |
| 6.2.1 | Numerical model..... | 55 |
| 6.2.2 | Application to the nearshore zone..... | 55 |
| | List of main symbols | 56 |
| | Bibliography..... | 58 |
| A | Nearshore hydropower | 62 |
| A.1 | Introduction | 62 |
| A.2 | Rip current..... | 62 |
| A.3 | Tidal power | 69 |
| A.4 | Conclusion | 70 |
| B | Derivation of the depth averaged equations..... | 71 |

| | | |
|-----|---|----|
| B.1 | Introduction | 71 |
| B.2 | Navier-Stokes equations..... | 71 |
| B.3 | Simplifications | 71 |
| B.4 | Pressure decomposition | 72 |
| B.5 | Free surface equation | 73 |
| B.6 | Depth averaged momentum equations | 74 |
| C | Discretisation | 77 |
| C.1 | Global continuity equation..... | 77 |
| C.2 | Local continuity equation..... | 78 |
| C.3 | Horizontal momentum equations..... | 78 |
| C.4 | Vertical momentum equation..... | 80 |

List of figures

| | |
|--|----|
| Figure 2-1: The nearshore zone (*)..... | 3 |
| Figure 2-2 Rip current structure (*)..... | 5 |
| Figure 2-3: Longshore current (*)..... | 6 |
| Figure 2-5: Rip current process: cusped beach (*)..... | 7 |
| Figure 2-6: Rip current spacing vs. velocity (*)..... | 8 |
| Figure 2-7: Longshore variation in wave-setup (*)..... | 9 |
| Figure 2-8: Surf zone bathymetric features (*)..... | 11 |
| Figure 2-9: Rip current through gap in sandbar (small figure is a front view) (*)..... | 12 |
| Figure 4-1: Horizontal location of variables (#)..... | 19 |
| Figure 4-2: Vertical location of variables (#)..... | 19 |
| Figure 4-3: Horizontal domain Ω in relation to the global domain (#)..... | 20 |
| Figure 5-1: Snapshot of the computation..... | 26 |
| Figure 5-2: Water wave theories and their applicability..... | 28 |
| Figure 5-3: Computed (solid line) and measured (circles) significant wave heights (top panel) and mean zero-crossing periods (bottom panel) along the flumes (simulation without viscosity)..... | 30 |
| Figure 5-4: Computed (red line) and measured (blue line) energy density spectra at different stations in the flume. All spectra use equally spaced frequency intervals..... | 31 |
| Figure 5-5: Computed wave-setup (red line) and the measured wave-setup (circles)..... | 32 |
| Figure 5-6: Computed (solid line) and measured (circles) significant wave heights (top panel) and mean zero-crossing periods (bottom panel) along the flume (simulation with a constant eddy viscosity)..... | 32 |
| Figure 5-7: Computed (red line) and measured (blue line) energy density spectra at different stations in the flume. Computation with a constant eddy viscosity..... | 33 |

| | |
|--|----|
| Figure 5-8: Computed (solid line) and measured (circles) significant wave heights (top panel) and mean zero-crossing periods (bottom panel) along the flume (simulation with a constant eddy viscosity and a new boundary condition) | 34 |
| Figure 5-9: Computed (red line) and measured (blue line) energy density spectra at different stations in the flume (simulation with a constant eddy viscosity and a new boundary condition) | 35 |
| Figure 5-10: Computed wave-setup (red line) and the measured wave-setup (circles) (simulation with a constant eddy viscosity and a new boundary condition)..... | 36 |
| Figure 5-11: Computed (solid line) and measured (circles) significant wave heights (top panel) and mean zero-crossing periods (bottom panel) along the flume (simulation with Smagorinsky viscosity model and coarser grid)..... | 37 |
| Figure 5-12: Computed (solid line) and measured (circles) significant wave heights (top panel) and mean zero-crossing periods (bottom panel) along the flume (simulation with Smagorinsky eddy viscosity and denser grid)..... | 38 |
| Figure 5-13: Computed (solid line) and measured (circles) mean period along the flume (simulation with Smagorinsky eddy viscosity and denser grid) | 38 |
| Figure 5-14: Computed (red line) and measured (blue line) energy density spectra at different stations in the flume (simulation with the Smagorinsky eddy viscosity model) | 39 |
| Figure 5-15: Computed wave-setup with the Smagorinsky eddy viscosity model (red line) and the measured wave-setup (circles)..... | 40 |
| Figure 5-16: Comparison of the surface elevation between the computation (red line) and the measurements (blue line) | 40 |
| Figure 5-17: Topography of the wave basin | 42 |
| Figure 5-18: Wave gauge locations (left) and current meter locations (right) for test B. | 43 |
| Figure 5-19: Time series of the measured surface elevation and the computed cross-shore velocity at the most offshore wave gage. | 43 |
| Figure 5-20: Run averaged flow field | 44 |

| | |
|--|----|
| Figure 5-21: Snapshots of vorticity and velocity vectors averaged over two wave periods from the simulation. Red represents negative and blue represents positive vorticity. Only the upper half of the computational domain is shown..... | 46 |
| Figure 5-22: Run averaged velocity vectors from experimental data (blue vectors) and simulation (red vectors)..... | 47 |
| Figure 5-23: Comparison of time-averaged modelled wave height (line) to experimental data (asterisk)..... | 48 |
| Figure 5-24: Comparison of time-averaged modelled mean water level (line) to experimental data (asterisk)..... | 49 |
| Figure 5-25: Comparison of time-averaged cross-shore currents (line) to experimental data (asterisk)..... | 50 |
| Figure 5-26: Comparison of time-averaged modelled cross-shore currents (line) in the channel to experimental data (asterisk)..... | 51 |
| Figure 5-27: Comparison of time-averaged modelled longshore currents (line) to experimental data (asterisk)..... | 52 |
| Figure A-1: Run averaged flow field with amended topography..... | 64 |
| Figure A-2: Comparison of time-averaged modelled cross-shore currents with amended topography (blue line) to modelled cross-shore currents with original topography (red line) ... | 65 |
| Figure A-3: Snapshots of vorticity and velocity vectors averaged over two wave periods from the simulation. Red represents negative and blue represents positive vorticity. Only the upper half of the computational domain is shown..... | 65 |
| Figure A-4: Comparison of time averaged modelled longshore currents with amended topography (blue line) to modelled longshore currents with original topography (red line)..... | 66 |
| Figure A-5: Comparison of time-averaged modelled wave height with amended topography (blue line) to modelled wave height with original topography (red line)..... | 66 |
| Figure A-6: run averaged flow with single rip channel..... | 67 |

Figure A-7: Comparison of time-averaged modelled cross-shore currents with amended topography with two channels (blue line) to modelled cross-shore currents with single channel (red line)..... 68

Figure A-8: Water level differences due to presence of a 30 km long dam at IJmuiden during MHW and spring tide (UNESCO-IHE)..... 70

Figure B-9: Coordinate system used..... 73

The source of all the figures denoted with an asterisk is the COMET® Website at <http://meted.ucar.edu/> of the University Corporation for Atmospheric Research (UCAR), sponsored in part through cooperative agreement(s) with the National Oceanic and Atmospheric Administration (NOAA), U.S. Department of Commerce (DOC). ©1997-2010 University Corporation for Atmospheric Research.

The source of all the figures denoted with the number sign is *Smit* (2008).

List of tables

| | |
|---|----|
| Table 1: Field characteristics of rip currents..... | 13 |
| Table 2: Measured wave conditions..... | 27 |

1 Introduction

The nearshore zone is an active zone that can be quite inhospitable to humans due to violent wave breaking and strong rip currents. The strength and dynamics of rip currents are usually underestimated and not understood by many people who encounter these currents. In saying this, rip currents account for more than 80% of lifeguard rescue efforts, and are the number one natural hazard in the state of Florida, USA. More people fall victim to rip currents in Florida, than to lightning, hurricanes, and tornadoes (*Lascodey*, 1998; *Luschine*, 1991). Also in Australia, with its vast coastline, rip currents are found to form a major threat to bathers around the country, where they are responsible for more than 90% of all surf rescues and most drownings (*Short*, 1999). It is therefore important to not only better understand this phenomenon but to also be able to predict their occurrence and strength.

The study of nearshore dynamics is also important for coastline development, harbors and inlets as the nearshore zone processes have a dominant influence on navigation and accessibility which in turn have a significant impact on the economic and environmental interests of our society. In general, the coastal engineer is concerned with the fluid motions in the nearshore zone that interact with structures, boats and the coastline. It is therefore of importance for the coastal engineer to be able to predict these fluid motions in the nearshore zone.

Nearshore dynamics are very complex. Due to this complexity and the non-linearity of the mathematical equations associated, a principal tool used for the simulation of nearshore dynamics are numerical models. A popular way to model rip currents is to use the extended Boussinesq equations (*Chen et al.*, 1999; *Madsen et al.*, 1997a; *Wei et al.*, 1995). Fully coupled wave/current interaction is taken into account by the Boussinesq equations. However, a well known drawback of Boussinesq-type modelling is the assumption of an irrotational and inviscid flow. The consequence of this is that neither the interaction of waves with rotational currents nor the effects of viscosity on the wave motion can be simulated.

An alternative method to model these incompressible turbulent fluid flows involving gravity waves is based on the time-dependent three-dimensional Navier-Stokes equations. This is the method of choice for this thesis which is incorporated into the XBeach program (*Roelvink et al.*, 2009).

1.1 Objective

With the use of the numerical model XBeach, in which a non-hydrostatic model based upon the numerical scheme as developed by *Stelling and Zijlema* (2003) was implemented, the objective is to accurately simulate the fluid motions in the nearshore zone. Two test cases will be used to verify the model for replication of the dynamics in the nearshore zone. The first case consists of irregular wave breaking in a laboratory barred surf zone. The second case is a wave induced and bathymetry driven rip current.

1.2 Readers guide

The outline of this thesis is organized as follows: In Chapter 2 a literature review is carried out briefly highlighting the nearshore zone dynamics that play a role in a rip current system, and an investigation of the dynamics of a rip current system is undertaken. Chapter 3 is dedicated for the literature review of numerical models that are currently or have been of importance for simulations of fluid dynamics in the nearshore zone.

Subsequently the numerical model that is used for the research in this thesis is presented in Chapter 4. In Chapter 5 the model is validated and verified for the nearshore dynamics using the two cases as outlined above in the objectives. Chapter 6 will present the conclusions and recommendations resulting from this study.

In Appendix A the model is applied to cases for energy generation from the ocean in the nearshore zone. In this Appendix a number of ideas that transform wave energy into a current and utilize this current for electricity generation will be discussed. Results of the numerical model for these particular cases will be presented and used as material for discussion.

In Appendix B the derivation of the governing equations of the numerical model from fundamental equations is presented, and in Appendix C the discretisation technique used in the numerical model XBeach is presented.

2 Nearshore Hydrodynamics

2.1 Introduction

The nearshore hydrodynamics include the transformation of wind-generated deep water waves into shallow water waves and then, due to breaking, into motions of different types and scales. The shallow water waves transform into small-scale turbulence, larger-scale coherent vortical motions, low-frequency waves, and steady flows. The hydrodynamics only include the fluid motions and not the processes of sediment transport and morphological evolution. For short-term fluid computations it is allowed to ignore these processes because the transported sediment only has a weak influence on the hydrodynamics.

The wave dynamics in the nearshore environment are only briefly described. If the reader wishes a more comprehensive introduction into nearshore dynamics and more specifically wave dynamics one is referred to the work of *Battjes (1988)*, *Holthuijsen (2007)*, and *Dingemans (1997)*. The nearshore circulation system, also known as a rip current system, will be more thoroughly described.

2.2 Nearshore zone

The nearshore zone consists of four defined regions where the nearshore zone processes take place. In the Figure 2-1 these regions are highlighted.

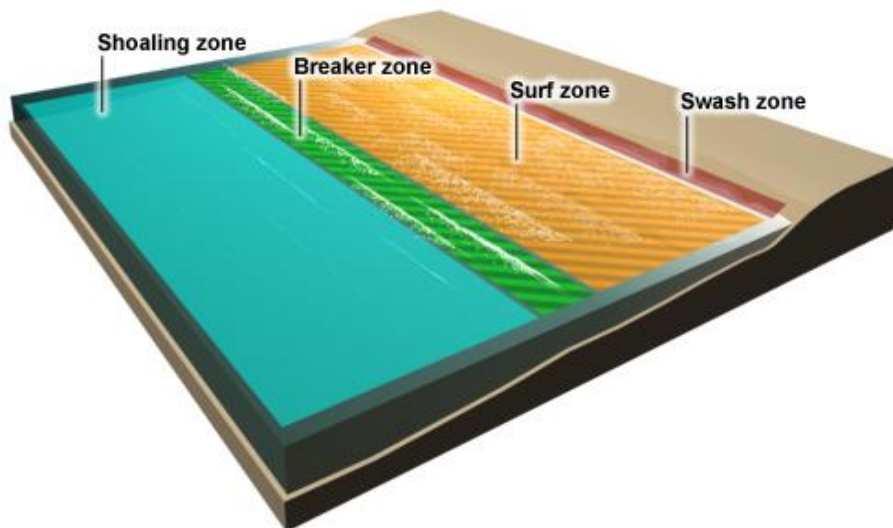


Figure 2-1: The nearshore zone (*)

The shoaling zone is the region where a wave passes from deep into shallow water. In this zone the water depth is less than half the wavelength. The vertical orientation of the wave changes as it begins to feel the effect of the bottom. As the wave nears the shore, its steepness increases and the wave eventually breaks.

The point where the wave begins to break is known as the breaking point. This is not to say that all waves begin to break in the same location. This location is dependent on wave height

variation. The breaker zone is where the majority of waves reach their steepness limit for a given wave spectrum. After the wave begins to break, it enters the surf zone where water is transported toward the beach in the form of smaller, broken waves known as bores. These bores can be thought of as continuously breaking waves. As bores reach the beach, water particles are pushed onshore and then retreat seaward. This area of run-up and backwash of water is known as the swash zone.

2.3 Wave propagation

Once a wave with a certain frequency and amplitude is generated it will propagate with a certain speed and direction. These properties will remain the same over a very long distance as long as the properties of the medium in which the wave travels will remain the same. However, if the wave with a certain wave length encounters a sloping seabed with decreasing depth, and the wavelength is of the same order as the depth, the amplitude and direction will be affected by the limited water depth. The propagation of a wave is thereby affected and the wave will start to deform. This effect can be described by the linear wave theory. The equations derived from the linear theory are applicable for waves with relatively low amplitude. When waves grow and steepen, they become nonlinear and the linear theory is not applicable anymore. However, in case the linear theory no longer holds, nonlinear theories are available such as the Stokes wave theory, cnoidal wave theory, and the stream-function theory. If the reader wishes more explanation on these theories, the book of *Holthuijsen* (2007) is a good starting point for further exploration.

The phenomenon of waves changing in longitudinal direction (i.e. in the direction of propagation) due to variation in the group velocity in that direction is called shoaling, and the result is either an increase or decrease in wave amplitude. If the phase speed is changed along the wave crest because of a variable depth along the wave crest, the wave will turn towards the shallower water. This process is called refraction. Another phenomenon is diffraction, which is caused by sudden change of amplitude along a wave crest. This variation in amplitude is usually caused by a structure and causes the wave to turn towards the region with lower amplitude. All these processes are of importance in the dynamics of the nearshore zone and the rip currents that can occur in this region. In the following paragraph the rip current system will be further investigated.

2.4 Rip Current Systems

2.4.1 Introduction

Rip currents are shore normal jet-like currents that typically extend from near the shoreline out past the line of breaking waves. They usually occur on gentle sloping beaches exposed to large oceanic swell. The rip current system is a horizontal circulation cell of mass transport. Mass transport as a concept is used in one of the first attempts to explain rip current systems. It was opted that the onshore mass transport by waves over an alongshore bar most efficiently exits through a narrow, usually morphodynamically, eroded rip channel to form a strong narrow current (*Munk*, 1949). This current, that was firstly scientifically observed by *Shepard et al.* (1941), was found to get stronger and also the seaward distance the rips would extend

increased when the height of the incoming waves increased. *Shepard* observed that the rip currents occurred at the center of beach cusps and on either side of regions in which the breaker height is large. At a later stage a more comprehensive series of field measurements were depicted by *Shepard and Inman* (1950). The observations concluded that a rip current system generally consisted of 4 parts. Part 1 is the shoreward mass transport due to the waves carrying water through the breaker zone in the direction of wave propagation. Part 2 is the movement of this water mass parallel to the coast as an alongshore current. Part 3 is the rip current itself, a seaward flow of water through a narrow rip channel. And part 4 is an alongshore movement outside the breaker zone of the expanding rip head. In the following figure the rip current structure is given.

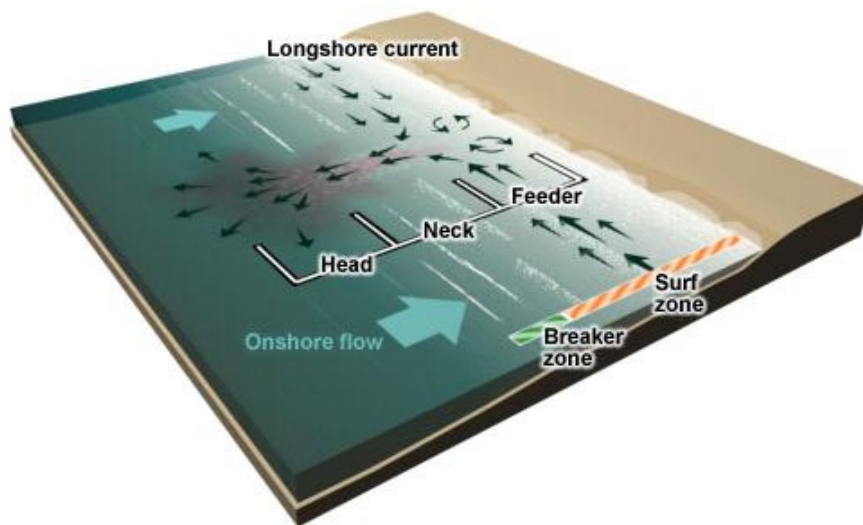


Figure 2-2 Rip current structure (*)

2.4.2 Rip current parts

2.4.2.1 Part 1: Onshore flow

In the deeper water beyond the shoaling zone, water particles of non-breaking waves have a decreasing orbital motion to a depth equal to half the wavelength, but little to no net flow in the wave direction. As waves move into shallower water, the circular orbits become progressively more distorted and upon breaking are highly disrupted. Following the wave breaking, water particles still oscillate moving landward with the wave crest and seaward with the trough. The average of these onshore currents causes a rise in the mean water level above the still water level known as wave set-up. The other parts of the nearshore circulation system stem from this onshore flow of water. For further investigation on the mass transport of waves towards the shoreline see the paper of *Longuet-Higgins* (1953).

2.4.2.2 Part 2: Longshore current

When waves break in the breaker zone and propagate further through the surf zone, they can create currents parallel to the shoreline called longshore currents. Longshore currents occur only when waves approach the shoreline at an angle. The angle of the incoming wave causes a progressively breaking wave that moves along the shoreline and a longshore current that moves

in the same direction as the breaking wave. The longshore current spans the entire width of the surf zone. It reaches maximum strength in the middle of the surf zone and diminishes in strength further offshore.

Higher waves create faster longshore currents. The angle of wave approach at breaking also affects the speed of the current. Peak currents occur when the wave approaches from 45 degrees. Higher or lower angles produce slower currents. Waves breaking parallel to the shoreline will induce no longshore current generated by the wave angle.

Like rip currents, longshore currents are subtle but can be seen or felt while standing in the surf zone. Longshore currents will always be present with rip currents as part of the rip current system.

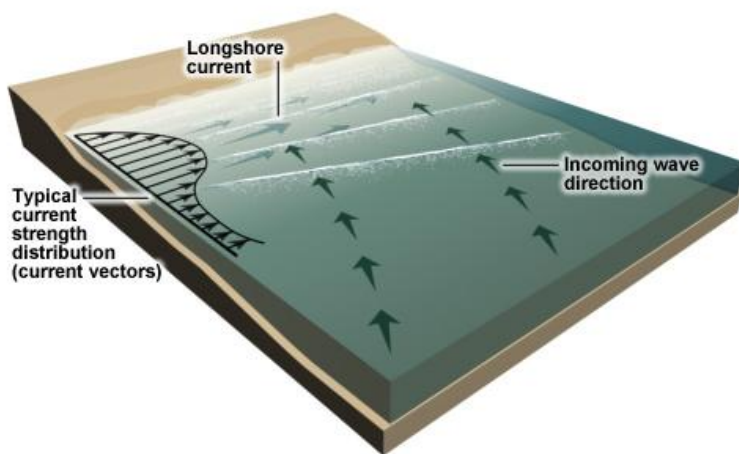


Figure 2-3: Longshore current (*)

2.4.2.3 Part 3: Rip current

Rip currents are jet-like currents of water that typically extend from near the shoreline out past the line of breaking waves.

Rip currents can be caused by several wave phenomena. These include offshore flow through channels in sandbars, variability of breaking wave heights, and longshore current interaction with structures. A portion of the longshore current enters into "feeder currents," which are the segments on the shore-side of a rip current. A rip current also has a neck and a head, as illustrated in the Figure 2-2.

2.4.2.4 Part 4: Rip head

The rip head is the part of a rip current system that is typically located beyond the breakers, marked by a spreading out or fanning of the rip current. It is here where the velocity and strength of the rip current circulation begins to weaken considerably.

2.4.3 Rip current characteristics

2.4.3.1 Wave angle

Rip currents are frequently generated when the incoming wave direction is nearly perpendicular to the shoreline. The orientation of the shoreline is therefore a key feature to note when assessing the potential for rip current formation at a particular beach. Near shore-normal waves produce a larger shoreward transport of water than obliquely incident waves (USACE, 2006). In one study, angles of incident wave direction within 20 degrees of normal to shore were correlated with increased rip current rescues (Engle, 2003). Waves incident at more oblique angles produce stronger longshore currents and are substantially less likely to form strong rip currents (Gutierrez, 2004). However, in the vicinity of shoreline structures waves approaching at angles of greater than 20 degrees create faster longshore currents and are therefore more likely to cause rip currents. Below some illustrations are given in which is shown how rip currents behave with different wave angles.

2.4.3.2 Spacing

Single-cell rip currents occur mostly in the vicinity of jetties or other man-made structures. A single rip current system can also form in a small bay with headlands. However it is more common to encounter multi-cell rip currents.

Multi-cell rip currents can form in many different conditions. Here are a few common examples of when multiple rip currents occur:

- One current is being created as another dissipates near the same location.
- Multiple gaps in the sandbar exist.
- Wave angles are close to normal on a cusped beach.

The spacing between multi-cell rip currents is generally observed to be less than 500 m and will vary based upon beach slope, shoreline orientation, wave height, and wave period.

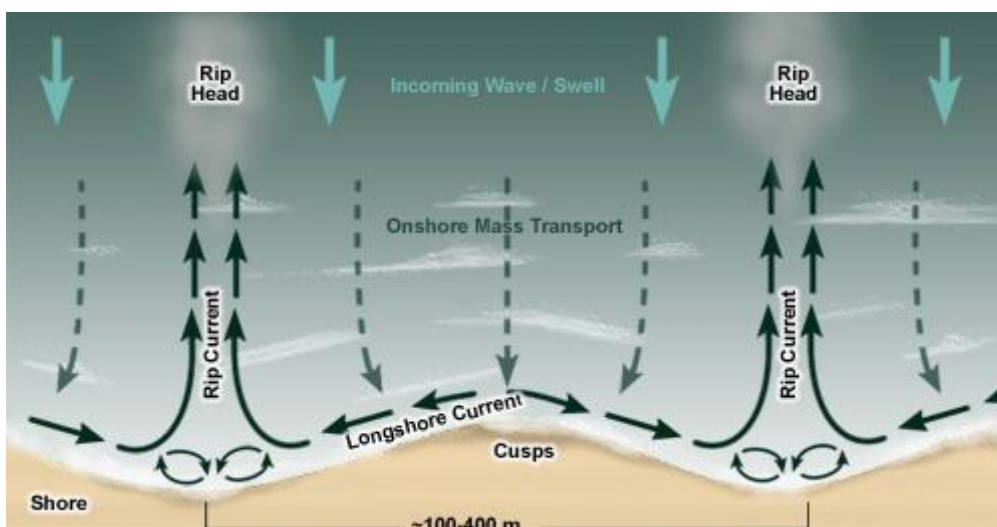


Figure 2-4: Rip current process: cusped beach (*)

2.4.3.3 Duration

Rip currents are transitory and temporal. The pulsation of an individual rip current is approximately 10 to 20 minutes. It is rare to see a rip current sustained for an hour or more. This is not to say that an area of beach will not be affected by a series of rip currents for more than 10-20 minutes as there could be multi-cell development that occurs over time along a stretch of beach.

2.4.3.4 Velocity

Rip current velocity is irregular and may swiftly increase within minutes due to larger incoming wave groups or nearshore circulation instabilities. It is imperative to understand that changes in rip current velocity occur in reaction to changes in incoming wave height and period as well as changes in water level. The rapid increase in velocity can catch unwary swimmers off guard. While rip current velocities average 0.3 – 0.6 m/s, moderate to strong rip currents can have speeds over 2 m/s.

Without the use of velocity measurements, one can attempt to estimate the potential strength of rip currents based on their spacing along a single beach. A single rip current in a given area of wave height usually indicates high offshore velocity. Multiple rip currents in the same area of given wave height tend to reduce the velocity. In general, the larger the spacing between rip currents on a single beach, the larger the potential velocity in the current. However, under the right wave and water level conditions, high velocities should be a concern on any beach, no matter what the spacing of the rip currents. In the illustrations below the rip currents with a larger spacing in between extend further offshore and thus potentially have a larger velocity.

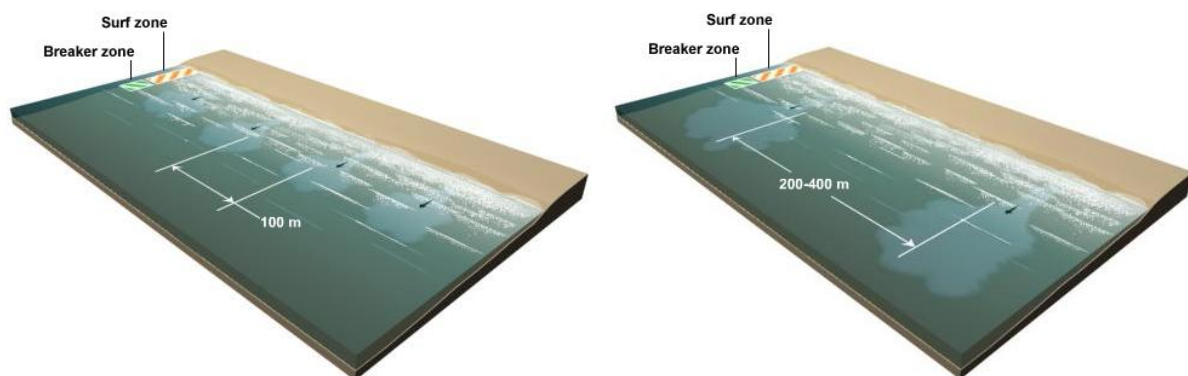


Figure 2-5: Rip current spacing vs. velocity (*)

2.4.4 Rip current forcing mechanisms

As previously mentioned, the first suggestion as to the cause of rip currents was based on mass transport by waves. In a purely two dimensional case, with the vertical and the shore normal axis, it was assumed that the pressure head provided by the shoreward mass transport of the waves caused a seaward flow. This is necessary to comply with the mass balance assumption in fluid mechanics (*Munk, 1949*). It was theoretically shown by *Longuet-Higgins (1953)* that in this case there would be an onshore flow at the surface and bottom and a seaward flow at intermediate depths. However, measurements in the ocean usually don't show this behavior and it is found that there is no offshore transport of water through breakers at intermediate depths

and no onshore flow of water in the rip currents, where the flow is directed offshore at all depths. Thus, although, a vertical circulation pattern is theoretically possible, a horizontal circulation pattern is usually dominant.

2.4.4.1 Radiation stress

Continuity of mass is one way to explain the occurrence of rip currents but by considering the continuity of momentum flux another approach can be taken to understand the phenomenon of a rip current system. Changes in mean sea level due to the incoming waves are caused by an increase or decrease of cross-shore momentum flux. *Longuet-Higgins* (1953) derived theoretical expressions for these changes in sea level. A lowering of the mean sea level was predicted as the waves approach the break point (wave set-down) and a rise in mean sea level (wave set-up) shoreward of the breakers.

Longuet-Higgins and Stewart introduced the concept of radiation stress to describe some of the nonlinear properties of surface gravity waves, the radiation stress being defined as the excess flow of momentum due to the presence of waves (*Longuet-Higgins and Stewart, 1964*)

In the theoretical study by *Bowen* (1969) the concept of *Longuet-Higgins* is used to investigate how the wave field interacts with the alongshore variations, due to different wave fields, bottom topography or due to the presence of edge waves, to produce nearshore circulation patterns. Bowen finds that the radiation stress provides the driving terms for a steady flow pattern only inside the surf zone. The radiation stress is proportional to the square of the wave height. Therefore the circulation pattern can be directly related to the alongshore variation in breaker height. Currents are flowing seaward where the breaker height is relatively low. The following figure shows an alongshore variation in wave-setup due to an alongshore variation of incoming waves.

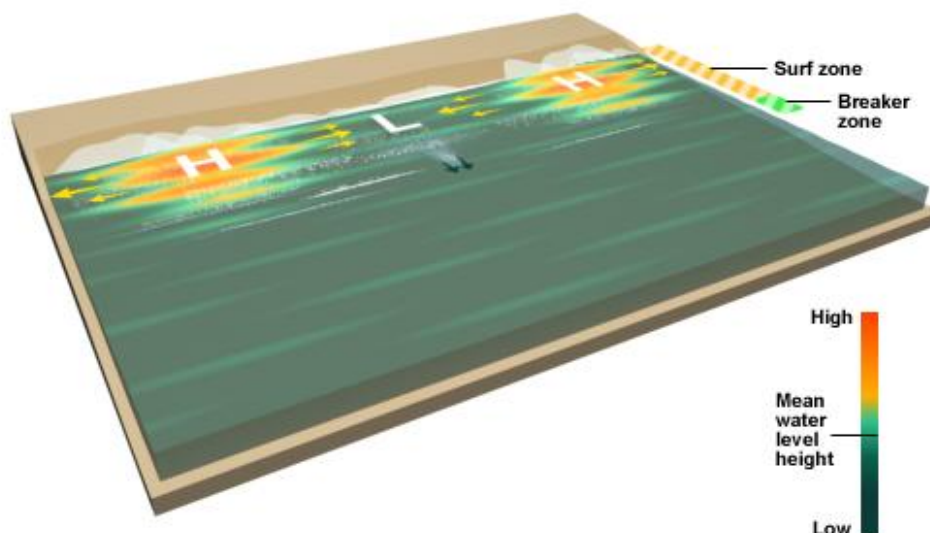


Figure 2-6: Longshore variation in wave-setup (*)

The nonlinear terms in the equation of motion show that the outward flowing current becomes narrower with increasing velocity. This specific feature of a rip current, namely the high

velocities in a narrow zone, is caused by vortex stretching over a sloping bottom topography, as was explained already by *Arthur* (1962).

2.4.4.2 Edge waves

In the experimental study by *Bowen and Inman* (1969) it was investigated if a nearshore circulation cell would occur when a plane beach was exposed to a uniform wave train, normally incident on the beach. Standing edge waves were generated on the beach of the same frequency as the incoming waves. Steady flow patterns arose from the interaction between the edge waves and the incoming waves. The circulation pattern consisted of an onshore flow toward the breakers, an alongshore current in the surf zone, and an offshore flow in relatively strong, narrow rip currents. The edge waves that are created by the normally incident incoming waves, produce an alongshore variation in waves height, and therefore producing a horizontal circulation cell. The rip currents were found to occur at alternate antinodes of the edge waves, and the spacing between the rip currents was therefore equal to the wavelength of the edge waves.

The edge wave theory, however, is only valid if the beaches are flanked by headland. Then a standing edge wave can develop between these two boundaries and a significant amount of wave energy can therefore be trapped between these headlands. Otherwise the occurrence of edge waves is difficult to explain.

2.4.4.3 Wave current interaction

In the previous mentioned studies, the wave energy and current energy have been completely uncoupled. It is known however that currents interact with encountering waves. Waves are steepened by an opposite current and their wavelength is shortened, a similar process as shoaling. This energy coupling between waves and rip currents was investigated by *LeBlond and Tang* (1974). They found that the energy interaction resists the flow, and that larger wave perturbations are needed to induce the rip currents.

Wave-current interactions not only have an effect on the wave height, wave speed and the current velocity, but they also cause the wave crest to change direction due to the difference of wave velocity along the wave crest. This effect is known as refraction and this is also of importance in the dynamics of the rip current structure. Therefore the analytical model of *LeBlond and Tang* was extended by *Dalrymple and Lozano* (1978) to include the effect of refraction of the normally incident wave field by the nearshore circulation. The analytical model describes the rip current cells on an open coastline with sloping planar foreshore and flat offshore bathymetry. The findings of the model are that refraction of the waves by the outgoing rip currents causes the waves to impinge on the beach at an angle, and therefore generating an alongshore current flowing towards the location of the rip channel. Because the rip currents reduce the wave energy, the alongshore flow is from regions of high wave energy to low wave energy, in the same manner as that of *Bowen* (1969). The analysis done by *Dalrymple and Lozano* shows that wave-current interaction can support the steady state rip current, however they have not treated the initiation mechanism that leads to this steady state.

2.4.4.4 Surf zone bathymetric features

Above studies all have shown that rip currents can occur on plane beaches with a flat bathymetry. But often rip current occurrence is caused by the interaction between waves and the bathymetry of the surf zone. Beaches can contain man-made bathymetric structures such as groins, jetties, and piers and natural bathymetric features such as canyons, ridges, and sandbars. See the figures below for the various bathymetric features that can play a role in a rip current system.

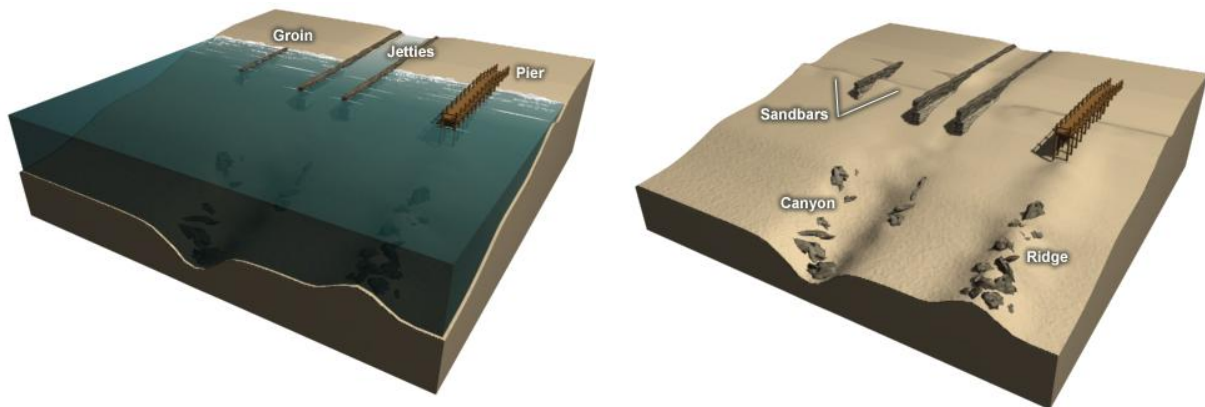


Figure 2-7: Surf zone bathymetric features (*)

Canyons and ridges

A variation of breaking wave amplitude near the shore can be caused by wave refraction by submarine canyons and ridges offshore, converging or diverging wave energy for a given wave path. This variation of breaking wave amplitude can generate a horizontal circulation cell (*Shepard and Inman, 1951*).

Sandbars

An analytical study by *Mei and Liu (1977)* has shown that a variation in depth along the shoreline causes variation in the radiation stress components and in the mean sea level in the surf zone, which creates a horizontal circulation cell of stream lines.

Often, rip currents form where a cut in a longshore sandbar is already present. Typically, the incoming waves will break on the sandbar. The sandbar acts as a dam that holds water deposited by the breaking waves. As wave set-up occurs and the longshore current develops, the low spots in the sandbar become the path of least resistance for the return flow of water. This form of a rip current system will be researched further later in this thesis. See the figure below for a typical rip current that is induced by a rip channel in a sandbar.

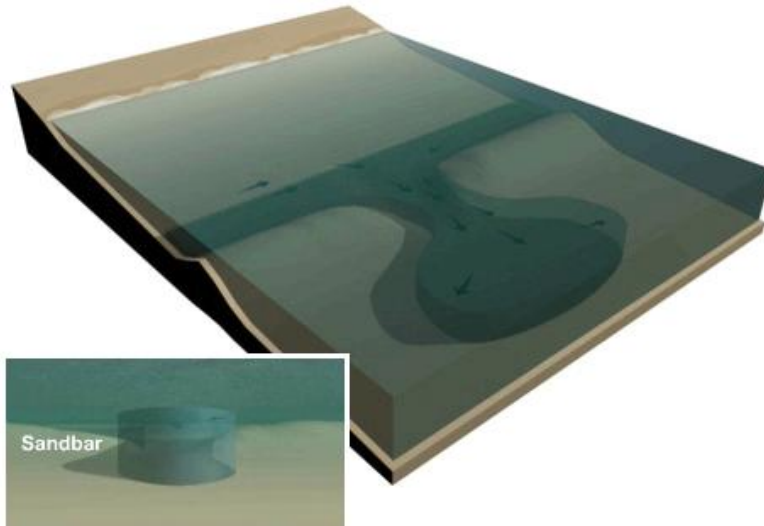


Figure 2-8: Rip current through gap in sandbar (small figure is a front view) (*)

Structures

Rip currents can also be generated by structures because a longshore current encounters a structure blocking the flow and therefore forcing its direction seaward due to water level gradients.

An experimental and computational study has been undertaken by *Wind and Vreugdenhil* (1986). They obtained data for a wave-driven current system in a closed basin to back up their computations and verify the numerical model that was used. In the basin, owing to the interaction of the longshore current with the sidewall, a strong rip current was generated. This same current system was modelled with the help of a numerical model. The effect of bottom topography, bottom friction, convection and turbulent viscosity on the current system has been investigated. In their paper they show that convective terms are of dominant importance for the dynamics of rip currents and that viscosity in the model allows for closed streamlines situated outside the breaker zone, which was in agreement with the experiment.

It can be concluded from the research of *Wind and Vreugdenhil* (1986) that for a detailed reproduction of the velocity field of the rip head adjacent to the structure, a more advanced turbulence model such as a $k-\epsilon$ model or a Smagorinsky subgrid model should be used for the computations.

2.4.5 Rip current flow

Rip current flows are induced by the incoming waves and influenced by tidal elevation and the bathymetric features that were described in the previous paragraph. In the following table hourly mean flows for various beaches have been tabulated.

| Location | U_r (m/s) | U_{max} (m/s) | λ_r (m) | w_r (m) | h_r^* (m) | h_b^* (m) | H_{mo} (m) | T_p (s) | D_{50} (mm) |
|-----------------|----------------|--------------------|--------------------|--------------|----------------|----------------|-----------------|--------------|------------------|
| Skallingen, NED | 0.3 | 1.7 | 150 | 90 | 1.25 | 1 | 0.8 | 8 | 0.25 |
| Palm Beach, AUS | 0.4 | 2 | 200 | 60 | 1.8 | 1 | 0.75 | 10 | 0.35 |

| | | | | | | | | | |
|------------------------------|------|------|-----|-----|------|-----|-----|----|------|
| Muriwai, NZL | 0.65 | 2 | 500 | 150 | 1.5 | 1 | 1.5 | 14 | 0.25 |
| Moreton Island, AUS | 0.4 | 1 | 300 | 35 | 1.4 | 1 | 0.5 | 10 | 0.2 |
| Torrey Pines, CA, USA | 0.2 | 1 | 300 | 100 | 1.25 | 1 | 0.5 | 12 | 0.1 |
| Monterey, CA, USA | 0.3 | 2 | 125 | 60 | 1.5 | 1 | 1.5 | 12 | 0.35 |
| SeaGrove, FL, USA | 0.35 | 1.25 | 60 | 30 | 0.8 | 0.3 | 0.5 | 8 | 0.3 |

Table 1: Field characteristics of rip currents

In the table above U_r is the rip current cross-shore velocity, U_{max} is the maximum documented rip current velocity, λ_r is the rip channel spacing, w_r is the rip channel width, h_r^* is the rip channel depth (* estimated to MSL), h_b^* is the bar height, H_{mo} is the significant wave height, T_p is the peak wave period, and D_{50} is the median sediment size.

The mean velocities are often quite small, however the maximum velocities can be rather large. The variation in the flow velocity can also be caused by the tidal variation of the water level over the course of a few hours (*Shepard and Inman, 1950*).

Rip currents have also been observed to pulsate on wave group temporal scales (*Shepard and Inman, 1950*). Infragravity rip current pulsations increase the rip current maximum flow to over 1 m/s over periods of 25-250 s. In addition, varying wave groups can increase the rip velocity (*MacMahan et al., 2004; MacMahan et al., 2006*).

MacMahan et. al. (2006) suggested that the rip current flow is portioned by the following frequency bands,

$$U_{rip} = U_{ig} + U_{VLF} + U_{mean} + U_{tide} \quad (2.1)$$

Where U_{ig} is the contribution within the infragravity band, 0.004 – 0.04 Hz (25 – 250 s), U_{VLF} is the contribution within 0.0005 – 0.004 Hz (4 – 30 min), U_{mean} is the mean based on the rip current system and wave conditions, and U_{tide} is the modulation associated with the slow variations in the water level. In the numerical study for this thesis the only frequency band that was present was the U_{mean} . For more information on the other contribution to the rip current velocity see the paper of *MacMahan et al. (2006)*.

As was previously stated, wave-current interaction was found (also by *Chen et. al. (1999)*) to produce a negative feedback on the wave forcing to reduce the strength and offshore extent of the flow. The weaker flow will as a result make the wave-current interaction less pronounced and thus the flow velocity will increase again. This mechanism will also cause the rip current to pulsate in strength. Furthermore, complex flow patterns occur with instabilities formed at the feeder current and with the unsteady rip flow due to vortex shedding.

The rip current flow, as was explained by *Arthur (1962)*, tends to concentrate in longshore direction as depth increases in the direction of flow. A process, which in the absence of friction, can be attributed to the conservation of potential vorticity along a stream line. As the rip current moves offshore into deeper water, the stream lines move closer together, creating a stronger and narrower current. This is due to lengthening of the vortices in this region which is known as

vortex stretching. As vorticity is described by the convective terms in the momentum equations, it can be concluded that the rip current is convection-dominated.

Vortex stretching is the lengthening of vortices in a three-dimensional fluid flow, associated with a corresponding increase of the component of vorticity in the stretching direction, due to the conservation of momentum.

Vortex stretching is at the core of the description of the turbulence energy cascade from the large scales to the small scales in turbulence. In general, in turbulent fluid elements are more lengthened than squeezed, on average. This results in more vortex stretching than vortex squeezing. For incompressible flow the lengthening implies thinning of the fluid elements in the directions perpendicular to the stretching direction. This reduces the radial length scale of the associated vorticity. Finally, at the small scales of the order of the Kolmogorov microscales, the turbulence kinetic energy is dissipated into heat through the action of molecular viscosity.

3 Numerical modelling of nearshore hydrodynamics

3.1 Introduction

An analytical solution to the governing equations in a rip current system that has as a result a horizontal circulation cell is only found for a two dimensional and very simplified system of equations (*Bowen, 1969; Mei and Liu, 1977*). However, most of the assumptions made in the analytical models are not entirely justified. To find solutions for more complex geometry and without all of the simplifications, use is made of numerical models that approach the solution to the governing equations to certain accuracy. There are many different numerical models that are capable of modelling rip currents. The appropriate model depends mainly on the complexity of the situation, on the type of beach and on the balance between accuracy and efficiency.

3.2 Nearshore modelling

The first mature models that calculated the wave-driven nearshore circulation and that incorporated important factors like convection and viscosity in the flow equations were reported by e.g., *Ebersole and Dalrymple (1979)*, *Wind and Vreugdenhil (1986)* and *Wu and Liu (1982)*. In these models the wave field was still limited to unidirectional linear monochromatic waves. A review of the state-of-the-art surf zone models of those days can be found in *Basco (1983)*.

In the following years more sophisticated models, that still had a decoupled wave and flow model, were introduced that included diffraction and breaking criteria for random waves. Current refraction was also incorporated through successive and iterative executions of the flow and wave models. A review was given by *Battjes et. al. (1990)* wherein they focused on the wave-induced nearshore circulations. One of their conclusions stated that the numerical models, with their improvements and more mature state of the decoupled concept of wave-flow modelling, were still only able to determine the steady circulation, while no models could yet handle low-frequency motions in the surf zone.

3.3 Boussinesq models

Nowadays the most popular models for nearshore modelling incorporate the Boussinesq theory in which the vertical structure of the velocity is not an exact solution of the basic nonlinear balance equations. Instead it is imposed that the horizontal velocity is constant over the vertical and the vertical velocity is varying nearly linear from the bottom to the surface.

The original equations from Joseph Boussinesq have been modified by many investigators to extend the applicability and improve various desired characteristics of the corresponding wave. One of the most successful extensions to the Boussinesq equations were done by *Madsen and Sørensen (1992)*. They extended the applicability of the Boussinesq equations to deeper water and they also included the possibility of wave breaking by a separate body of fluid on the wave surface with a dissipative effect on the energy balance, simulating the real life wave rollers. These extended Boussinesq equations with the improved dispersion properties and the possibility of wave breaking, were the basis of a model developed by *Madsen et. al. (1997a)*. This

model has been used to study the wave-driven nearshore circulation. The model uses a coupled approach, thus the surface gravity waves and the flow are computed with the same model, which eliminates the necessity to iteratively find the interaction effects between the waves and the currents. The model has been applied to two examples of wave-induced nearshore circulation, both with waves normally incident on a plane sloping beach. The first example has a rip channel in the bottom profile of the beach, and the second is concerned with a detached breakwater parallel to the shoreline. Both simulations show good agreement with laboratory measurements both with respect to the variation of the wave heights and setup and the resulting wave-generated current patterns. Furthermore, this model has the potential to simulate more complicated phenomena like low frequency motions (*Chen et al., 1999; Madsen et al., 1997a; Madsen et al., 1997b; Sørensen et al., 1998*).

3.4 Non-hydrostatic models

From previous paragraph it can be concluded that Boussinesq-type models are a useful tool to study nearshore circulation. However, there are alternatives to using Boussinesq equations for the simulation of a two-dimensional rip current structure. Moreover, one can be interested in the three-dimensional structure of a rip current, which therefore eliminates the choice of a Boussinesq-type model because of its depth averaged nature. One promising approach is, instead of using the Boussinesq equations, to discretize the water in one or more layers and to use the Navier-Stokes equations. This gives a model with similar wave characteristics to those of the extended Boussinesq-type models (*Stelling and Zijlema, 2003; Zijlema and Stelling, 2005*). There are a many more models that make use of the Navier-Stokes equations or the Euler equations to compute the flow and the wave field, however, other than the proposed method by *Stelling and Zijlema*, these methods need 10 to 20 vertical layers in order to obtain accurate results, resulting in a longer computation time. These models are therefore less competitive than the Boussinesq-type models. The method of *Stelling and Zijlema* utilizes an edge based compact difference scheme for the approximation of the vertical gradient of the non-hydrostatic pressure. This ensures accurate wave breaking and dispersion characteristics of the modelled waves.

In the XBeach model a depth averaged approach of *Stelling and Zijlema* is taken. Even though the depth averaged approach less accurately computes the dispersion of waves, the result obtained by *Smit (2008)* of the Berkoff test case showed that for relatively short waves the diffraction, refraction and wave shoaling was modelled very satisfactorily using only one layer. The two layer approach only improved the result marginally. The depth averaged method, however, is more competitive with the Boussinesq-type models regarding efficiency and comparable regarding accuracy. The big advantage of the XBeach model is the robustness. Almost no calibration is required, unlike Boussinesq-type models.

4 Model description

4.1 Introduction

In the previous chapter one was given an overview of some of the different types of models being used in the field of computational fluid dynamics for coastal engineering problems. As was stated the numerical method that is being used for the topic of research in this thesis, is the method developed by *Stelling and Zijlema* (2003; 2005). This scheme is incorporated into the depth averaged XBeach program, which uses the same non-hydrostatic pressure correction technique for the Non Linear Shallow Water Equations (NSWE). However, it is different to the numerical scheme proposed by *Stelling and Zijlema* with respect to the time discretisation, which in the XBeach model is made second order accurate as opposed to first order accurate. The subject of this chapter is a brief description of the numerical model in its two dimensional depth integrated (2DH) form. See Appendix B for the derivation of the governing equations and Appendix C for a detailed description of the discretisation technique used in this numerical model.

4.2 Governing equations

The governing equations of the numerical model are based on the three-dimensional unsteady incompressible Reynolds-averaged Navier-Stokes equations. To model the non-hydrostatic free-surface flows with gravity waves these equations have to be solved together with the continuity equation. The numerical model XBeach is a depth averaged model and therefore the governing equations have to be integrated over the water depth. These equations are written as follows in non-conservative form. See Appendix B for the derivation of these equations.

$$\begin{aligned}
 \frac{\partial U}{\partial t} + U \frac{\partial U}{\partial x} + V \frac{\partial U}{\partial y} + g \frac{\partial \zeta}{\partial x} + \frac{1}{H} \int_{-d}^{\zeta} \frac{\partial p}{\partial x} dz &= \frac{1}{\rho H} \frac{\partial H \bar{\tau}_{xx}}{\partial x} + \frac{1}{\rho H} \frac{\partial H \bar{\tau}_{xy}}{\partial y} - \frac{\tau_{bx}}{\rho H} \\
 \frac{\partial V}{\partial t} + V \frac{\partial V}{\partial x} + U \frac{\partial V}{\partial y} + g \frac{\partial \zeta}{\partial y} + \frac{1}{H} \int_{-d}^{\zeta} \frac{\partial p}{\partial y} dz &= \frac{1}{\rho H} \frac{\partial H \bar{\tau}_{yx}}{\partial x} + \frac{1}{\rho H} \frac{\partial H \bar{\tau}_{yy}}{\partial y} - \frac{\tau_{by}}{\rho H} \\
 \frac{\partial W}{\partial t} + U \frac{\partial W}{\partial x} + V \frac{\partial W}{\partial y} + \frac{1}{H} (p|_{\zeta} - p|_{-d}) &= \frac{1}{\rho H} \frac{\partial H \bar{\tau}_{xz}}{\partial x} + \frac{1}{\rho H} \frac{\partial H \bar{\tau}_{yz}}{\partial y}
 \end{aligned} \tag{4.1}$$

The vertical integration of the non-hydrostatic pressure gradient in equation (4.1) is written as follows by virtue of the Leibniz' rule of integration:

$$\int_{-d}^{\zeta} \frac{\partial p}{\partial x} dz = \frac{\partial}{\partial x} \int_{-d}^{\zeta} p dz - p|_{z=-d} \frac{\partial d}{\partial x} \tag{4.2}$$

The integral as occurred in the right hand side of (4.2) is approximated by

$$\int_{-d}^{\zeta} p dz \approx \frac{1}{2} H (p|_{z=\zeta} + p|_{z=-d}) = \frac{1}{2} H p|_{z=-d} \tag{4.3}$$

Finally, writing (4.2) in non-conservative form, we obtain

$$\int_{-d}^{\zeta} \frac{\partial p}{\partial X} dz = \frac{1}{2} H \frac{\partial p|_{z=-d}}{\partial X} + \frac{1}{2} p|_{z=-d} \frac{\partial(\zeta-d)}{\partial X} \quad (4.4)$$

The process is very similar for the gradient of the dynamic pressure in the y -direction.

The depth integrated approach of the model is, regarding to the modelled accuracy of the frequency dispersion, comparable to the Boussinesq model of *Peregrine* (1967). Higher accuracy of the frequency dispersion of the modelled waves can be obtained by adding more layers in the vertical.

In the momentum equations (4.1) the stress terms $\bar{\tau}_{ij}$ include the effect of subgrid turbulent mixing. These terms are defined as follows

$$\begin{aligned} \bar{\tau}_{xx} &= 2\nu_t \frac{\partial U}{\partial X}, \quad \bar{\tau}_{yy} = 2\nu_t \frac{\partial V}{\partial Y} \\ \bar{\tau}_{xy} &= \bar{\tau}_{yx} = \nu_t \left(\frac{\partial V}{\partial X} + \frac{\partial U}{\partial Y} \right) \\ \bar{\tau}_{xz} &= \nu_t \frac{\partial W}{\partial X}, \quad \bar{\tau}_{yz} = \nu_t \frac{\partial W}{\partial Y} \end{aligned} \quad (4.5)$$

The eddy viscosity ν_t can be a constant or can be determined with a Smagorinsky eddy viscosity model.

4.3 Grid schematization

The numerical model uses a rectangular structured grid, in which a cell with its centre at $\mathbf{x}_{i,j} = (x_i, y_j)$ is bounded by the horizontal grid lines $x = x_{i \pm \frac{1}{2}, j}$ and $y = y_{i, j \pm \frac{1}{2}}$ and between the bottom $z = -d = -d(\mathbf{x}_{i,j})$ and free surface $z = \zeta_{i,j} = \zeta(\mathbf{x}_{i,j})$. The local mesh sizes $\Delta x_{i,j}$, $\Delta y_{i,j}$ and the local water depth $H_{i,j}$ are then described by

$$\Delta x_{i,j} = x_{i+\frac{1}{2},j} - x_{i-\frac{1}{2},j}, \quad \Delta y_{i,j} = y_{i,j+\frac{1}{2}} - y_{i,j-\frac{1}{2}}, \quad H_{i,j} = \zeta_{i,j} + d_{i,j} \quad (4.6)$$

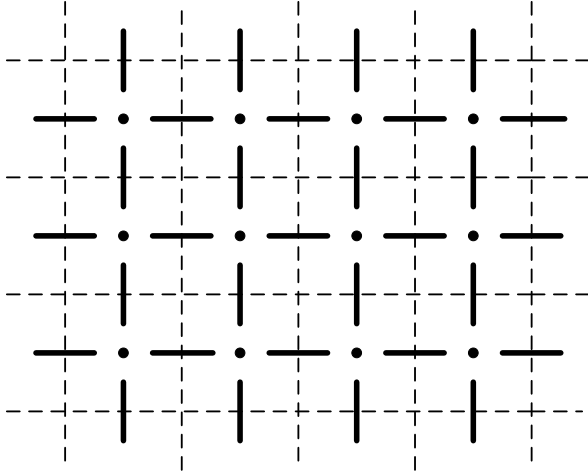


Figure 4-1: Horizontal location of variables (#)

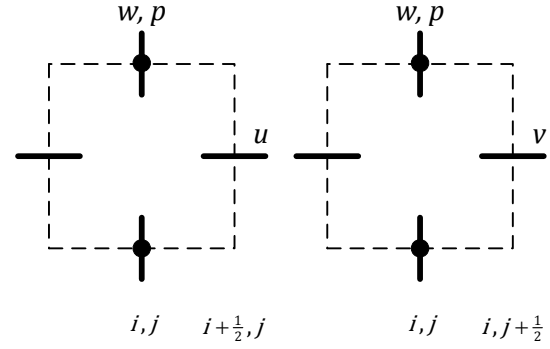


Figure 4-2: Vertical location of variables (#)

For the horizontal variable layout a staggered arrangement is employed. In the staggered arrangement the pressure, bottom and free surface variables are all located at the cell centre. The averaged horizontal velocity components U and V , on the other hand, are respectively located at the cell faces $\mathbf{x}_{i+1/2,j}$ and $\mathbf{x}_{i,j+1/2}$.

Although the model is in a depth integrated form (2DH), a vertical momentum equation has to be solved due to a cell face approach of the pressure. However, unlike for the horizontal momentum equations, the vertical variable arrangement is not staggered to allow for the application of a compact scheme. Both the pressure terms and the vertical velocity components are located at the cell face (See Figure 4-2). This allows for a very natural inclusion of the boundary condition of the dynamic pressure at the free surface, which is assumed to be zero at the free surface. And it appears that a correct approximation of the pressure distribution in the top cell is key to modelling dispersive waves correctly (*Stelling and Zijlema, 2003*).

The equations in (4.6) allow for non-uniform mesh sizes. This makes it possible to locally reduce the mesh size and thus increase computational accuracy where a strong variation in the flow is expected.

In the governing equations (4.1) the momentum balance is non-conservative, however for an accurate prediction of the breaking of waves the advective terms have to be discretized in a conservative approach. This ensures a conservation of the momentum within the grid cell. The

advective term $U \frac{\partial U}{\partial x}$ is discretized as follows:

$$U \frac{\partial U}{\partial x} = \frac{{}^x \bar{q}_{i+1,j} U_{i+1,j} - {}^x \bar{q}_{i,j} U_{i,j}}{\bar{H}_{i+1/2,j} \Delta x} + \frac{U_{i+1/2,j+1/2} {}^x \bar{q}_{i+1,j} - {}^x \bar{q}_{i,j}}{\bar{H}_{i+1/2,j} \Delta x} \quad (4.7)$$

With ${}^x \bar{q}_{i+1,j} = {}^x q_{i+1/2,j}^n - {}^x q_{i-1/2,j}^n$ and ${}^x q_{i+1/2,j}^n = U_{i+1/2,j}^{n+1/2} H_{i+1/2,j}^n$, ${}^y q_{i,j+1/2}^n = V_{i,j+1/2}^{n+1/2} H_{i,j+1/2}^n$. The water depth is not defined at the velocity points and thus needs to be interpolated from surrounding points. We use a simple first order accurate upwind interpolation:

$$H_{i+\frac{1}{2},j}^n = \begin{cases} \zeta_{i,j}^n + \max(d_i, d_{i+1}) & \text{if } U_{i+\frac{1}{2},j}^{n+\frac{1}{2}} > 0 \\ \zeta_{i+1,j}^n + \max(d_i, d_{i+1}) & \text{if } U_{i+\frac{1}{2},j}^{n+\frac{1}{2}} < 0 \\ \max(\zeta_{i,j}^n, \zeta_{i+1,j}^n) + d_{i+\frac{1}{2}} & \text{if } U_{i+\frac{1}{2},j}^{n+\frac{1}{2}} = 0 \end{cases} \quad (4.8)$$

Based on the expression for $H_{i+\frac{1}{2},j}^n$, as given by (4.8), it can be shown that if the time step is chosen such that $\Delta t |U_{i+\frac{1}{2},j}^{n+\frac{1}{2}}| / \Delta x < 1$ at every time step then the water depth $H_{i,j}^{n+1}$ is non-negative at every time step (*Stelling and Duinmeijer, 2003*). Therefore flooding never happens faster than one grid size per time step. This is physically correct and therefore the calculation of the dry areas does not need any special feature. For computational efficiency, the momentum equations are not solved and velocity values are set to zero if the water depth $H_{i+\frac{1}{2},j}^n$ is below a threshold value. The value in this thesis is set to 10^{-5} m. This approach has been verified by *Zijlema and Stelling (2008)* and they found the approach to be very effective without much numerical difficulty.

4.4 Boundary conditions

In order for the equations to have a unique solution, boundary conditions need to be prescribed. These boundary conditions are prescribed for the tangential and normal velocities along the entire boundary of the domain. This includes the bottom, the water surface and the four vertical boundaries. See the figure below for the computational domain with its boundaries.

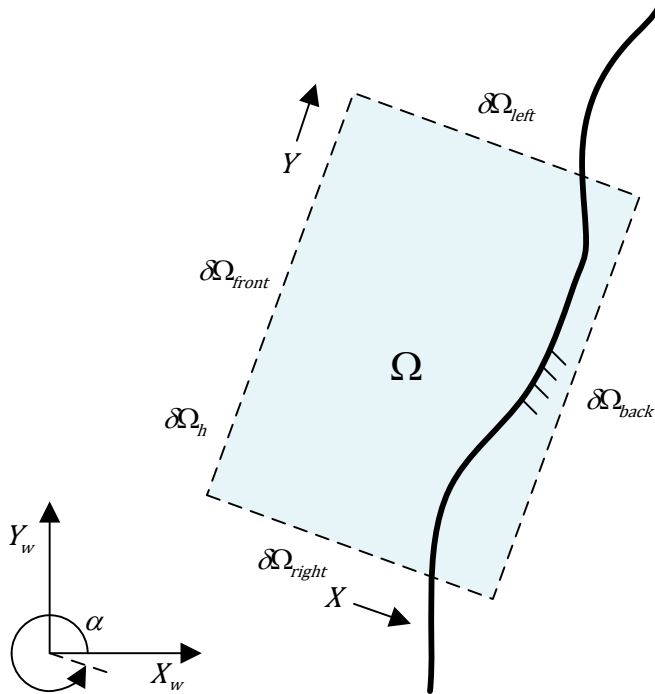


Figure 4-3: Horizontal domain Ω in relation to the global domain (#)

In Figure 4-3 the computational domain Ω is bounded horizontally by a rectangular shaped boundary $\partial\Omega_h$ which consists of four vertical planes. The front boundary $\delta\Omega_{\text{front}}$ is the seaward

boundary and the back boundary $\delta\Omega_{\text{back}}$ is the landward boundary, both of which are parallel to the y-axis. The boundaries parallel to the x-axis are the two side boundaries $\delta\Omega_{\text{left}}$ and $\delta\Omega_{\text{right}}$. Vertically the domain is bounded by the single valued free surface $z = \zeta(\mathbf{x}, t)$ and the bottom $z = -d(\mathbf{x}, t)$.

4.4.1 Free surface and bottom

At the free surface the tangential and normal stresses are assumed to be continuous and the total pressure is set to zero, therefore neglecting surface tension effects and differences in the atmospheric pressure. This leads to the boundary condition for the dynamic pressure:

$$p(\mathbf{x}, \zeta(\mathbf{x}, t), t) = 0 \quad (4.9)$$

Tangential stresses at the surface due to wind can be described using suitable expressions for the large scale influence of the wind. It is, however, not possible to include generation of waves with these expressions.

At the bottom the kinematic boundary condition (B.9) is used. The two tangential stresses due to bottom friction are specified using an expression based on the depth averaged velocity:

$$\tau_{bx} = c_f \rho U |U|, \quad \tau_{by} = c_f \rho V |V| \quad (4.10)$$

Wherein c_f is a dimensionless coefficient.

4.4.2 Closed boundaries

At closed boundaries the boundary can be regarded as a solid vertical wall. No discharge can go through the boundary, which means that the normal velocity is set to zero. For the tangential velocities the free-slip condition is applied which implies a zero gradient of the tangential velocity.

4.4.3 Open boundary

At the seaward boundary and landward open boundary the normal velocity has to be prescribed. The gradient of the tangential velocities at these boundaries are assumed to be zero. For a non-reflecting boundary an absorbing-generating boundary condition based on the Riemann invariants is used.

To construct this boundary condition a few simplifications are made. Firstly, the boundary is considered to be a straight line. The x-axis is perpendicular to the boundary and is directed positive inwards and the y-axis is parallel to the boundary. Secondly, the bottom located at the boundary is approximated as flat and non-linearity's are neglected. At the boundary the surface elevation and depth averaged velocity are the summation of the incoming and reflected signal.

$$\zeta = \zeta^r + \zeta^{in}, \quad U = U^r + U^{in} \quad (4.11)$$

The incoming wave signal at the boundary is composed of N long crested harmonic free linear waves. Each wave travels with its own celerity c_k along a straight ray in the direction θ_k . Along each wave ray a local coordinate system s, t is prescribed with s parallel to the wave ray and t

perpendicular to the wave ray. The time varying depth averaged velocity due to harmonic k in the direction of s is denoted by \hat{u}_k . At the boundary the total depth averaged velocity and surface elevation due to the incoming waves is given by

$$\mathbf{u}^{in} = \sum_{k=1}^N \mathbf{u}_k^{in}, \quad \zeta^{in} = \sum_{k=1}^N \zeta_k^{in} \quad \text{with } \mathbf{u}_k = (u_k, v_k), \quad u_k = \hat{u}_k \cos \theta_k \quad \text{and} \quad v_k = \hat{u}_k \sin \theta_k \quad (4.12)$$

With the assumption that the wave forms remain constant along the individual wave rays, each of the harmonics obeys

$$\frac{\partial \hat{u}_k^{in}}{\partial t} - c_k \frac{\partial \hat{u}_k^{in}}{\partial s} = 0 \quad (4.13)$$

For linear waves this condition can also be written as

$$\begin{aligned} u_k^{in} - c_k \cos \theta_k \frac{\zeta_k^{in}}{H} &= 0 \\ v_k^{in} - c_k \sin \theta_k \frac{\zeta_k^{in}}{H} &= 0 \end{aligned} \quad (4.14)$$

The applications that are considered only requires the velocity component perpendicular to the boundary and therefore the v -components are ignored from now on.

The reflected signal also consists of different wave components each travelling in its own direction and velocity. However it is very hard to obtain from the model in what direction and in with which velocity these reflected signals are travelling. Therefore it is assumed that the reflected signal only contains relatively long waves traveling perpendicular to the boundary. This is a reasonable assumption as most short wave energy is dissipated due wave breaking and only the infragravity waves are reflected. With these two assumptions the Sommerfeld radiation condition for the reflected waves is written as

$$\frac{\partial u^r}{\partial t} - c \frac{\partial u^r}{\partial x} = 0 \quad (4.15)$$

In which c is the shallow water wave celerity. Again assuming linear waves equation (4.15) can be rewritten as

$$U^r + \frac{c}{H} \zeta^r = 0 \quad (4.16)$$

Now we can add the two relations (4.14) and (4.16) to obtain an expression for the velocity at the boundary resulting in

$$\sum_{k=1}^N U_k^{in} + U^r - \sum_{k=1}^N c_k \frac{\zeta_k^{in}}{H} + \frac{c}{H} \left(\zeta^r - \sum_{k=1}^N \zeta_k^{in} \right) = 0 \quad (4.17)$$

Finally substituting (4.11) into (4.17) this is written as

$$U_b = U^{in} + \sqrt{\frac{g}{H}} (\zeta^r - \zeta^{in}) \quad (4.18)$$

This is the weakly reflective boundary condition that replaced the boundary condition already present in the model which was based on *Van Dongeren and Svendsen (1997)*, which is also a weakly reflective boundary and is used for 2D cases. The boundary condition described here assumes reflected waves that are perpendicular to the boundary. In 2D cases this can lead to significant errors if the reflected waves do not propagate close to normal to the boundary. Note that the boundary condition, as described here, also requires the incoming surface elevation to be provided at the boundary in addition to the velocity.

The boundary condition from *Van Dongeren and Svendsen* is based on the method of characteristics and assumes that both outgoing and incoming waves travel with the long wave celerity, $c = \sqrt{gh}$.

4.5 Wave breaking

In numerical models, wave breaking is a difficult phenomenon to capture accurately, as the free surface, which acts as an air-water interface, assumes complex shapes due to e.g. wave overturning. Furthermore, the air-water interface in breaking waves is often hard to define due to the mixing of water and air. As was previously mentioned, there are computational methods that can handle these types of problems (Volume of fluid methods, Marker and Cell), but these are numerically very intensive and therefore too expensive for the large scale coastal engineering applications. Also the detailed information of what happens in a breaking wave is not necessary for coastal engineering practice.

In the present model the free surface is tracked with a single valued function of the horizontal plane. This approach is more efficient and makes the simulation of the wave transformation in the coastal zone feasible. However, this does mean that breaking waves can no longer be captured in detail. Instead, wave breaking is regarded as a sub-grid process. Thus the waves can steepen until the front face is almost vertical, but then the process of overturning is not modelled.

This approach has also been successfully applied in other non-hydrostatic numerical models based on the non linear shallow water equations (NSW-equations) (e.g. *Hibberd and Peregrine, 1979*). In these models the analogy between a bore and a breaking wave is used to simulate wave evolution during breaking and run-up. This is justified because from the study of *Peregrine and Svendsen (1978)* it appears that the breaking process itself stabilizes the wave form into a turbulent almost vertical front. This means that during breaking a long wave develops for which mass and momentum are conserved. The energy dissipation in such a wave is of the same rate as in a bore of similar height (*Svendsen, 2006*).

Just before the breaking point of the wave, when the wave is still steepening, both frequency dispersion and non-linear effects are important. The non-linear properties tend to steepen the wave while on the other hand the frequency dispersion is doing the opposite. Because in the NSW-equations the frequency dispersion is not included the balancing effect of frequency

dispersion is missing, which causes the wave to break prematurely. Therefore models based on the NSW-equations are not suitable for the determination of the breaking point accurately, which make them only valid after breaking has been initiated.

Non-hydrostatic models, however, do not have this predicament as they include frequency dispersion and are therefore applicable in the region prior breaking. Furthermore, because they reduce to the NSW-equations in shallow water they can also be used after breaking has been initiated.

In the paper of *Zijlema and Stelling (2008)* it was shown by the authors that their non-hydrostatic model with this approach was capable of predicting the breakpoint accurately. The most attractive feature of this approach is that there are no external parameters (such as maximum steepness), which tell the model when breaking should be initiated.

The XBeach model described in this thesis, is an adapted version of the non-hydrostatic model presented in *Zijlema and Stelling (2008)*. Momentum and mass conservation are guaranteed using a conservative numerical method based on *Stelling and Duinmeijer (2003)*. Therefore the model behavior for wave breaking is similar to their model. The largest difference is the depth averaged method applied in the XBeach model instead of the two layer approach in the model of *Zijlema and Stelling (2008)*. Due to the depth averaged method the frequency dispersion is modelled less accurately and this can lead to overestimation of wave energies in the high frequency range. The breaking point is still accurately simulated but the rate of energy dissipation after breaking is underestimated, which could lead to an overestimation of the wave height in the surf zone. Also the vertical structure of the flow is not resolved and therefore dissipation due to a vertical gradient of the flow velocity is not accounted for. An eddy viscosity model, like e.g. the Smagorinsky subgrid model, can increase the rate of energy dissipation after breaking due to the high velocity gradients found in the surf zone.

4.6 Smagorinsky eddy viscosity model

The Smagorinsky eddy viscosity model (*Smagorinsky, 1963*) is usually used in Large Eddy Simulations (LES), in which the Navier-Stokes equations are averaged over space, which gives a result similar to the Reynolds equations, in which the Navier-Stokes equations are ensemble averaged over time. The large eddy simulation resolves, as the name suggests, the large eddies, due to the averaging over the grid size. The smaller eddies that occur within one or more grid volumes are not resolved, however these eddies are small and are more isotropic than the larger eddies. The larger structures are broken up into the smaller scales via the energy cascade and they lose their self-similar processes that are not much affected by the large scale geometry. This means that the small scales are less of a problem to model. Moreover, the most important function of the small scale turbulence is the energy dissipation of the large scale motion.

The small scale turbulences are modelled using sub-grid stress, see equation(4.5). In these terms the eddy viscosity is defined by the mesh size and the sub-grid deformation. This eddy viscosity is calculated from the gradients of the flow velocity at the resolved scale as follows:

$$v_t = (C_s \Delta_s)^2 \sqrt{2 \sum_{i=1}^2 \sum_{j=1}^2 (S_{ij} S_{ij})}, \quad S_{ij} = \frac{1}{2} \left(\frac{\partial \mathbf{u}_i}{\partial \mathbf{x}_j} + \frac{\partial \mathbf{u}_j}{\partial \mathbf{x}_i} \right) \quad (4.19)$$

The only coefficient needed in the Smagorinsky model is the Smagorinsky constant denoted by C_s [-] and is usually given a value between 0.1 and 0.2. In our simulations a value of 0.2 seemed to give the best results. The length scale used in the Smagorinsky formulation Δ_s is the scale of the smallest resolvable eddy and in our case is defined as $\Delta_s = \sqrt{\Delta x \Delta y}$. This scale is essentially the filter width employed and is therefore dependent on the mesh size. In the Boussinesq model of Chen et. al. (1999) for the modelling of a rip current system the same length scale was used.

As previously mentioned this approach for the eddy viscosity has the advantage that it adds dissipation in regions where high gradients of the flow occur. In smooth regions of flow it adds very little dissipation which is important for the propagation of waves outside the surf zone because the influence of turbulent viscosity is negligible here.

4.6.1 Discretisation of the Smagorinsky model

The discretisation of the Smagorinsky subgrid model for the eddy viscosity is as follows, with the eddy viscosity defined in the cell center:

$$v_{i,j} = (C_s \Delta_s)^2 \sqrt{2 \left[\left(\frac{\partial U}{\partial x} \right)^2 + \left(\frac{\partial V}{\partial y} \right)^2 + \frac{1}{2} \left(\frac{\partial U}{\partial y} + \frac{\partial V}{\partial x} \right)^2 \right]} \quad (4.20)$$

in which

$$\frac{\partial U}{\partial x} = \frac{U_{i,j} - U_{i-1,j}}{\Delta x}, \quad \frac{\partial V}{\partial y} = \frac{V_{i,j} - V_{i,j-1}}{\Delta y}$$

$$\frac{\partial U}{\partial y} = \frac{1}{2} \frac{U_{i,j+1} - U_{i,j-1} + U_{i-1,j+1} - U_{i-1,j-1}}{\Delta y}, \quad \frac{\partial V}{\partial x} = \frac{1}{2} \frac{V_{i+1,j} - V_{i-1,j} + V_{i+1,j-1} - V_{i-1,j-1}}{\Delta x}$$

5 Validation and verification

In order to assess if the numerical model XBeach can accurately simulate the physical processes involved in the nearshore zone, the approach as described in Chapter 4 is compared to two cases which have measured data from a laboratory. The following cases will be considered:

1. Irregular wave breaking in a laboratory barred surf zone
2. Experiments on rip currents and nearshore Circulation

The first case to be considered is a laboratory experiment, in which the surf zone turbulence was accurately measured. This case is used to verify the correct wave setup and breaking point. Also this case is very useful to see if the significant wave height is correctly modelled throughout the field. The second case considered is a comprehensive laboratory experiment in a directional wave basin with a longshore bar, in which two rip channels were present. The measurement data included the free surface and the velocity at various locations in the wave basin.

5.1 Irregular wave breaking in a laboratory barred surf zone

5.1.1 Introduction

The laboratory flume test of *Boers* (2005) is a study with a field-like surf zone with breaker bars and irregular waves in a wave flume. This experiment allows for an excellent comparison to the model to verify the important characteristics of waves in the surf zone. The beach profile is a barred beach as shown in the figure below.

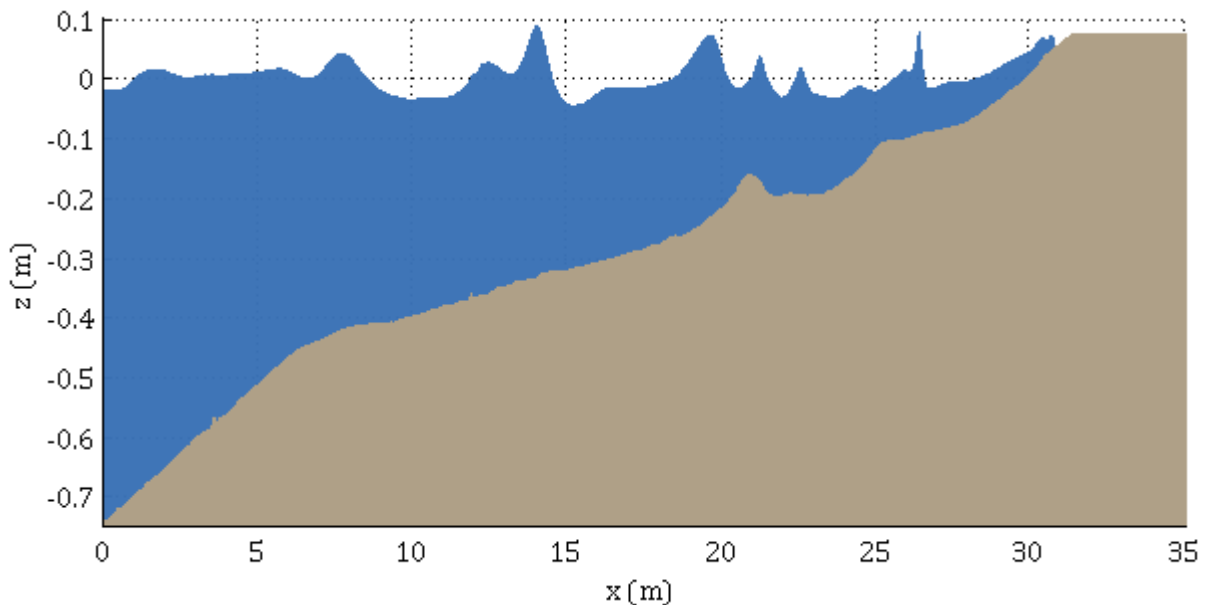


Figure 5-1: Snapshot of the computation

The experiment that *Boers* carried out involved taking numerous measurements. In fact he measured the surface elevation at 70 locations with wave gauges throughout the wave flume. The physical parameters in the surf zone such as wave heights and periods are based on the

surface elevation. Also use was made of Laser-Doppler Velocimeters (LDV), an electromagnetic flow meter, a shear stress plate and a video camera.

In the experiments *Boers* conducted, three irregular wave conditions were considered with different significant wave heights and periods. See Table 2 for the three different wave conditions.

| Wave test | measured H_{m0} [m] at $x = 0$ m | measured T_p [s] at $x = 0$ m | duration [s] of wave series |
|----------------|---------------------------------------|------------------------------------|--------------------------------|
| Test 1A | 0.157 | 2.05 | 157.079 |
| Test 1B | 0.206 | 2.03 | 157.079 |
| Test 1C | 0.103 | 3.33 | 245.441 |

Table 2: Measured wave conditions

It can be seen in the table that Test 1C has the lowest wave steepness. This case is the most interesting for us to compare our model with as these lesser steep waves break in the shallow region only. For the other conditions it appears the waves break throughout the flume as well as the waves at the boundary are already highly non-linear, which makes it much harder to impose the right boundary velocity.

Also from *Stelling and Zijlema (2003)* and *Smit (2008)* we know that the dispersion is more inaccurately modelled with the depth averaged method than with the a non-hydrostatic model with 2 layers, especially when kH values, which is the wave number k multiplied with the water depth H , exceed about 2.0 [-]. However in the *Boers* test case kH is around 0.9 [-] at the boundary, and the depth and wave period only decreases onward from there. In the surf zone the kH value is even smaller, just before the first breaker bar the value is estimated to be around 0.6 [-]. These kH values are small enough to compute with only one layer for sufficient accurate results regarding the wave celerity which affects the significant wave height and mean zero-crossing period.

5.1.2 Boundary condition

5.1.2.1 Fourier transform of the surface elevation

The boundary condition imposed in the numerical model is a cross-shore velocity derived from the measured surface elevation at the boundary. This is done with a Discrete Fourier Transform (DFT) and the linear dispersion relation, assuming that the surface elevation was made up of free harmonics. The surface elevation in the flume at the boundary was measured with a wave gauge and was sampled with a frequency of 20 Hz. The measured wave series was then transformed in all the components that made up the total wave signal at the boundary. This was done with the use of a Fast Fourier Transform (FFT) algorithm. An FFT computes the DFT and produces exactly the same result as evaluating the DFT definition directly. The only difference is that an FFT is much faster. The DFT is defined by the following equation.

$$X_k = \sum_{n=0}^{N-1} x_n e^{-i2\pi k \frac{n}{N}} \quad k=0, \dots, N-1. \quad (5.1)$$

The amplitudes for all the frequencies from the record are 2 times the modulus of the complex elements of X_k with k ranging from zero to half the record length due to the symmetry. And the phase is equal to the four-quadrant inverse tangent of the imaginary and real parts of X_k .

5.1.2.2 Velocity boundary

The forcing at the open boundary is a velocity in the cross-shore direction. This velocity can be determined with the linear wave theory, the Stokes wave theory or the cnoidal wave theory. Which theory is used depends on the conditions found at the boundary. See the figure below for the ranges of applicability of the various wave theories, wherein H is wave height, h is the water depth and τ is the wave period.

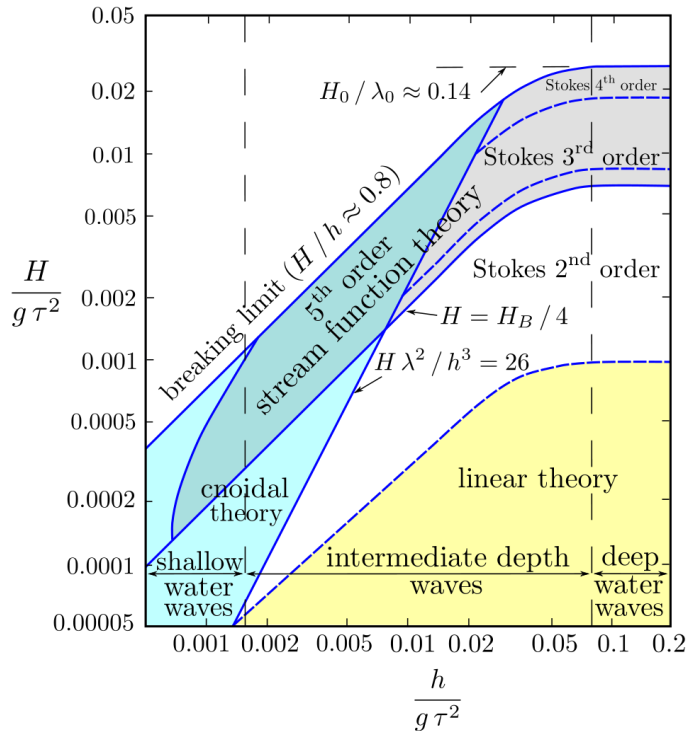


Figure 5-2: Water wave theories and their applicability

The linear wave theory is only applicable to waves with low steepness and in relative deep water to relatively intermediate water depth. This theory was used for case 1C to compute the depth averaged velocity from the amplitudes and phases of each wave component.

$$U^{in}(t) = \sum_{i=1}^N 2\pi \frac{f_i a_i}{k_i h} \cos(2\pi f_i \cdot t + \alpha_i) \quad (5.2)$$

Equation (5.2) is the incoming velocity at the boundary wherein α_i is the phase, a_i is the amplitude and f_i is the frequency of each wave component of the wave spectrum, k_i is the wave

number determined with the linear dispersion relation and h is depth at the boundary. For the calculation of the incoming velocity the low frequency waves are filtered out of the wave spectrum. So for $f_i < 0.2$ Hz the wave amplitude is set to zero. The reasons for doing so will become apparent later on in the chapter.

5.1.3 Setup

The grid size was set to 0.025 m which roughly amounts to 300 grid points for the peak wave. This is enough detail for the waves to be captured accurately. A coarser grid will reduce computational runtime, however for validation purposes first a fine grid was employed so that the results were without much numerical dissipation. The simulation time was taken equal to the duration of the wave measurement time, which is about 1700 seconds. The friction coefficient c_f was set to 0.15 [-]. The CFL condition was set to 0.5 [-].

5.1.4 Computations without viscosity

The first computations were done without the effects of viscosity. The results of these computations are presented in this paragraph. To illustrate the results of the computations the following figures are shown wherein the mean wave quantities, namely the significant wave height and the mean zero-crossing period, are compared to the measurement data. Also the spectra from the computations and experiment at different stations throughout the flume are compared and the wave setup or the mean water level is compared. These three comparisons give a good impression of how the model predicts the mean wave quantities needed for an accurate simulation of a rip current system, in which these wave quantities play a major role.

Figure 5-3 shows the comparison between the significant wave height and the zero-crossing period between the computation and the experiment for case 1C. For a large part the significant wave height is underestimated. This underestimation is directly from the offshore boundary onwards. The open boundary at the offshore side is the non-reflective boundary based on *Van Dongeren and Svendsen (1997)* and assumes incoming long waves and outgoing long waves. Due to this assumption the energy of the short waves entering the computational domain is slightly reduced when long waves leave the domain. This results in a lower significant wave height at the seaward boundary. The position where the significant wave height starts to decrease, due to breaking, is very well predicted. This is also true for the mean zero-crossing period. At the boundary the mean zero-crossing period is overestimated which is also due to the reflection from the shoreline of the low frequency waves. In the very shallow region ($x > 25$ m), not enough energy is dissipated and mean zero crossing period is underestimated. If viscosity is added to the model extra dissipation of the wave energy can be achieved in this region.

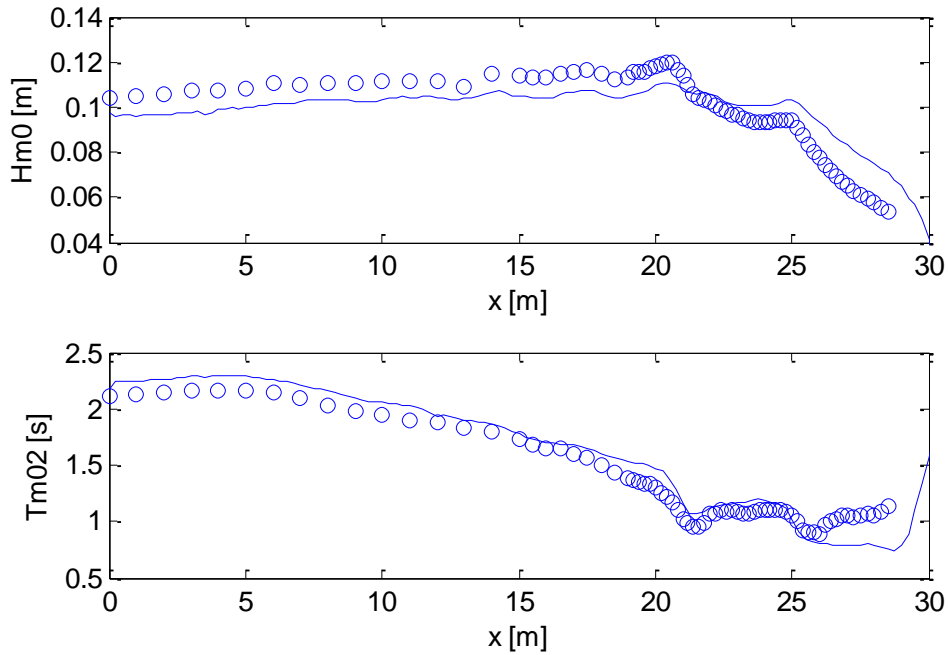


Figure 5-3: Computed (solid line) and measured (circles) significant wave heights (top panel) and mean zero-crossing periods (bottom panel) along the flumes (simulation without viscosity)

In Figure 5-4 a comparison is made between the spectra from the computation and experiment at different stations throughout the flume. The spatial evolution of the energy density spectrum has an amplification in both the sub- and super-harmonic ranges. This is consistent with the triad interactions of the waves. In the surf zone this transformation is more rapid and also the decrease in energy, due to wave breaking, is more noticeable. The further inshore from the breaker line the broader the shape of the wave spectrum, which is attributed to the nonlinear couplings and dissipation. In the computations one can see that the energy in the shallow region at the higher frequencies is overestimated. Dissipation due to viscosity is a subgrid process which was tried to capture using a proper conservation principle, however it apparently fails to dissipate enough energy beyond the breaking point. Also in the lower frequencies the energy is slightly overpredicted, the reflection of lower frequency waves can be the cause for this effect. The incoming low frequency waves, up to 0.2 Hz, as was mentioned in paragraph 5.1.2.2, have already been filtered out to reduce this effect. If these would not have been filtered out the overestimation would have been considerably higher. In conclusion, the simulation is in good agreement with the observed transformation of the spectrum throughout the flume including the surf zone and the shoaling region, where our main interest lies.

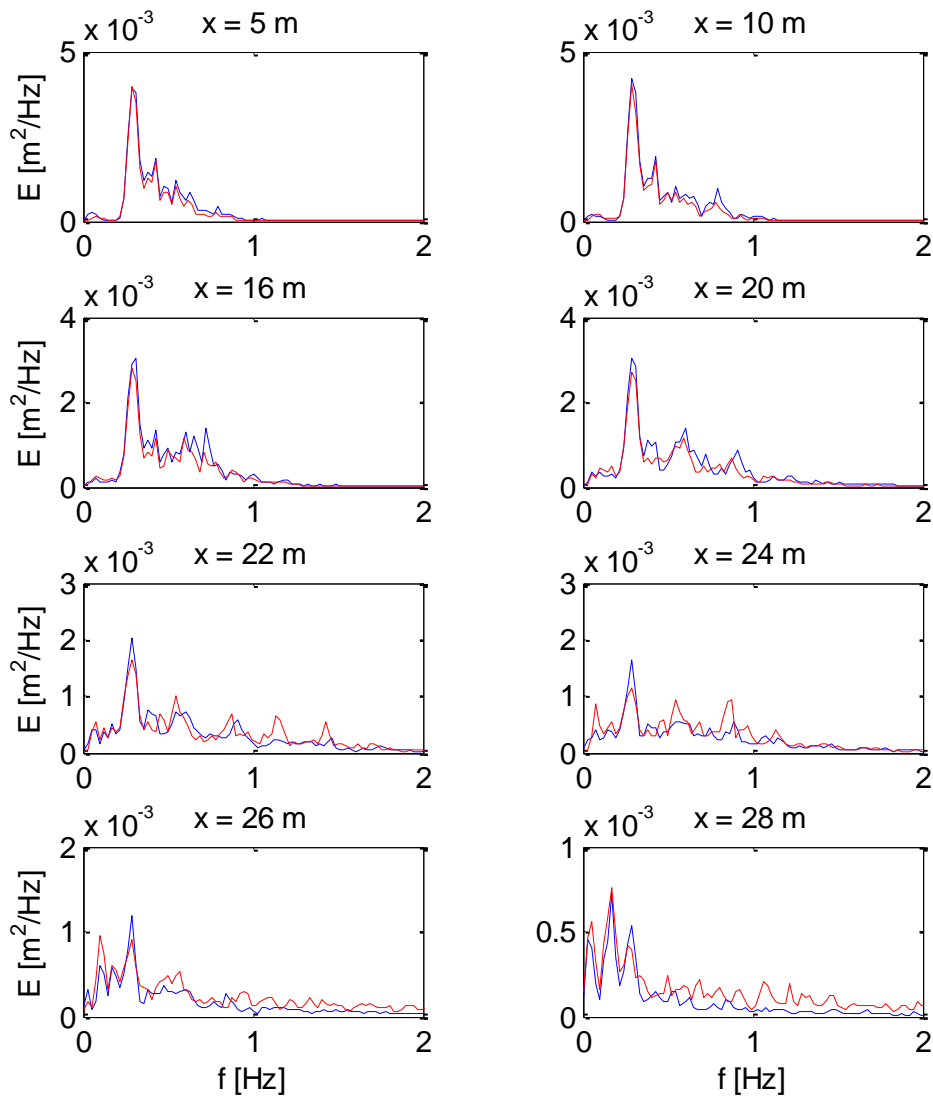


Figure 5-4: Computed (red line) and measured (blue line) energy density spectra at different stations in the flume. All spectra use equally spaced frequency intervals.

Also a good agreement with the measurements is needed with respect to the prediction of the wave-setup, which is an important aspect for the generation of a rip current. The following figure shows the comparison of the wave-setup between the computation and the flume test. In the shallower region the wave-setup is in fairly good agreement with the experimental results from the flume test. The computed wave-setup in the shoaling region and in the first part of the surf zone, however, is overestimated. Essentially, there is a net inflow of mass in the computational domain. The boundary condition based on *Van Dongeren and Svendsen* can cause this, due to the assumption that the incoming waves travel with celerity $c = \sqrt{gh}$. This is not the case as the incoming short waves travel with the phase speed from the linear wave theory at intermediate depth. A boundary condition based on the Sommerfeld radiation condition can be more appropriate for the short waves in the computation.

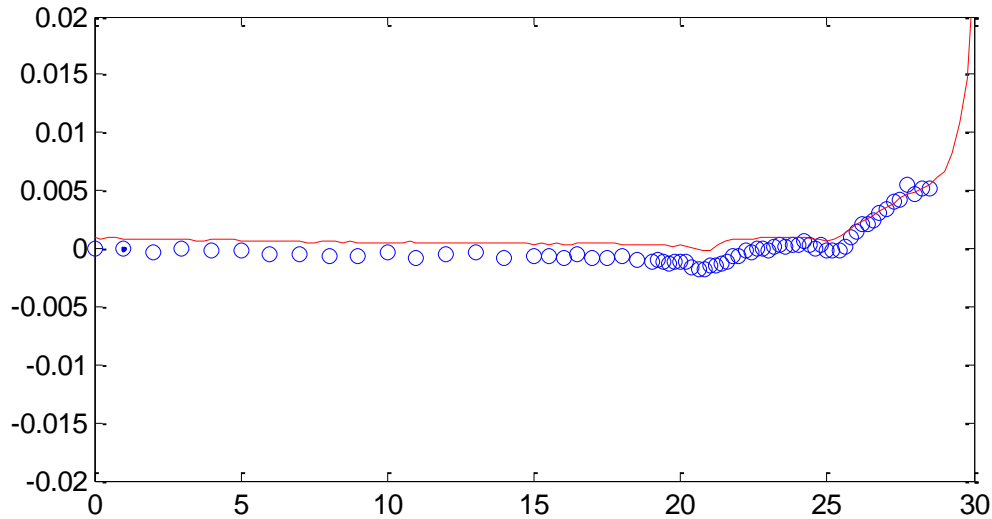


Figure 5-5: Computed wave-setup (red line) and the measured wave-setup (circles)

In the next paragraph first an attempt is made to add extra dissipation in the shallow region to decrease the overestimation of the significant wave height in the shallow region by adding a constant eddy viscosity stress term to the model.

5.1.5 Computations with a constant eddy viscosity

The numerical model is extended with a constant eddy viscosity so that more energy is dissipated in the shallow region. In the following figure the results regarding the significant wave height and zero-crossing period are shown. The value of the constant eddy viscosity was set to $\nu = 0.01 \text{ m}^2/\text{s}$.

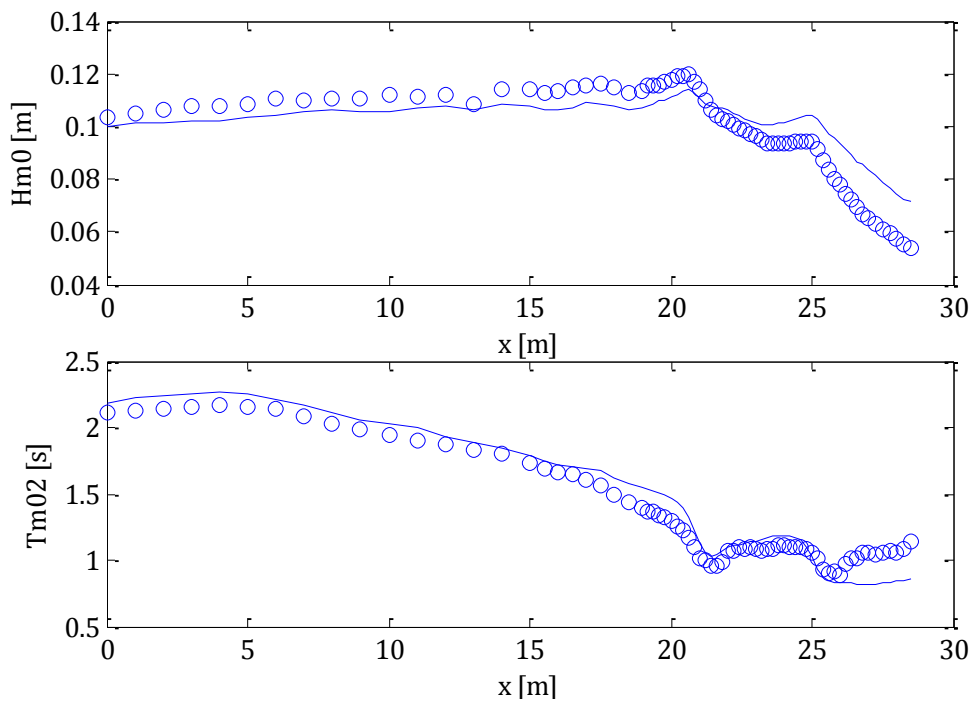


Figure 5-6: Computed (solid line) and measured (circles) significant wave heights (top panel) and mean zero-crossing periods (bottom panel) along the flume (simulation with a constant eddy viscosity)

In Figure 5-6 the wave height beyond the first breaker bar is still too high. The wave height is also reduced in the region before the first breaker bar. Increasing the viscosity gives better results in the region beyond the first breaker bar but also lowers the wave height in the region before the first breaker bar, where extra energy dissipation is not needed.

In Figure 5-7 the comparison is made between the wave energy density spectra of the computation and the experiment. The spatial evolution of the wave energy at the higher frequencies from deep to shallow water is better modelled than in Figure 5-4, as the viscosity in the model dampens the wave height and thus the energy. However, a large increase of the energy is seen in the very shallow region ($x > 22$ m) at the lower frequencies, compared to the computation without the turbulent mixing stress included. The higher frequency components are dissipated more rapidly due to the eddy viscosity into low frequency motions. The low frequency waves are not dissipated as rapidly due to the low gradients of the velocity in these waves. The overestimation of the low frequency waves can be caused by the boundary condition based on *Van Dongeren and Svendsen (1997)*.

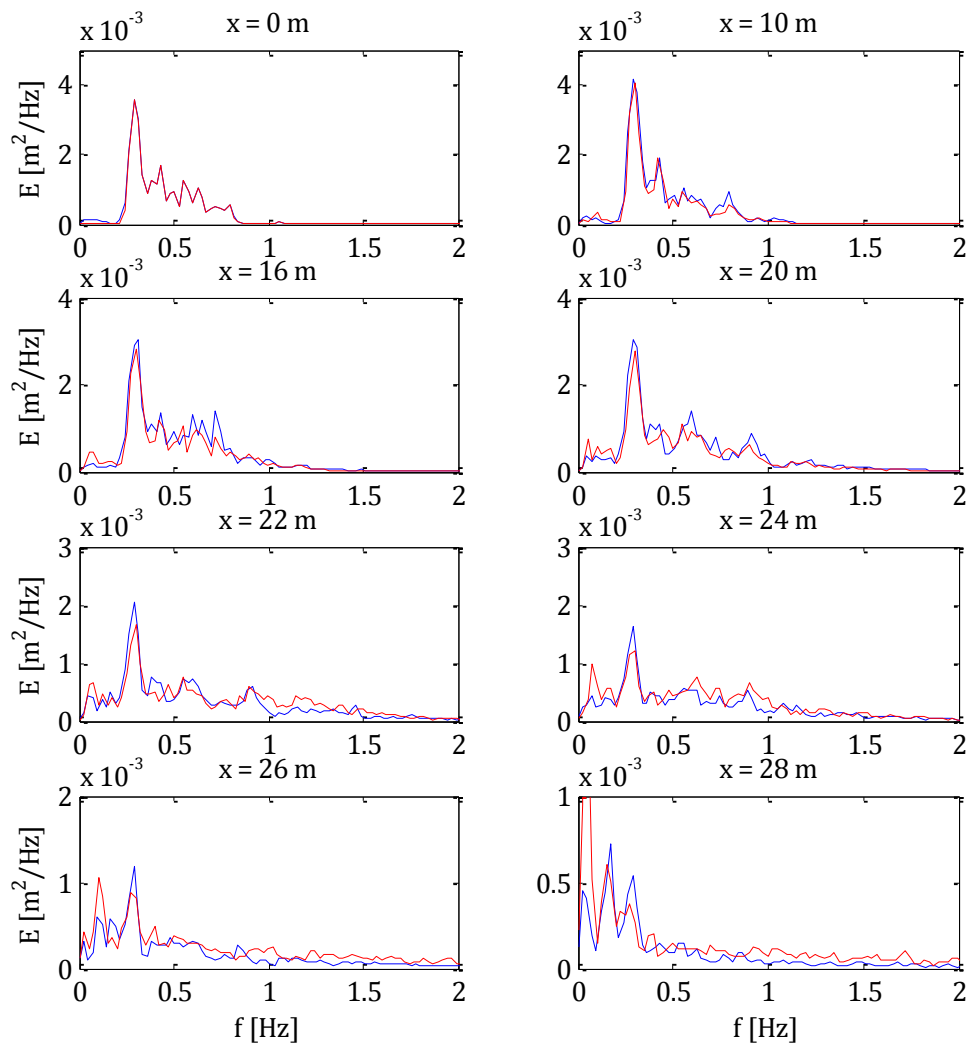


Figure 5-7: Computed (red line) and measured (blue line) energy density spectra at different stations in the flume. Computation with a constant eddy viscosity

5.1.6 Computations with a constant eddy viscosity and a new boundary condition

The model was run with a constant eddy viscosity of $\nu = 0.01 \text{ m}^2/\text{s}$ and with the boundary condition as described in Chapter 4, which is based on the Sommerfeld radiation condition. Figure 5-8 shows the significant wave height and the zero-crossing period. The wave height and the wave period at the boundary is almost the same as in the experiment. This is due to the use of the new boundary condition. In contrast to the boundary condition based on *Van Dongeren and Svendsen*, this boundary condition does not longer assume that the incoming wave celerity equals $c = \sqrt{gh}$. The propagation speed of the outgoing waves is still approximated as shallow water waves. This approximation is justified because the reflected waves are mostly long waves with a low frequency.

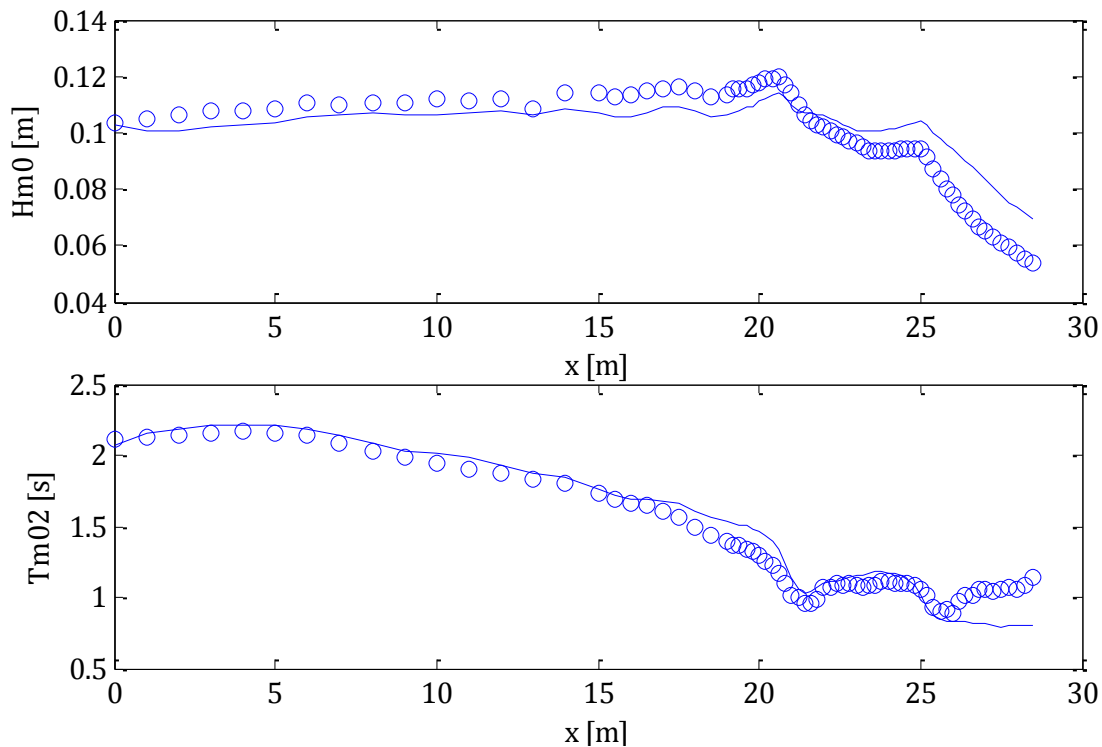


Figure 5-8: Computed (solid line) and measured (circles) significant wave heights (top panel) and mean zero-crossing periods (bottom panel) along the flume (simulation with a constant eddy viscosity and a new boundary condition)

In the above figure one can see that the significant wave height on the boundary is the same as the measured significant wave height, but is underestimated from the seaward boundary onwards. However, using a lower constant eddy viscosity coefficient is not preferred as then not enough energy is dissipated beyond the first breaker bar. Therefore, a Smagorinsky eddy viscosity model is an option, which scales the eddy viscosity to the gradient of the flow velocity. At places where a larger gradient of the velocity occurs more energy is dissipated. In the surf zone, where more dissipation is required, higher gradients of the flow occur due to wave breaking. Therefore the Smagorinsky eddy viscosity model could give improvements in this region. In the region before the first breaker bar the horizontal accelerations of the flow are not yet as high as beyond the point of breaking and therefore the Smagorinsky eddy viscosity model could also give improvements in this region.

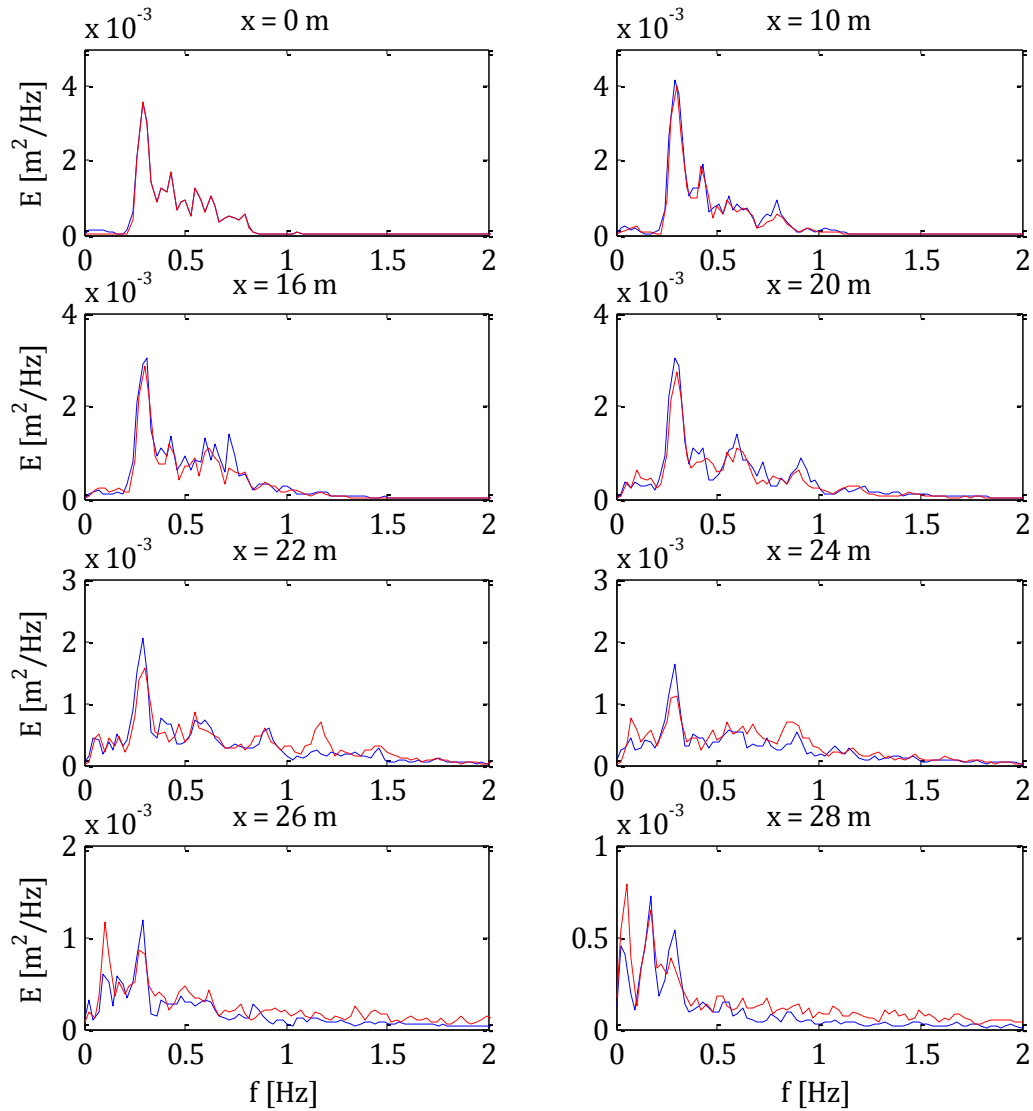


Figure 5-9: Computed (red line) and measured (blue line) energy density spectra at different stations in the flume (simulation with a constant eddy viscosity and a new boundary condition)

Figure 5-9 shows that the new boundary condition gives a big improvement in the very shallow region regarding the low frequency waves compared to Figure 5-7. However, compared to Figure 5-4 the result regarding the low frequency waves in the very shallow region ($x=28$ m) is still worse. Nevertheless the new boundary condition used in this computation is obviously better capable of non-reflecting the low frequency waves at the seaward boundary, which therefore reduces the low frequency wave energy in the shallow region. The low frequency wave energy in the deeper parts only amount to a small share of the total energy and the

overestimation is therefore not very obvious. For example the low frequency energy at $x=16$ m is much better in agreement in Figure 5-9 than in Figure 5-7. However Figure 5-9 shows that there should be more dissipation of energy at both the higher and lower frequencies beyond the first breaker bar ($x > 22$ m). In the next paragraph the Smagorinsky eddy viscosity model is being put to the test in the hope this will give better results.

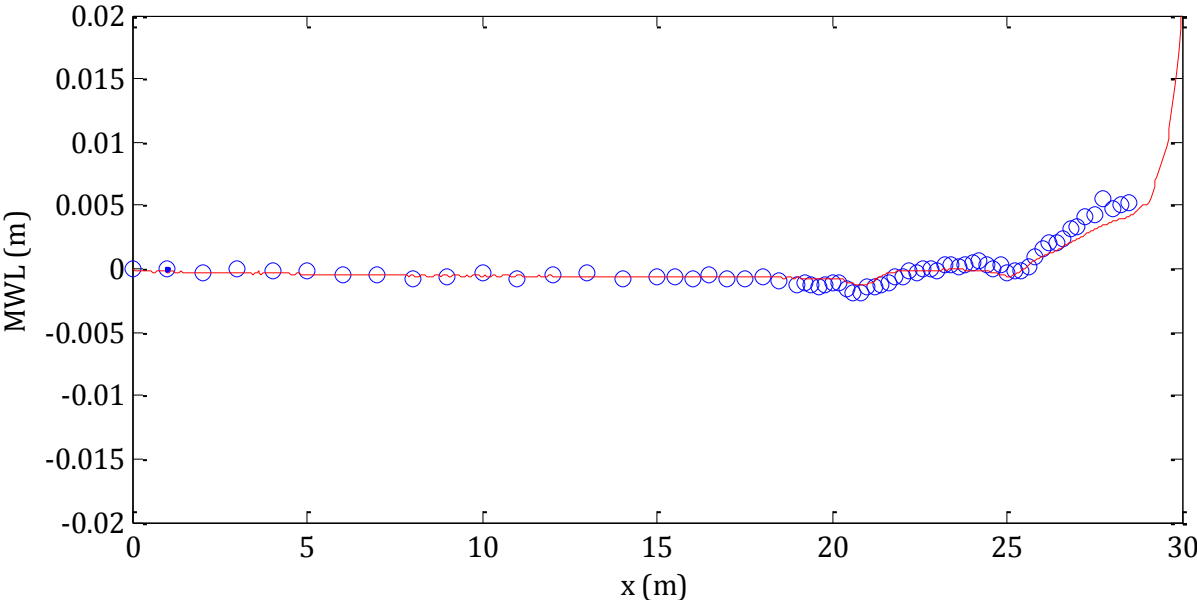


Figure 5-10: Computed wave-setup (red line) and the measured wave-setup (circles) (simulation with a constant eddy viscosity and a new boundary condition)

In the figure above one can see that the mean water level and the wave setup due to the new boundary condition is much better modelled. The boundary condition does not result in a net inflow of mass as was the case with the boundary condition of *Van Dongeren and Svendsen*.

5.1.7 Computations with a Smagorinsky eddy viscosity model

In the computations with the Smagorinsky eddy viscosity model, the mesh size is set to 0.05 m in x-direction and 1 m in y-direction, which amounts to 700 nodes, as this is a one dimensional case. The larger grid size drastically reduces the computational time and accuracy is not much reduced. At the offshore boundary the incoming wave is still captured by approximately 150 nodes. Therefore a coarser grid is justified as the incoming waves are still captured with enough detail.

In the following figure, again, a comparison is made between computation and experiment for the significant wave height and the zero-crossing period. A drastic improvement in the wave height beyond the first breaker bar is achieved with the inclusion of the Smagorinsky model. Also the wave period is much better modelled, especially from the second breaker bar onwards. However, the wave height at the crest of the first breaker bar is a bit underestimated, in other words, the wave energy is too much dissipated due to the viscosity but also due to the coarser

grid that was used. An improvement, again, can be realized by using a finer grid but keeping the Smagorinsky coefficient multiplied with the Smagorinsky length scale ($C_s\Delta_s$) a constant. So reducing the length scale means an increase of the Smagorinsky constant of an equal amount. The Smagorinsky model as used in the XBeach program is not a subgrid model as used in Large Eddy Simulations (LES). Unlike LES the XBeach model cannot contain subgrid eddies. The Smagorinsky model is used like a breaker model to add extra dissipation after a wave has broken and a bore is propagating. This bore is much more dissipative than an unbroken wave, and the model used for the research in this thesis does not distinguish between a bore and an unbroken wave. However, large gradients in the flow do occur in a bore and therefore a Smagorinsky model works so well. The square of the Smagorinsky constant multiplied with the square of the length scale ($C_s^2\Delta_s^2$) was, in the one dimensional case with Δy set to 1 m and $C_s=0.2$, equal to 0.002 m². This value gave the best results.

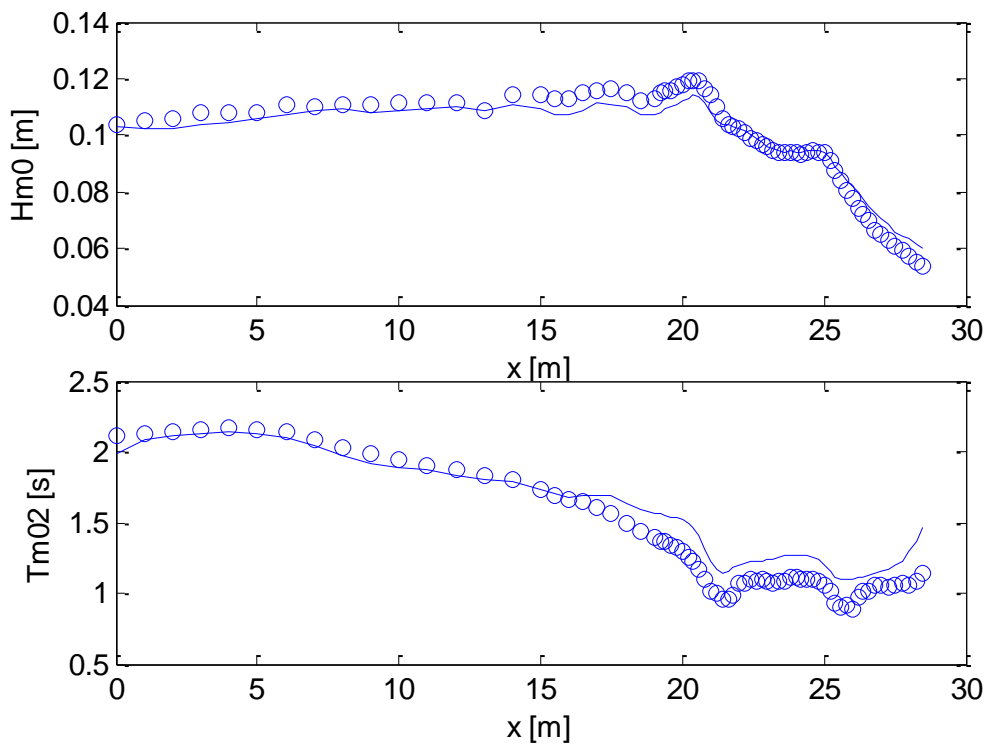


Figure 5-11: Computed (solid line) and measured (circles) significant wave heights (top panel) and mean zero-crossing periods (bottom panel) along the flume (simulation with Smagorinsky viscosity model and coarser grid)

In Figure 5-12 the significant wave height and the zero-crossing period is shown with the grid size set to 0.01 m, however keeping $(C_s\Delta_s)^2=0.002$ m². The figure shows an almost perfect agreement for the wave height but the zero-crossing period is still a little overestimated around the first breaker bar. The zero-crossing period is, however, not the most reliable estimated characteristic wave period due to the fact that the second-order moment of the variance density spectrum is sensitive to small errors or variations in the measurement or analysis technique. Another mean period is the T_{m01} , which is less dependent on high frequency noise. The T_{m01}

shows a better agreement in the surf zone than the T_{m02} , however the T_{m01} is slightly worse near the seaward boundary.

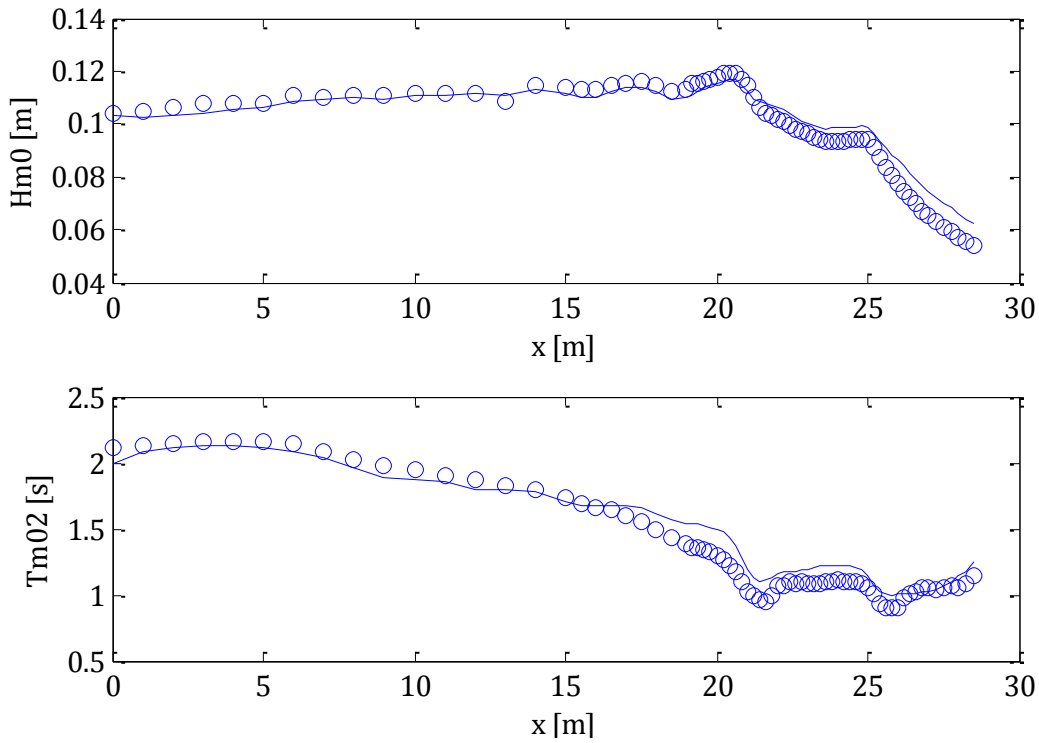


Figure 5-12: Computed (solid line) and measured (circles) significant wave heights (top panel) and mean zero-crossing periods (bottom panel) along the flume (simulation with Smagorinsky eddy viscosity and denser grid)

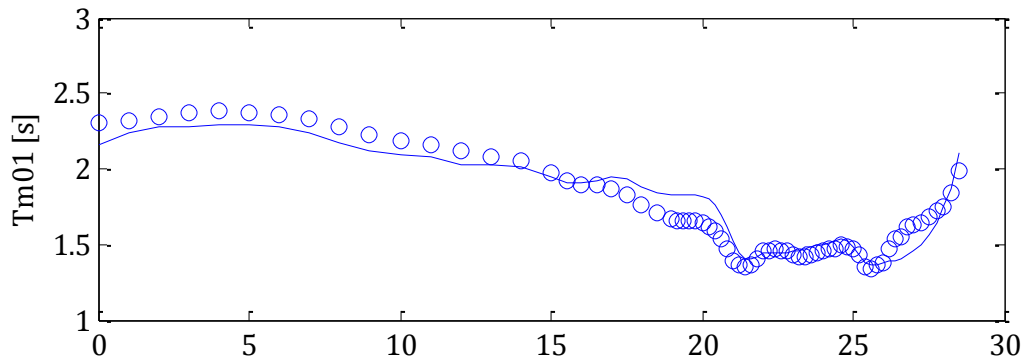


Figure 5-13: Computed (solid line) and measured (circles) mean period along the flume (simulation with Smagorinsky eddy viscosity and denser grid)

In the above figure the mean period is still overestimated in the shoaling region before the first breaker bar, but it does show better agreement with the measurements beyond the first breaker bar.

In Figure 5-14 the wave energy at the higher frequencies and also in the very low frequencies is modelled more in compliance with the measurements in contrast to the simulation with the constant eddy viscosity. Due to the higher eddy viscosity in regions with higher gradients of the flow velocity, such as just beyond the breaker bars, the wave energy is dampened more.

However there still seems to be an overestimation of the very low frequency waves close to the shoreline. Apparently the flow gradient in these low frequency waves is not high enough for the eddy viscosity model to dissipate their energy.

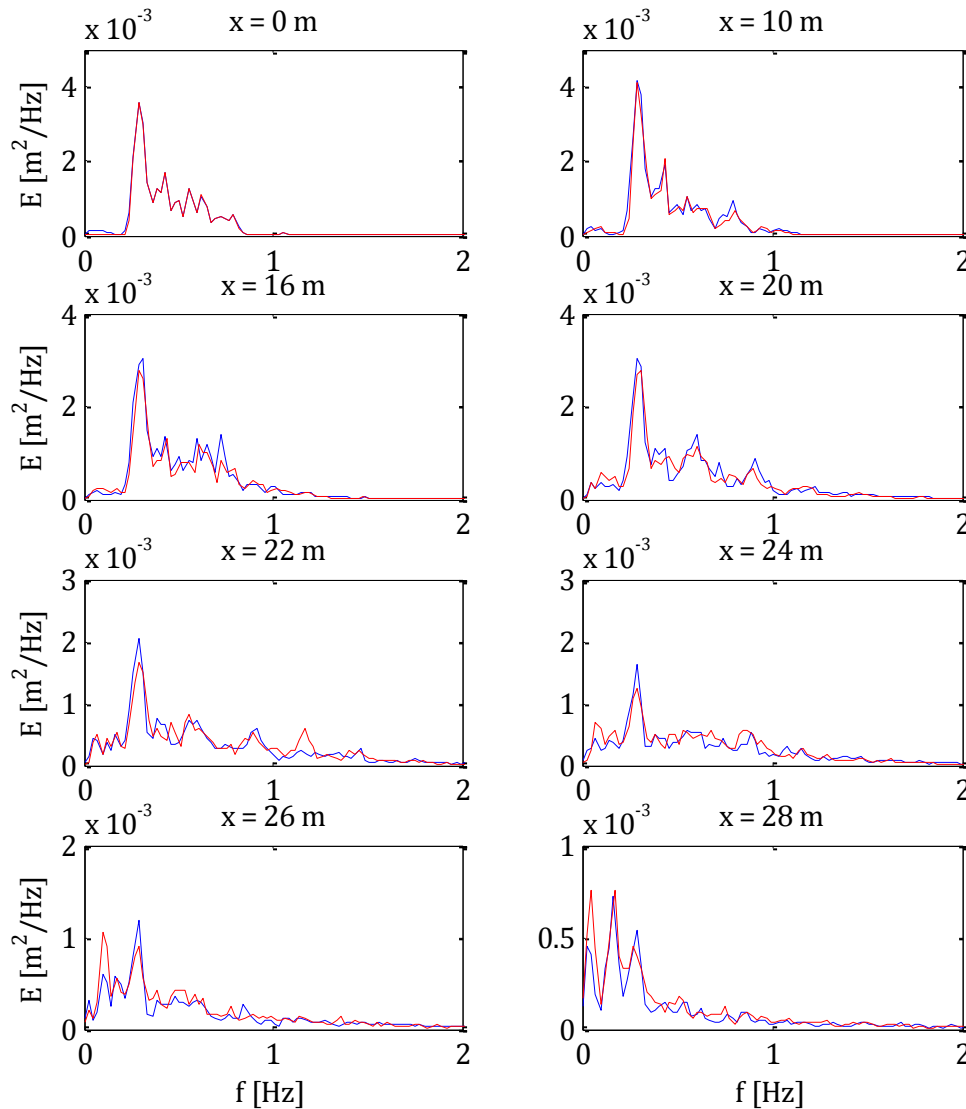


Figure 5-14: Computed (red line) and measured (blue line) energy density spectra at different stations in the flume (simulation with the Smagorinsky eddy viscosity model)

Another important measure is the wave setup. In Figure 5-15 a comparison is made of the wave-setup between the model with the added Smagorinsky eddy viscosity model and the flume experiment. The computed overestimation in the shoaling region and in the first part of the surf zone, as was the case in the computation without viscosity, has disappeared and the modelled wave setup in this region is now in good agreement with the measurements. In the shallower region the wave-setup is still in good agreement with the measurements.

In Figure 5-16 a comparison is given between the surface elevations of the computations and the measurements along four longshore sections. The sections are; (a) just before the first breaker

bar, (b) just behind the first breaker bar, (c) before the second breaker bar and (d) behind the second breaker bar.

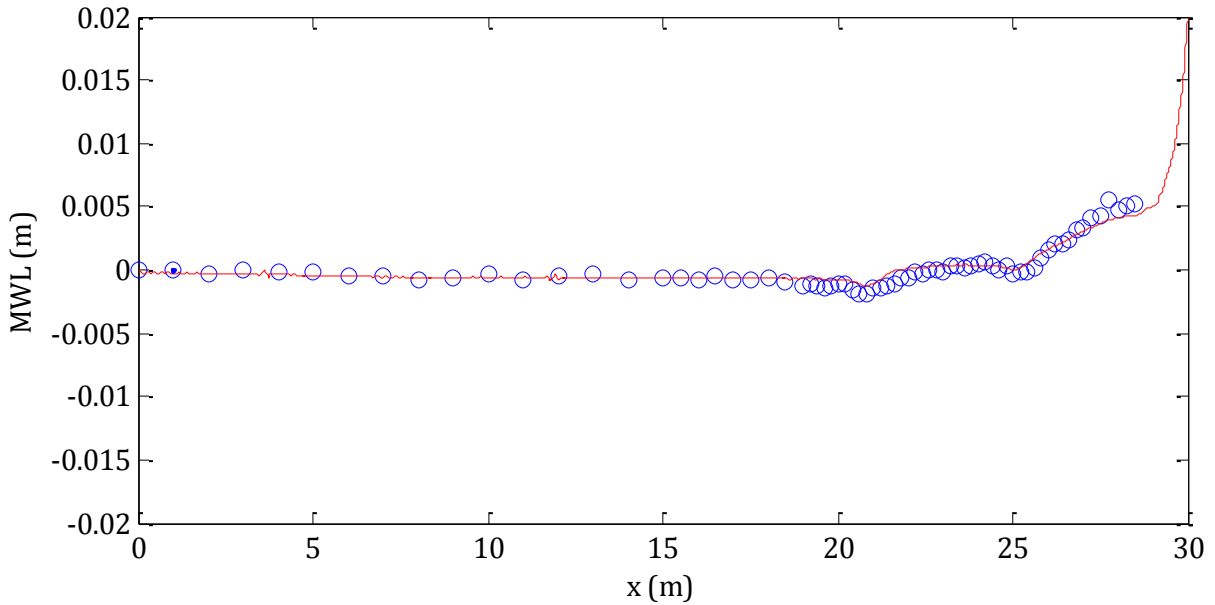


Figure 5-15: Computed wave-setup with the Smagorinsky eddy viscosity model (red line) and the measured wave-setup (circles)

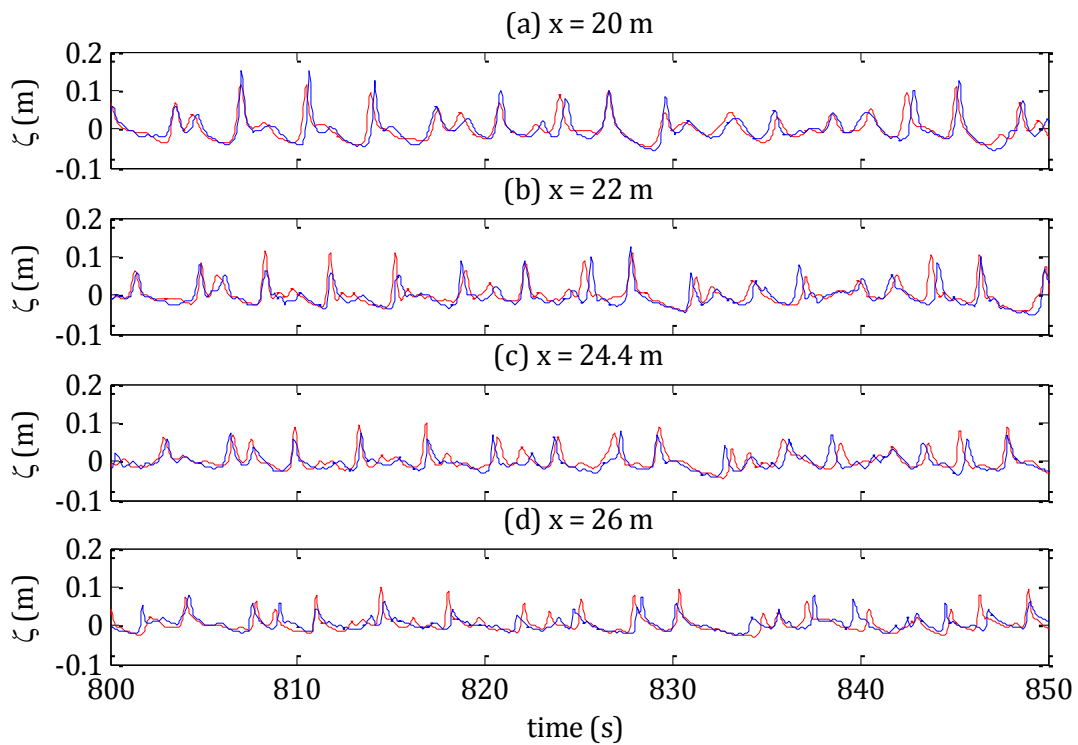


Figure 5-16: Comparison of the surface elevation between the computation (red line) and the measurements (blue line)

The above figure shows that the model has a good accuracy in the instantaneous surface elevation and not only in the mean wave characteristics, although the individual crest heights are sometimes either a little overpredicted or underpredicted.

5.2 Experiments on rip currents and nearshore circulation

5.2.1 Introduction

Rip currents and their effects on nearshore circulation have been observed qualitatively in the field for many years now (e.g. *Shepard et al.*, 1941), however it is also established that comprehensive data sets involving rip currents in the field are difficult to obtain. In the laboratory the environment is more easily controlled and therefore the data is qualitatively better and a more comprehensive data set can be gathered. There are, however, not many laboratory data sets involving rip currents on a longshore varying bathymetry. In fact, rip current experiments have only been performed by *Hamm* (1992), *Drønen et al.* (2002) and *Haller et al.* (2002), of which the experiment of *Haller et al.* is the most comprehensive. The data set from this experiment is used as validation material for the numerical model XBeach for the bathymetry driven nearshore circulation.

The measurement data from the experiment of *Haller et al.* were obtained in a directional wave basin with a longshore bar, in which two rip channels were present. The experiment was carried out using several incident wave conditions, but all were regular waves and no random waves were produced by the wave maker.

The flow velocity, wave height and mean water level were measured over a large area of the wave basin to get a detailed picture of the circulation pattern of the rip current system. For these measurements ten capacitance wave gages were used to measure time series of the water surface elevation during the experiments. For the time series of the horizontal currents three 2-D side-looking Acoustic Doppler Velocimeters (ADV's) were used. These ADV's were placed three centimeters above the bottom of the basin.

In the experiment it was obvious that the rip current system consisted of two circulation patterns. The larger circulation cell was shown to consist of the rip current and the feeder current. The second, smaller, circulation cell was counter-rotating to the main circulation cell and was closer to the shoreline. Also the measurements showed that the rip current was unstable and that the current had a low-frequency oscillation in strength.

The numerical model Xbeach, as was verified in the previous paragraph, is used to simulate the circulation patterns that were found during the experiments of *Haller et al.* (2002), induced by the monochromatic normally incident waves on a beach with a longshore bar and two rip channels.

The propagation of the uniform wave train over the longshore bar and the channels creates variability in wave height and wave breaking, and thus variability in the dissipation of wave energy in the region behind the longshore bar. This again creates a longshore variability in wave setup, which is the main driver for the feeder currents and the rip current system. The dynamics of the rip current system were also explained in Chapter 2. The smaller circulation cells, shown in Figure 2-2, are created because of the higher waves at the shoreward side of the longshore bar in the channels close to the shoreline. The high waves in the channels break earlier than the waves behind the bar. This creates a larger setup near the shoreline, resulting in a longshore

gradient of pressure which drives the flow away from the channels. The breaking pattern is of great importance for the flow pattern. If the waves do not break over the bar then the method outlined above is eliminated. Also, if the waves in the channel break strongly then the longshore surface gradients are reduced, which will then again reduce the rip current.

5.2.2 Topography

The topography under consideration is taken from a detailed survey in the wave basin and is shown in Figure 5-17. The intention of the experiment was to create a plane sloping bottom and two equal symmetric rip channels. However, as it turned out, there were some differences between the two channels and also the bars exhibit some longshore nonuniformities.

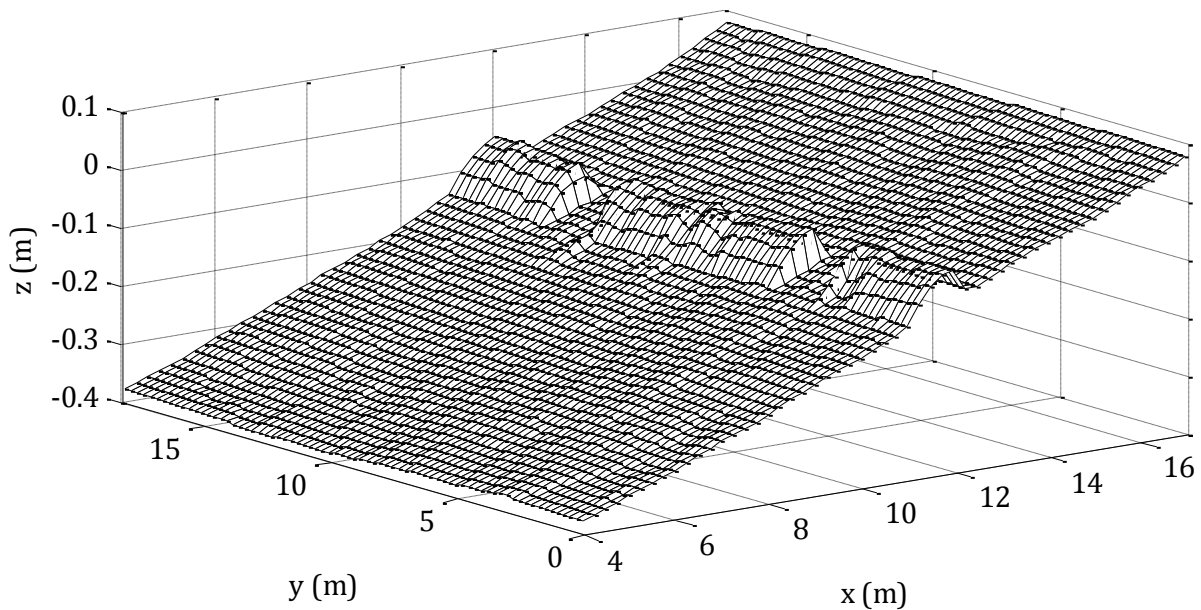


Figure 5-17: Topography of the wave basin

5.2.3 Boundary conditions

Our simulations provide a direct comparison with the measurements from test B of the experiment. This test consisted of normally incident waves with a wave height of 4.75 cm and a period of 1 s. During the experiment there were 30 runs made with these wave conditions. This was in order to create a map of the circulation system with a dense spatial resolution due to the limited number of ADV's available for the experiment. This test contains the most extensive spatial map of the currents, but it is important for validation that the different runs do not contain a large variability in the wave conditions. The offshore wave gage remained stationary for the entire test B and represents the best estimate of experimental repeatability. It turned out that the standard deviation σ_H of the mean wave height (H_m) was 0.06 cm and the percent variability ($\%var=100*\sigma_H/H_m$) was approximately 1 percent for Test B. The variability during the experiment for the different runs regarding the mean water level was also very small. This allows for the use of all the runs for comparison with one simulation with the mean wave height and the mean water level at the boundary.

The velocity at the boundary is determined with the linear wave theory from the surface elevation measured at the offshore wave gage. In our simulations the wave generating boundary

is therefore set at the location of the most offshore wave gauge, which is at 3.95 m from the wave maker. This gives a more precise forcing of the model in conjunction with the experiment. Also the kH value is lower here due to the lower depth which is around $kH = 1.5$ [-]. See Figure 5-18 for the wave gauge locations and the locations of the ADV's for test B and Figure 5-19 for the boundary velocity and surface elevations.

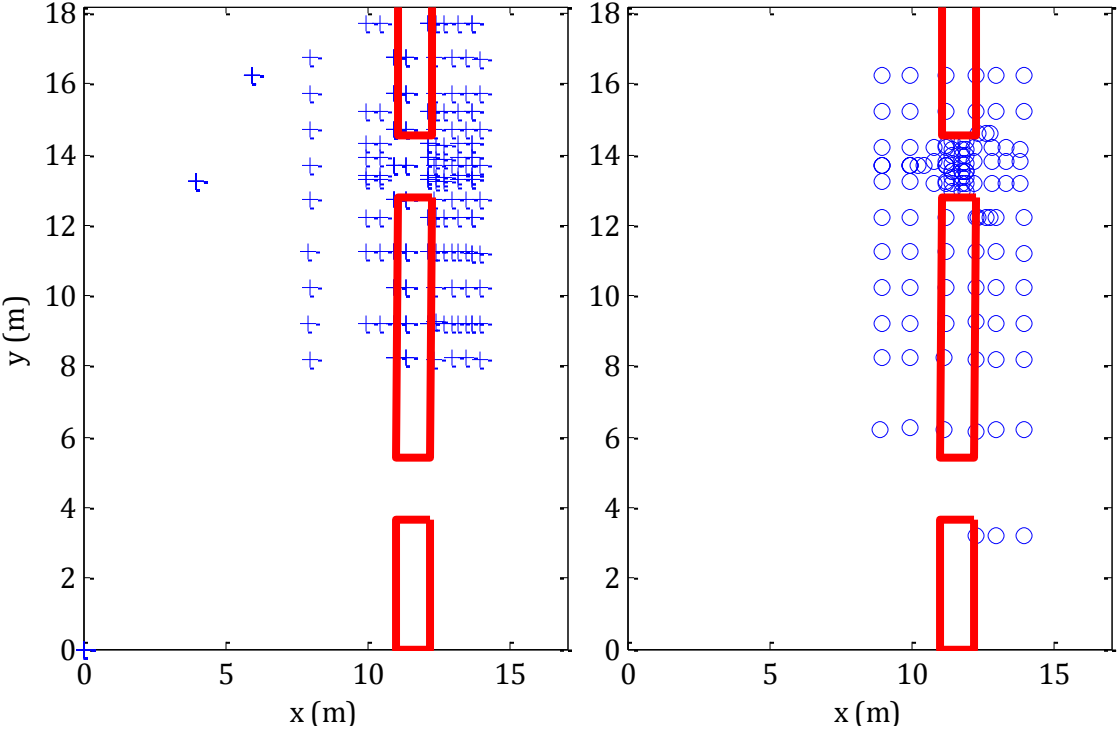


Figure 5-18: Wave gauge locations (left) and current meter locations (right) for test B.

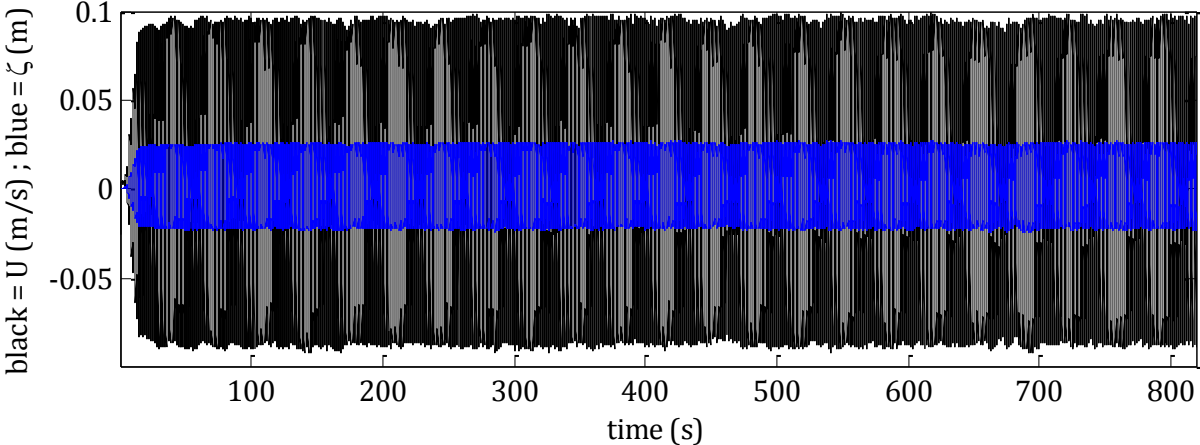


Figure 5-19: Time series of the measured surface elevation and the computed cross-shore velocity at the most offshore wave gauge.

5.2.4 Numerical setup

The model grid spacing is $\Delta x=5\text{cm}$ and $\Delta y=5\text{cm}$, and the Courant number is chosen at 0.9. The number of grid points per wavelength approximately 30. The model is run for the full length of the experimental run, so for 1638 seconds. In addition the time averaging is done over the second half of the run to avoid start-up effects. The friction coefficient c_f and the Smagorinsky

eddy viscosity constant are based on standard values which can be found in the literature and are equal to respectively $c_t=0.0025$ [-] and $C_s=0.2$ [-]. The Smagorinsky length scale is equal to $\Delta_s = \sqrt{\Delta x \Delta y} = 0.05$ m.

5.2.5 Results

In Figure 5-20 the run averaged circulation pattern from the computation is shown. Due to the longshore nonuniformities of bathymetry the circulation patterns in both rip channels are not symmetric. The figure also shows that a part of the two rip currents are converging offshore in the center of the wave basin and that this results in an offshore cross-shore current behind the center breaker bar. In Figure 5-25 at $x=10$ m and $y=8$ m it shows that the experiment does not show this behavior as strongly. An explanation can be found in a different vortex shedding pattern, in which the upper rip current and lower rip current are converging more than in the experiment.

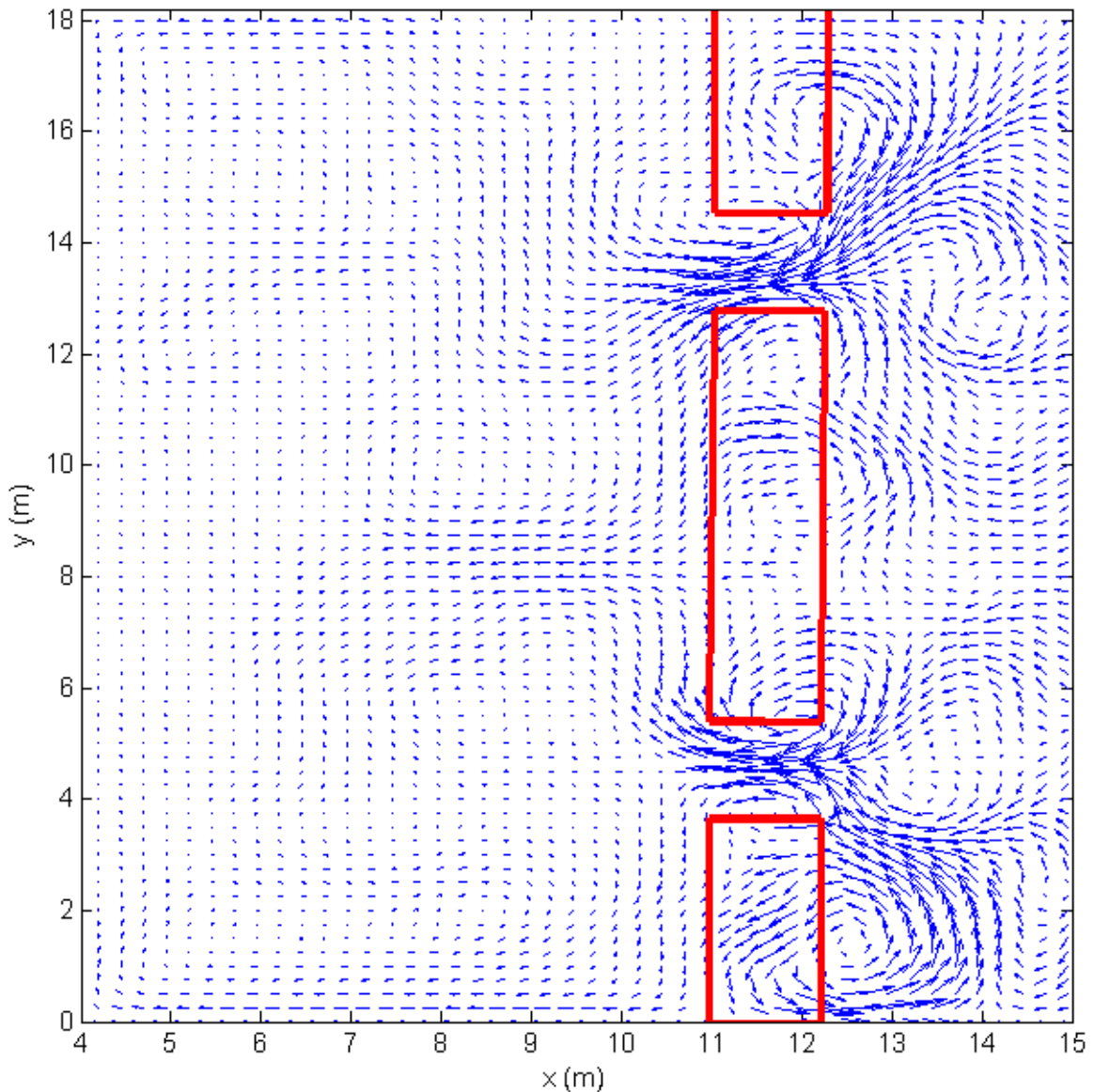


Figure 5-20: Run averaged flow field

In Figure 5-21 the instability of the upper rip current is shown. The figure shows eight snapshots of the computed velocity and vorticity. The model simulates the vortex shedding and the meandering of the rip side-to-side. The rip current is constantly changing direction and also varying in strength. This means that the rip current is unstable and also pulsating in strength. The reason for this is the wave-current interaction that takes place. The current slows down the wave and therefore increases its height. This causes the wave to break further offshore, which then locally increases the wave setup and thus partly eliminating the pressure gradient in the longshore direction behind the breaker bar. This decreases the rip current velocity and therefore a less pronounced wave-current interaction follows, which then decreases wave height and the process starts over again. This causes the pulsating behavior of the current.

The vortex shedding can be explained as the vortices moving from high pressure to low pressure, this changes the direction of the main rip current flow (also known as a Von Karman vortex street). The general circulation pattern can only be found by averaging over a longer time interval, as is done in Figure 5-20.

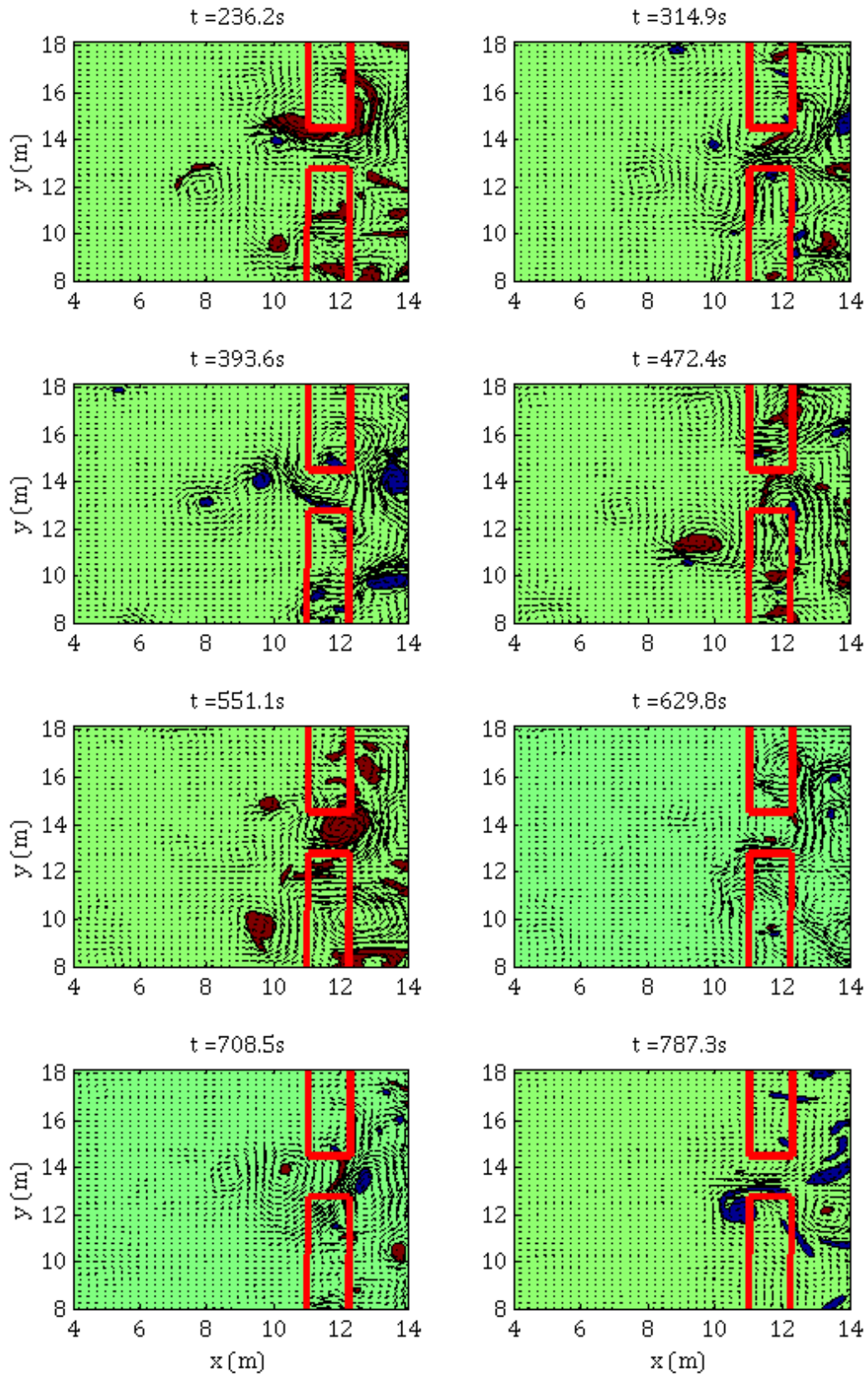


Figure 5-21: Snapshots of vorticity and velocity vectors averaged over two wave periods from the simulation. Red represents negative and blue represents positive vorticity. Only the upper half of the computational domain is shown.

In Figure 5-22 a comparison is made between the velocities from the experiment and the velocities from the simulation averaged over the second half of the run. The velocities from the experiment are only measured at the locations of the ADV's, so to make a good comparison the velocities from the simulation are also plotted at the same locations. Due to the limited number of ADV's available for each run only a time averaged comparison can be made for the horizontal flow velocities, as each run has again a different pattern of vortex shedding due to the high instability of this phenomenon. In the figure it shows that the computation is in good agreement with the experiment. The direction and length of the velocity vectors in the rip channel are similar although the computation has a larger mean velocity in the lower part of the channel and the direction is a bit more at an angle compared to the experiment. The experiment shows a larger velocity in the upper part of the channel. The feeder currents are very similar in the computation and in the experiment.

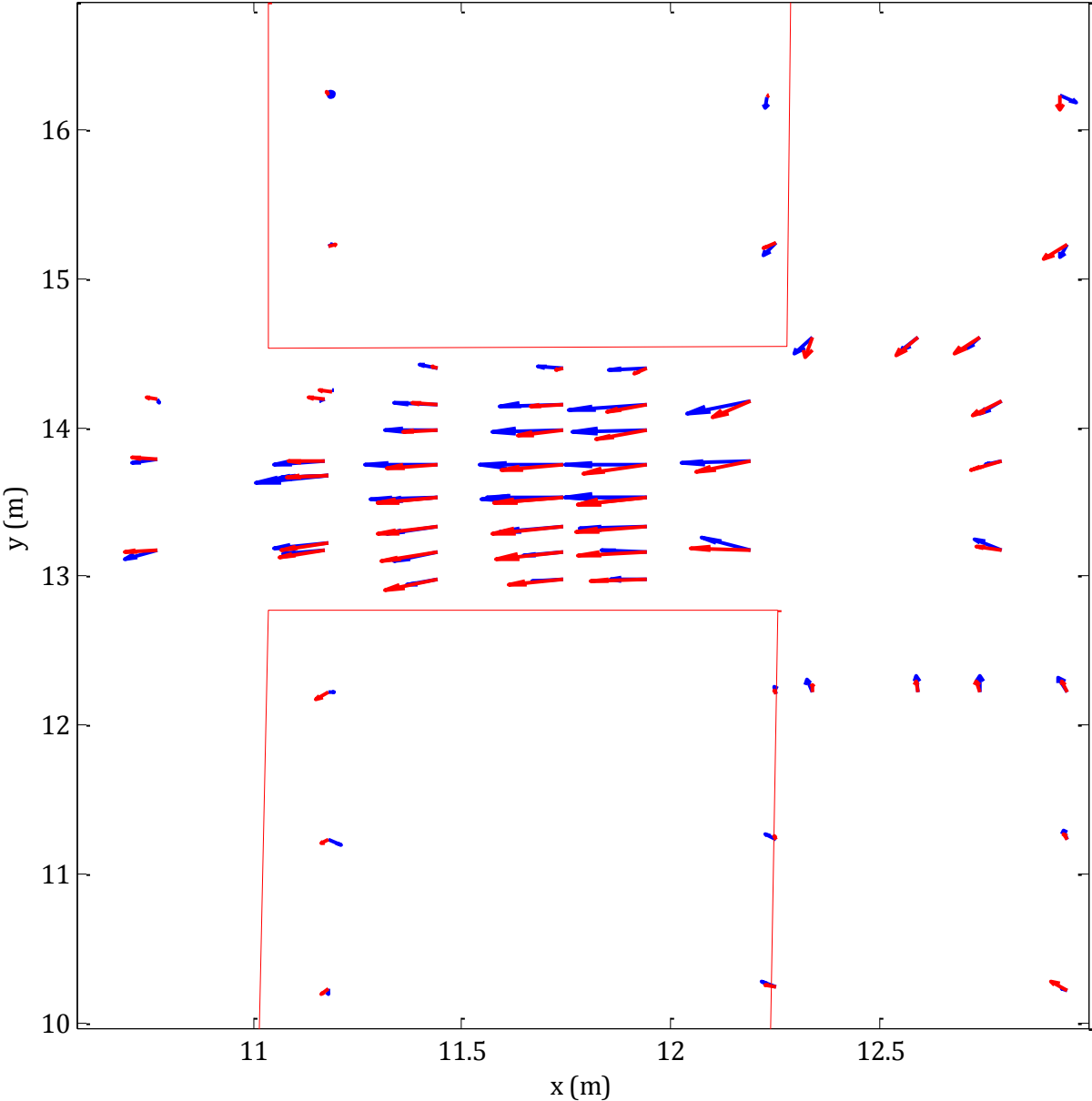


Figure 5-22: Run averaged velocity vectors from experimental data (blue vectors) and simulation (red vectors).

Figure 5-23 shows a comparison between the measured and computed mean wave height along five longshore sections. The sections are (a) close to the shoreline, (b) in the trough behind the bar, (c) over the bar, (d) on the offshore edge of the bar, and (e) 1 m offshore of the bar. The bar is located between $x=11$ m and $x=12.4$ m. All five sections demonstrate reasonable agreement between the measurements and computations.

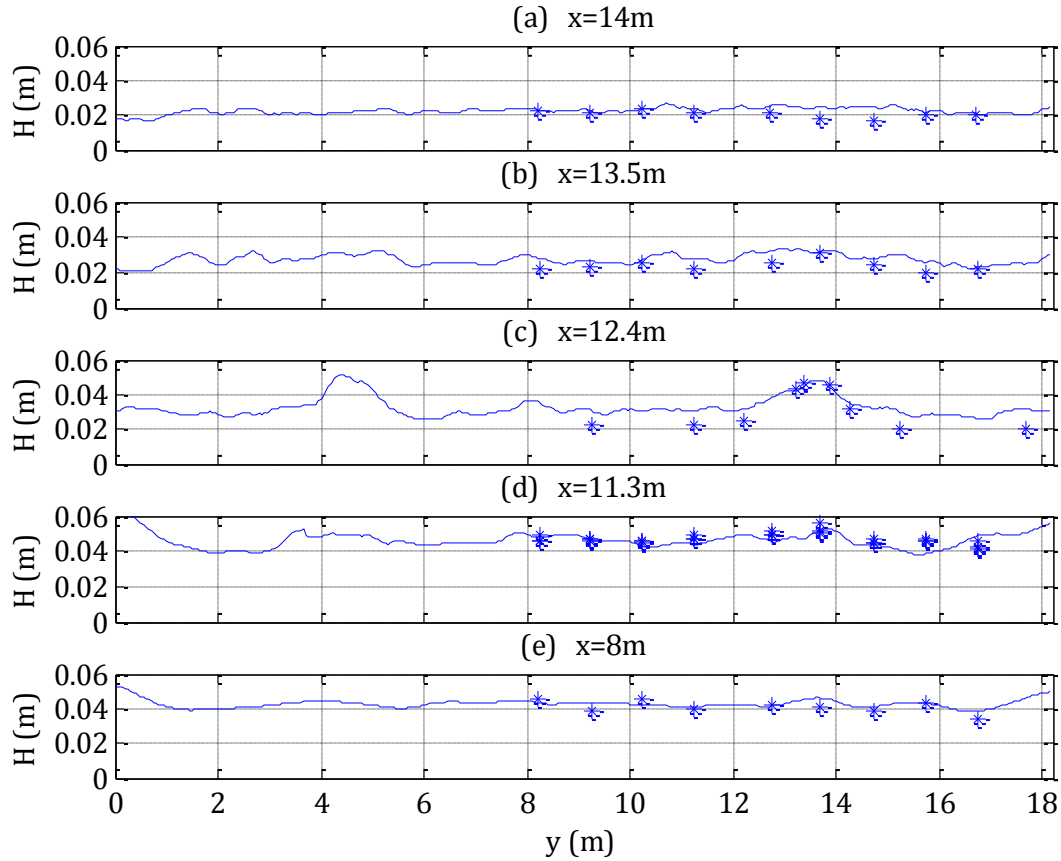


Figure 5-23: Comparison of time-averaged modelled wave height (line) to experimental data (asterisk)

The accuracy of the modelled wave height is quantified using the index of agreement between model/data according to *Willmott* (1981). This is written as follows

$$d = 1 - \frac{\sum_{j=1}^n [y(j) - x(j)]^2}{\sum_{j=1}^n [|y(j) - \bar{x}| + |x(j) - \bar{x}|]^2} \quad (5.3)$$

Where $x(j)$ are the measured data, $y(j)$ the computed data, and \bar{x} is the mean of $x(j)$. A value of $d = 1$ indicates perfect agreement, and a value of $d = 0$ indicates total disagreement. For the computation of d , all measured points are used. The value of d_H for the wave height in our case is 0.95, which is better than the value of *Chen et al. (1999)* and *Haas et al. (2003)* which was $d_H = 0.92$.

In Figure 5-24 a comparison is made between the measured mean water level and the computed mean water level. The same longshore sections are taken as in Figure 5-23. The agreement for

all the sections is reasonable. In the trough region the depression in $\bar{\zeta}$ near the channel is modelled well.

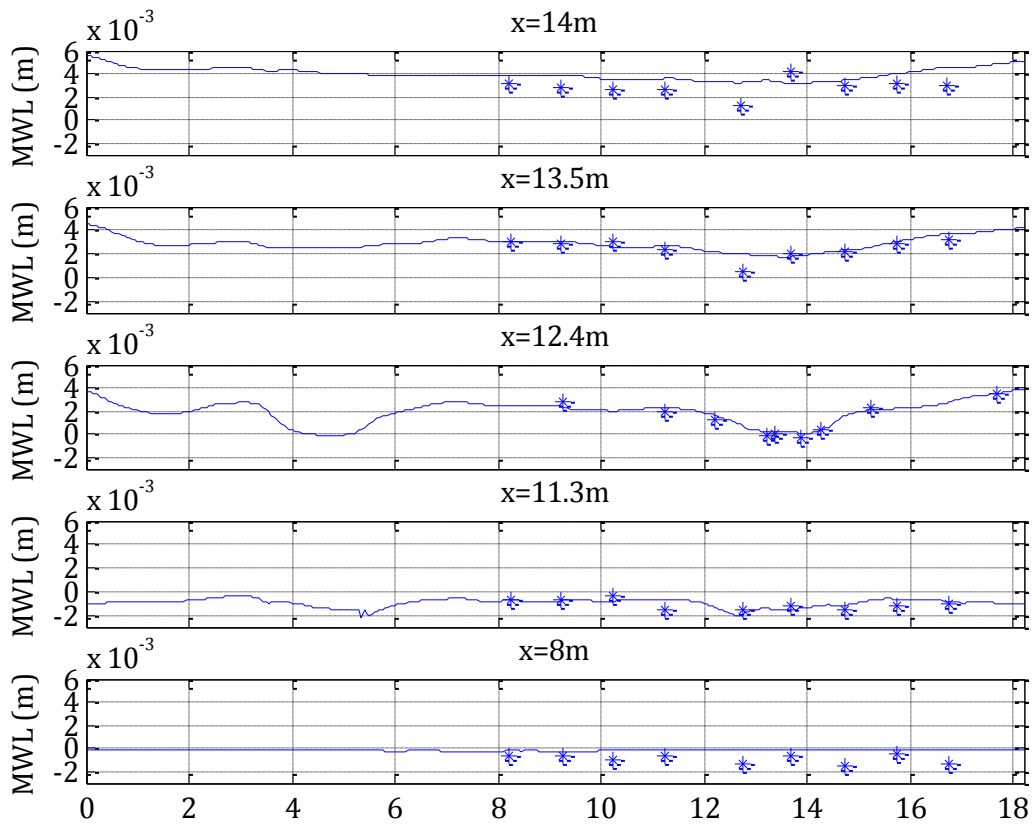


Figure 5-24: Comparison of time-averaged modelled mean water level (line) to experimental data (asterisk).

The mean water level has a $d_{\zeta} = 0.98$, which shows that the pressure gradients are modelled well, and better than the values achieved by *Chen et al.* (1999) and *Haas et al.* (2003), who had a value of $d_{\zeta} = 0.96$.

The cross shore velocity from the measurements and the computed cross-shore currents are compared in Figure 5-25. The agreement is fairly good for the five longshore sections. Close to the shoreline at $x=14$ meter the longshore variation is modelled well. The peak currents occur at the center of the rip channels, although no measurements were conducted here close to the shoreline. At the shore side of the bar, at $x=12.2$ m, the cross-shore currents are accurately represented. The average velocity in the rip channel at $y=13$ m is in good agreement. Also at the offshore side of the bar, at $x= 11.2$ m, the model seems to catch the important details of the longshore variation of the cross-shore current. The measured velocities in the rip channel at the offshore side of bar ($x=11.2$ m) show that the measurements have a quite a large variability. However the computed velocity in the upper rip channel ($y=13$ m) is in good agreement with lower measured velocities. Further offshore, at $x=10$ m, the averaged cross-shore current is close to zero which is in agreement with the measurements, however at $y=8$ m the cross-shore current is slightly larger as was mentioned previously. Although, the same longshore section

shows that the variability of the measurements here is quite high, as can be seen at $y=13.8$ m. Here measurements are taken in the same location of different experimental runs and show different results as is also the case at the longshore section $x=11.2$ m at $y=13.8$ m. A cause is the chaotic vortex shedding of the rip current offshore of the longshore breaker bar, which can be completely different in each run.

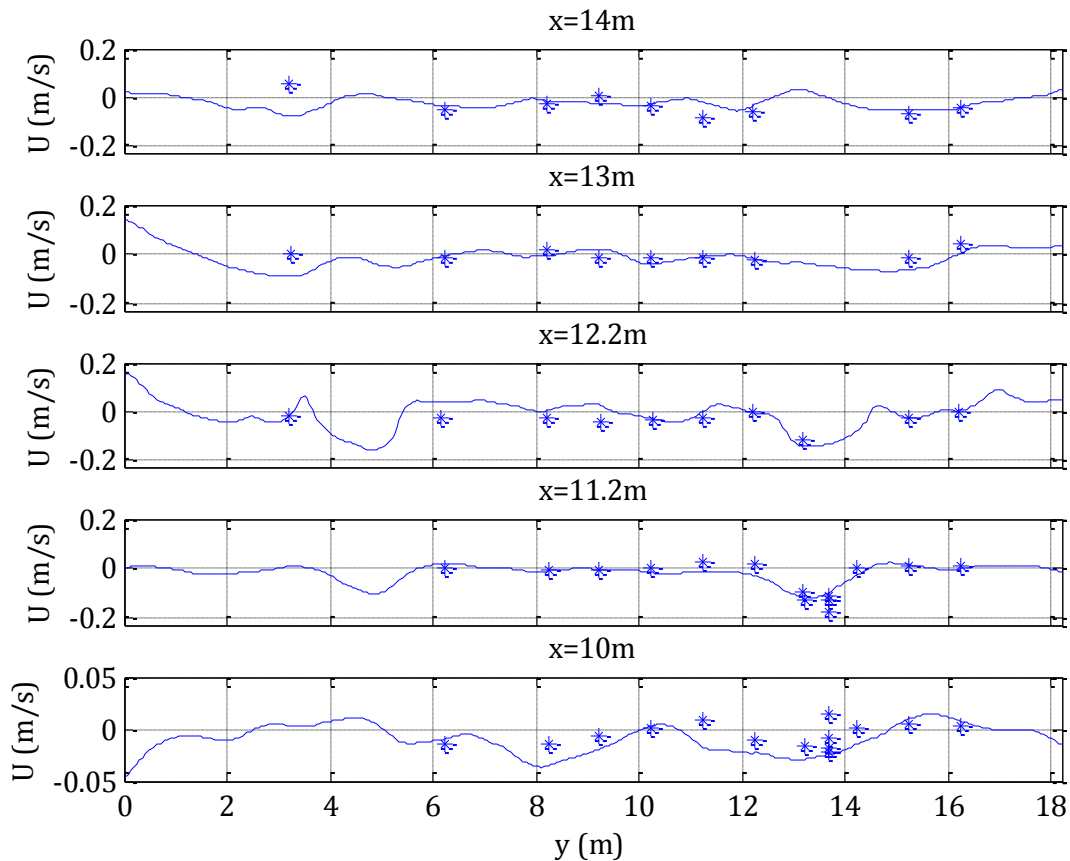


Figure 5-25: Comparison of time-averaged cross-shore currents (line) to experimental data (asterisk)

More detailed comparisons between the measurements and the computations of the cross-shore velocity in the rip channel are shown in Figure 5-26. The simulated velocities in the rip channel, as we have seen in Figure 5-22, are in good agreement in the channel. However, the computed velocities are a bit higher in the left part of the channel ($12.8 < y < 13.3$), and a bit lower in the right part of the channel. However the computed velocity does show to agree well with the measurements in the sense that the line of the modelled cross-shore currents goes right between the measurements. The index of agreement for the cross-shore currents is fairly good, with $d_U = 0.95$. This is again a bit better than the results from *Chen et al.* (1999) and *Haas et al.* (2003).

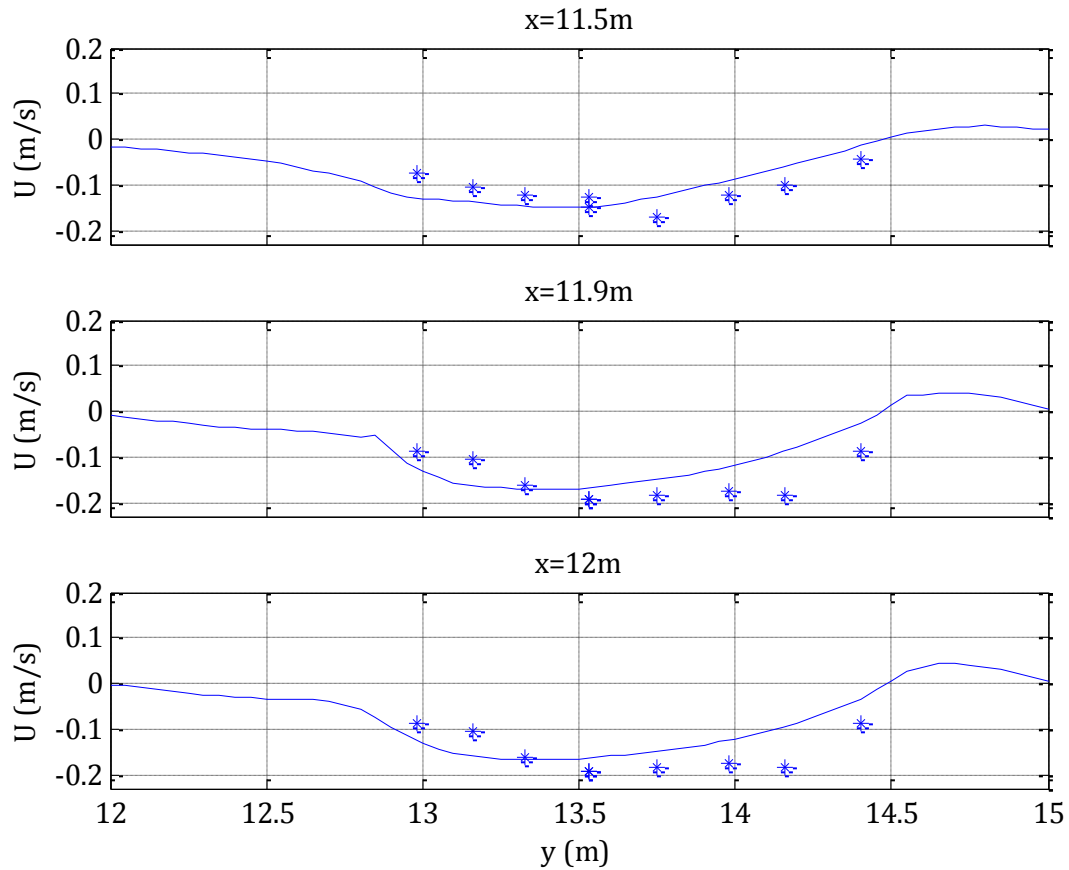


Figure 5-26: Comparison of time-averaged modelled cross-shore currents (line) in the channel to experimental data (asterisk)

Figure 5-27 shows the longshore current velocity from the measurements compared with the modelled longshore current velocity. The modelled current velocity is in good agreement with the measured longshore current velocity. In every longshore section the agreement is good although there are some small differences. The index of agreement for the longshore currents is $d_V = 0.88$. In summary, the results of the model simulation indicate a good agreement with the measured data for the waves, mean water level and the currents.

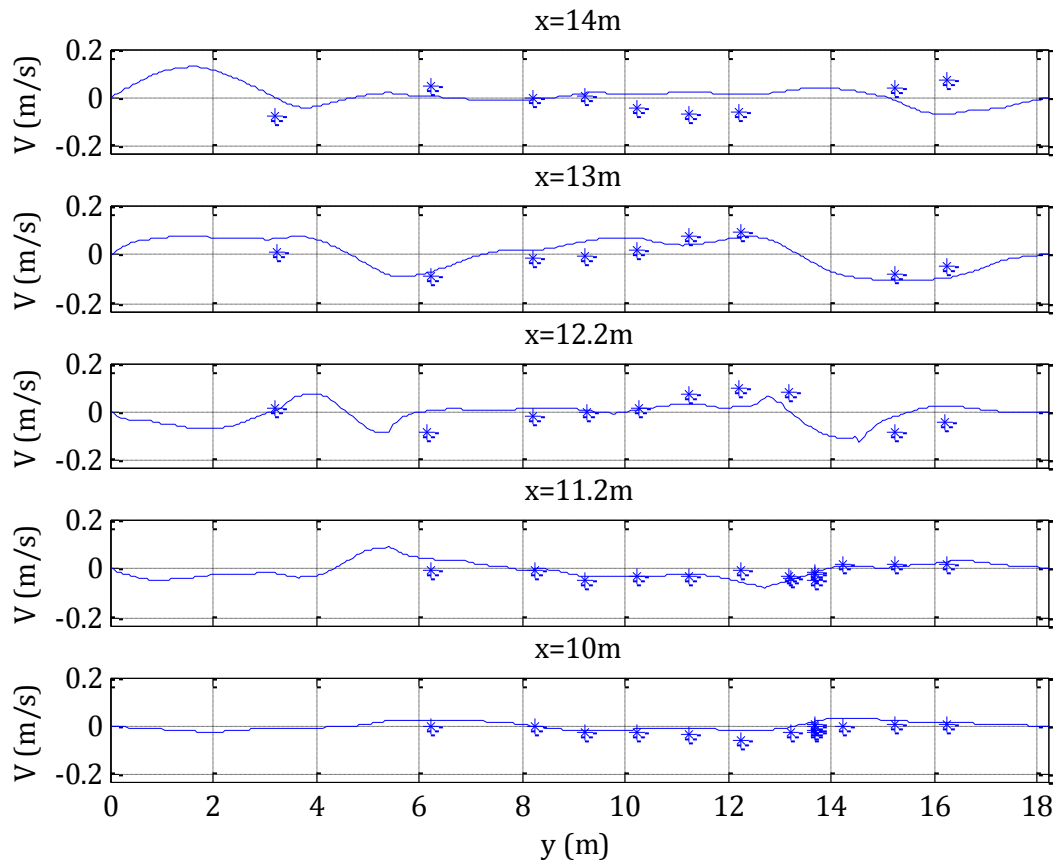


Figure 5-27: Comparison of time-averaged modelled longshore currents (line) to experimental data (asterisk)

5.3 Conclusions

First the numerical model XBeach has been put to the test to replicate the measured data from the flume experiment conducted by *Boers (2005)*. The model showed to be very accurate with the Smagorinsky eddy viscosity model and the boundary condition based on the Sommerfeld radiation condition, as described in Chapter 4. The significant wave height and the wave setup are modelled in very good agreement with the experiment. This is important for the test case with rip current system as these are the main drivers for the rip current.

The numerical model XBeach has also been used to simulate the currents generated in a closed directional wave basin and compared with the experiments by *Haller et al. (2002)*. The time-averaged flow properties from the model are compared with the time-averaged measurements, and the overall results show good agreement between the model and laboratory data. The *Wilmott (1981)* index of agreement between the model and data is found to be quite good and in all cases better than the values found by *Chen et al. (1999)* and *Haas et al. (2003)*. Thus the computations with the model provide a good insight into the mechanisms of the rip current circulation, more than can be gained from the measurements alone.

First, it is noted that the rips in the two channels behave differently. The rip in the upper channel, where most of the measurements were taken, is much stronger than the rip in the

lower channel. The cause for this difference is that the depth in upper half ($y > 7$ m) of the basin is greater causing more flow toward the upper rip channel leading to a stronger rip current.

From the study of *Haas et al.* (2003) it was concluded that the wave current interactions play an important role in rip current systems. Observations during the laboratory experiments indicated that the feedback mechanism of the wave-current interaction resulted in a slow pulsation of the rip current. They also found the influence of the bottom stress to play a significant role. The bottom stress is one of the two uncertain parameters in the simulation, together with the Smagorinsky constant. A higher bottom stress in the simulations of *Haas et al.* gave a more stabilized rip current flow. The flow still meandered but only at the seaward end and the flow in the channel was steadier. However the instantaneous peak velocity decreased.

From the simulations it is also noted that wave current interaction and vortex shedding has a negative feedback on the stability and strength of the rip current system. For a rip current system to work for energy extraction the impact of these mechanisms should be reduced.

6 Conclusions and recommendations

The objective of this study was to accurately simulate the fluid motions in the nearshore zone with the use of the numerical model XBeach, in which a non-hydrostatic model based upon the numerical scheme as developed by *Stelling and Zijlema (2003)* was implemented. After the model was further developed and validated, an investigation was undertaken in how the wave induced current velocity could be increased. In this section the results found in the study will be presented together with recommendations for future development and research.

6.1 Conclusions

6.1.1 Numerical model

The depth averaged XBeach program (*Roelvink et al., 2009*), with the add-on of the non-hydrostatic model based upon *Stelling and Zijlema (2003)* and modified to second order accurate in both time and space and including a dynamic eddy viscosity model, appears to give very promising results regarding the simulation of the nearshore zone dynamics. The full transformation of short waves from deep water to breaking and beyond is accurately modelled. Also accurate results were obtained regarding the wave induced horizontal flow circulation found on a barred beach with rip channels.

The most interesting result was the big improvement from the added dynamic eddy viscosity model, which was based on the Smagorinsky subgrid eddy viscosity model. The result especially improved in the region beyond the breaking line of the waves. The eddy viscosity model adds more dissipation to the model in areas where high gradients of the flow occur. Without an eddy viscosity model the simulation proved not to give enough dissipation in these regions.

6.1.2 Application to the nearshore zone

The model is proven to give accurate results in the nearshore zone with a good efficiency thanks to the depth averaged approach. Also the model is very robust and not much tweaking is needed in contrast to a lot of Boussinesq models, which have to include numerous extra terms to the momentum equations in order to accurately model the surf zone dynamics. The grid size, the friction coefficient and the eddy viscosity parameter are the only parameters that need to be chosen carefully. The grid size should not be too small in order to include enough numerical dissipation, however extra dissipation can be achieved by increasing the eddy viscosity parameter, but a fine grid will reduce efficiency, and not too big in order to capture enough detail of the incoming waves. For the incoming waves 30 nodes per wave length is usually enough detail.

For the application to the nearshore zone two experimental studies were considered. The first experiment was a flume experiment with irregular waves on a barred beach. The results from the non-hydrostatic model together with the added eddy viscosity model were very satisfactory, especially regarding the significant wave height and wave period. Also the wave spectra and the wave setup were accurately predicted. The results achieved from this test case gave confidence

that sufficiently accurate results could also be achieved for the second test case which consisted of a more complicated bathymetry involving all the nearshore zone dynamics.

The results achieved from the second test case were also very good, better than the results achieved by *Chen et al.* (1999) and *Haas et. al.* (2003). The model is therefore competitive to Boussinesq-type models in terms of accuracy. If the model is also competitive in terms of efficiency is unknown. The rip current test case consisted of 95.630 grid points and took about 9 hours and 20 minutes to complete a run of about 1700 seconds on an Intel Core 2 Duo @ 3.00 GHz CPU. The model, however, is not optimized for a dual core processor.

6.2 Recommendations

6.2.1 Numerical model

The numerical model XBeach, as it is, has a good balance between accuracy and efficiency. The model can be made more accurate by adding a second layer, however from the computations from *Smit* (2008) it was concluded that the two layer approach only marginally improved the results and adding a second layer will increase computational time significantly.

Additionally even more layers could be added to the model to improve the dispersion characteristics and to find the vertical distribution of the flow. However this would significantly reduce efficiency due to more computational effort needed to solve the non-hydrostatic pressure matrix, as the size of this matrix is equal to the number of grid points multiplied by the number of layers that are employed. However, one can keep the size of the matrix equal to the size as in the one layer case by assuming a hyperbolic pressure distribution of the dynamic pressure in the vertical. The dynamic pressure at the surface and the vertical gradient of the dynamic pressure at the bottom are assumed to be zero, and the value of the depth integrated dynamic pressure is assumed to be equal to half of the total pressure at the bottom. Together with the linear vertical distribution of the hydrostatic pressure and the hyperbolic vertical distribution of the dynamic pressure, the momentum equations in the multiple layers are calculated with this distribution in mind. Extra computational effort is needed for solving the momentum equations in the multiple layers and the calculation of the vertical dynamic pressure distribution. However the Poisson pressure equation is only solved for the dynamic pressure at the bottom, just as is the case in the one layer approach.

6.2.2 Application to the nearshore zone

The first next logical step with regard to the application to the nearshore zone would be to try and model a real world event. This would build more confidence in the application of the model and could also lead to some interesting insights. Furthermore comparisons should be made to existing Boussinesq models.

List of main symbols

Roman symbols

| Symbol | Description | Unit |
|--------------------|---|--------------------------------|
| c | Wave celerity | m /s |
| c_g | Group velocity | m /s |
| d | Depth, measured positive downward from z_0 | m |
| g | Gravitational acceleration | m/s ² |
| H | (i) Water depth (ii) Wave Height | m m |
| i | Mesh point index (subscript) | [-] |
| j | Mesh point index (subscript) | [-] |
| k | Wave number | rad /m |
| k_x, k_y | Wave number components | rad /m |
| L, L_x, L_y | Typical Flume/Basin/Area length | m |
| p | Normalized dynamic pressure | m ² /s ² |
| p_0 | Atmospheric pressure | N /m ² |
| P | Pressure | N /m ² |
| q_x, q_y | Specific discharge in the x-/y-direction | m ² /s |
| t | Time | s |
| T | Wave period | s |
| \mathbf{u} | Velocity vector | m /s |
| u | x-component of the velocity vector \mathbf{u} | m /s |
| \mathbf{U} | Depth averaged velocity vector | m /s |
| U | x-component of the depth averaged velocity \mathbf{U} | m /s |
| $U_{i,j}$ | Discrete velocity U | m /s |
| v | y-component of the velocity vector \mathbf{u} . | m /s |
| V | y-component of the depth averaged velocity \mathbf{U} | m /s |
| $V_{i,j}$ | Discrete velocity V | m /s |
| w | z-component of the velocity vector \mathbf{u} . | m /s |
| W | Depth averaged vertical velocity | m /s |
| $W_{i,j,b}$ | Vertical velocity at $z = -d(x)$ | m /s |
| $W_{i,j,z}$ | Vertical velocity at $z = -\zeta(x,t)$ | m /s |
| \mathbf{x} | Point at (x,y) | m |
| \mathbf{X} | Point at (x,y,z) | |
| $\mathbf{x}_{i,j}$ | Point at (x_i, y_j) | |
| x | Principle horizontal coordinate | m |
| x_w | World coordinate | m |
| x_0 | World x-coordinates of origin. | m |
| $x_i, x_{i+1/2}$ | x-location of i th -gridline | m |
| y | Lateral horizontal coordinate | m |
| y_w | World coordinate | m |
| y_0 | World y-coordinate of origin. | m |
| $y_j, y_{j+1/2}$ | y-location of j th -gridline | m |
| z | Vertical coordinate | m |
| z_0 | Reference level | m |

Greek symbols

| Symbol | Description | Unit |
|---|---|-------------------------|
| Δ_s | the characteristic length scale of the smallest resolvable eddy | m |
| Δx_i | Local mesh interval in x-direction | m |
| Δy_j | Local mesh interval in y-direction | m |
| $\delta\Omega$ | Rectangular shaped boundary curve of domain Ω | m |
| $\delta\Omega_{\text{back}}$ | “Back” boundary, usually a land boundary | m |
| $\delta\Omega_{\text{front}}$ | “Front” boundary, usually the Seaward boundary | m |
| $\delta\Omega_{\text{left}}, \delta\Omega_{\text{right}}$ | “Left/right” boundaries of the domain | m |
| ζ | Free surface elevation, measured positive upwards from z_0 | m |
| L | Wave length | m |
| ν_t | Eddy viscosity | m^2/s |
| τ_{ij} | Stress | m^2/s^2 |
| Ω | Horizontal domain enclosed by boundary $\delta\Omega$ | m^2 |

Acronyms/Abbreviations

| Symbol | Description |
|---------------|------------------------------------|
| NSWE | Non-linear shallow water equations |
| XBeach | Extreme Beach behaviour model |
| LES | Large eddy simulation |
| FOU | First order upwind |
| CFL | Courant-Friedrichs-Levy |
| DTP | Dynamic Tidal Power |
| ADV | Acoustic Doppler Velocimeter |
| LDV | Laser Doppler Velocimeter |
| DFT | Discrete Fourier Transform |
| FFT | Fast Fourier Transform |

Bibliography

- Arthur, R.S., 1962. A Note on the Dynamics of Rip Currents. *Journal of Geophysical Research*, 67(7): 2777-2779.
- Basco, D.R., 1983. Surfzone currents. *Coastal Engineering*, 7: 331-355.
- Battjes, J.A., 1988. Surf-Zone Dynamics. *Annual Review Fluid Mechanics*, 20: 257-293.
- Battjes, J.A., Sobey, R.J. and Stive, M.J.F., 1990. Nearshore circulation. *Sea Ocean Engineering Science*, A(9): 467-493.
- Boers, M., 2005. Surf Zone Turbulence, Delft University of Technology, Delft.
- Bowen, A.J., 1969. Rip Currents: 1. Theoretical Investigations. *Journal of Geophysical Research*, 74(23): 5467-5478.
- Bowen, A.J. and Inman, D.L., 1969. Rip Currents: 2. Laboratory and Field Observations. *Journal of Geophysical Research*, 74(23): 5479-5490.
- Chen, Q., Dalrymple, R.A., Kirby, J.T., Kennedey, A.B. and Haller, M.C., 1999. Boussinesq modeling of a rip current system. *Journal of Geophysical Research*, 104: 20617-20637.
- Dalrymple, R.A. and Lozano, C.J., 1978. Wave-Current Interaction Models for Rip Currents. *Journal of Geophysical Research*, 83(C12): 6063-6071.
- Dingemans, M.W., 1997. Water wave propagation over uneven bottom. World scientific publishing, Singapore.
- Drønen, N., Karunarathna, H., Fredsøe, J., Mutlu Sumer, B. and Deigaard, R., 2002. An experimental study of rip channel flow. *Coastal Engineering*, 45(3-4): 223-238.
- Ebersole, B.A. and Dalrymple, R.A., 1979. A numerical model for nearshore circulation including convective accelerations and lateral mixing. *Ocean Engineering*, Rep. 21.
- Haas, K.A., Svendsen, I.A., Haller, M.C. and Zhao, Q., 2003. Quasi-three-dimensional modeling of rip current systems. *Journal of geophysical research*, 108(C7): 10 - 1 / 10 - 21.
- Haller, M.C., Dalrymple, R.A. and Svendsen, I.A., 2002. Experimental study of nearshore dynamics on a barred beach with rip channels. *Journal of geophysical research*, 107(C6).
- Hamm, L., 1992. Directional Nearshore Wave Propagation Over a Rip Channel: An Experiment, *Coastal Engineering*.
- Harlow, F.H. and Welsh, J.E., 1965. Numerical Calculation of Time-Dependent Viscous Incompressible Flow of Fluid with Free Surface. *The Physics of Fluids*, 8(12): 2182 - 2189.
- Hibberd, S. and Peregrine, D.H., 1979. Surf and run-up on a beach: a uniform bore. *Journal of Fluid Mechanics Digital Archive*, 02(95): 323-345.
- Hirsch, C., 2007. *Numerical Computation of internal and external flows*. Wiley, New York.
- Hirt, C.W. and Nichols, B.D., 1981. Volume of Fluid (VOF) Method for the Dynamics of Free Boundaries*. *Journal of Computational Physics*(39): 201-225.
- Holthuijsen, L.H., 2007. *Waves in Oceanic and Coastal Waters*. Cambridge University Press, Delft University of Technology
- UNESCO-IHE.
- Lascody, R.L., 1998. East central Florida rip current program. National Weather Service In-House Report: 10.
- LeBlond, P.H. and Tang, C.L., 1974. On Energy Coupling Between Waves and Rip Currents. *Journal of Geophysical Research*, 79(6): 811-816.
- Longuet-Higgins, M.S., 1953. Mass transport in water waves. *Phil. Trans Roy. Soc., A*(245): 535-581.
- Longuet-Higgins, M.S. and Stewart, R.W., 1964. Radiation stress in water waves, a physical discussion with applications. *Deep-sea Res.*, 11(4): 529-563.
- Luschine, J.B., 1991. A study of rip current drownings and weather related factors. *Natl. Weather Dig.*: 13-19.

- MacCormack, R.W., 1969. The effect of viscosity in hypervelocity impact cratering. AIAA Hyper Velocity Impact Conference, Paper 69 - 354.
- MacMahan, J.H., Reniers, A.J.H.M., Thornton, E.B. and Stanton, T.P., 2004. Infragravity rip current pulsations. *Journal of Geophysical research*, 109(C01033).
- MacMahan, J.H., Thornton, E.B. and Reniers, A.J.H.M., 2006. Rip current review. *Coastal Engineering*, 53: 191-208.
- Madsen, P.A. and Sørensen, O.R., 1992. A new form of the Boussinesq equations with improved linear dispersion characteristics. Part 2: a slowly-varying bathymetry. *Coastal Engineering*, 18(3-4): 183-205.
- Madsen, P.A., Sørensen, O.R. and Schäffer, H.A., 1997a. Surf zone dynamics simulated by a Boussinesq type model. Part I. Model description and cross-shore motion of regular waves. *Coastal Engineering*, 32: 255-287.
- Madsen, P.A., Sørensen, O.R. and Schäffer, H.A., 1997b. Surf zone dynamics simulated by a Boussinesq type model. Part II: surf beat and swash oscillations for wave groups and irregular waves. *Coastal Engineering*, 32: 289-319.
- Mei, C.C. and Liu, P.L.-F., 1977. Effects of Topography on the Circulation In and Near the Surf Zone - Linear Theory. *Estuarine and Coastal Marine Science*, 5: 25-37.
- Munk, W.H., 1949. The solitary wave theory and its application to surf problems. *Annals of the New York Academy of Sciences*, 51(Ocean Surface Waves): 376-424.
- Peregrine, D.H., 1967. Long waves on a beach. *Journal Fluid Mechanics*, 27: 817-834.
- Peregrine, D.H. and Svendsen, I.A., 1978. Spilling Breakers, Bores and Hydraulic Jumps. *Coastal Engineering*: 540-550.
- Roelvink, J.A. et al., 2009. Modelling storm impacts on beaches, dunes and barrier islands. *Coastal Engineering*, 56: 1133 - 1152.
- Shepard, F.P. and Inman, D.L., 1950. Nearshore circulation related to bottom topography and wave refraction. *Trans. Amer. Geophys. Union*, 31(4): 555-565.
- Shepard, F.P. and Inman, D.L., 1951. Nearshore circulation, *Proceedings of the 1st Conference of Coastal Engineering*, pp. 50-59.
- Shepard, F.P., O., E.K. and LaFond, E.C., 1941. Rip Currents: A process of geological importance. *Journal Geology*, 49(4): 337-369.
- Short, A.D., 1999. Beach hazards and safety, *Beach and Shoreface Morphodynamics*. John Wiley and Sons, Chichester, pp. 292-304.
- Smagorinsky, J., 1963. General Circulation experiments with the primitive equations. *Monthly Weather Review*, 91(3): 99-164.
- Smit, P.B., 2008. Non-hydrostatic modelling of large scale tsunamis, Delft University of Technology.
- Sørensen, O.R., Schäffer, H.A. and Madsen, P.A., 1998. Surf zone dynamics simulated by a Boussinesq type model. III. Wave-induced horizontal nearshore circulations. *Coastal Engineering*, 33: 155-176.
- Stelling, G.S. and Duinmeijer, S.P.A., 2003. A staggered conservative scheme for every Froude number in rapidly varied shallow water flows. *International Journal for Numerical Methods in Fluids*, 1(43): 1-23.
- Stelling, G.S. and Zijlema, M., 2003. An accurate and efficient finite-difference algorithm for non-hydrostatic free-surface flow with application to wave propagation. *International Journal for Numerical Methods in Fluids*(43): 1-23.
- Svendsen, I.A., 2006. *Introduction to Nearshore Hydrodynamics*. World Scientific Publishing Co Pte. Ltd., Singapore.
- Tome, M.F. and Mckee, S., 1994. GENSMAC: A computational Marker and Cell Method for Free Surface Flows in General Domains. *Journal of Computational Physics*(110): 171-186.
- Van Dongeren, A.R.V. and Svendsen, I.A., 1997. Absorbing-Generating Boundary Condition for Shallow Water Models. *Journal of Waterway, Port, Coastal, and Ocean Engineering*, 126(6): 303-313.
- Wei, G., Kirby, J.T., Grilli, S.T. and Subramanya, R., 1995. A fully nonlinear Boussinesq model for surface waves, 1, Highly nonlinear unsteady waves. *Journal Fluid Mechanics*, 294: 71-92.

- Wilmott, C.J., 1981. On the validation of models. *Physical Geography*, 2: 184 - 194.
- Wind, H.G. and Vreugdenhil, C.B., 1986. Rip-current generation near structures. *Journal Fluid Mechanics*, 171: 459-476.
- Wu, C.S. and Liu, P.L.-F., 1982. Finite element modelling of breaking wave-induced nearshore current. In: Kawai, T. (Ed.), *Finite Element Flow Analysis*: 579-586.
- Zijlema, M. and Stelling, G.S., 2005. Further experiences with computing non-hydrostatic free-surface flows involving water waves. *International Journal for Numerical Methods in Fluids*, 48: 169-197.
- Zijlema, M. and Stelling, G.S., 2008. Efficient computation of surf zone waves using the nonlinear shallow water equations with non-hydrostatic pressure. *Coastal Engineering*(55): 780-790.

Appendices

A Nearshore hydropower

A.1 Introduction

In this thesis an investigation has been made into the hydrodynamics of the nearshore zone. The study of nearshore dynamics is important for coastline developments, harbors and inlets. Additionally there is another reason why nearshore hydrodynamics and specifically wave induced currents are interesting and should therefore be investigated and modelled. As energy consumption is rising and fossil fuels are diminishing, and global warming is more and more on the agenda of politicians and policymakers, the world is searching for a renewable energy source that can sustain the rising energy consumption of the world's population. Wind, waves and sunlight are all natural phenomena that contain energy which could be harvested. Waves have about 5 times the energy density of wind but it has proven difficult to extract this energy from waves. In an effective rip current system a part of the wave energy is transformed into a current velocity, the so called rip current. Apparently, it is much more effective to extract the energy out of a current, so therefore it could be worthwhile to research how strong rip currents are formed and if these currents are stable enough for energy extraction.

Also other ways in which wave motions are transformed into a current can be interesting for energy extraction methods from the ocean. For example, tidal power plants can be made more effective by also directing the short wave induced currents into the tidal turbines. This will add to the current flow of the tidal difference between the offshore and inshore side of the tidal dam.

The numerical model XBeach, with the addition of a Smagorinsky subgrid model, as verified in this thesis appears to be able to reproduce most of the physical relevant processes in a rip current system reasonably well. Therefore this model can be used to find ways of utilizing the wave induced current velocity for energy extraction methods. In this Appendix the numerical model XBeach is applied for a brief investigation into the possible energy potential in a wave induced nearshore zone current.

A.2 Rip current

From chapters 2 and 5 we can deduce that there are mechanisms in a rip current system that decrease the strength and give the current a pulsating behavior. Also, due to vortex shedding, the current changes in direction and strength. So a way to increase the current's strength and make the current more suitable for energy extraction is to cancel out these mechanisms.

The wave-current interaction within the rip current channel decreases the current strength, due to the heightening of the waves which causes the waves to break earlier, which in turn decreases the longshore wave-setup gradient from within the rip channel to just outside the rip channel. This is the main driver of the current and therefore this mechanism should be eliminated in order to increase the current. A way of doing this is to block the incoming waves that enter the rip channel which therefore cancels out the wave-current interaction in the rip channel. The

wave-current interaction is also known to give the current a pulsating behavior, which is therefore also eliminated.

Vortex shedding, as we have seen in Paragraph 5.2, constantly changes the direction of the current, which as a consequence makes it rather difficult to extract energy out of the current. Therefore we should also try to obstruct this mechanism. Figure A-1 shows that vertical walls have been strategically placed in the topography of the rip current experiment of *Haller et. al* (2002) to achieve this.

The amended topography results in a stronger rip current without the vortex shedding. In order to extract energy from this current a turbine should be placed in the narrowest part of the rip channel, where current velocities are at their highest. The average velocity compared with the experiment's mean velocity has increased to more than twice the value. In order for this system to work the bathymetry has to be fixed so that erosion of the bottom cannot occur. Otherwise the bottom may be modified by erosion which would change the dynamics. In Figure A-1 the mean flow field is given with the amended topography.

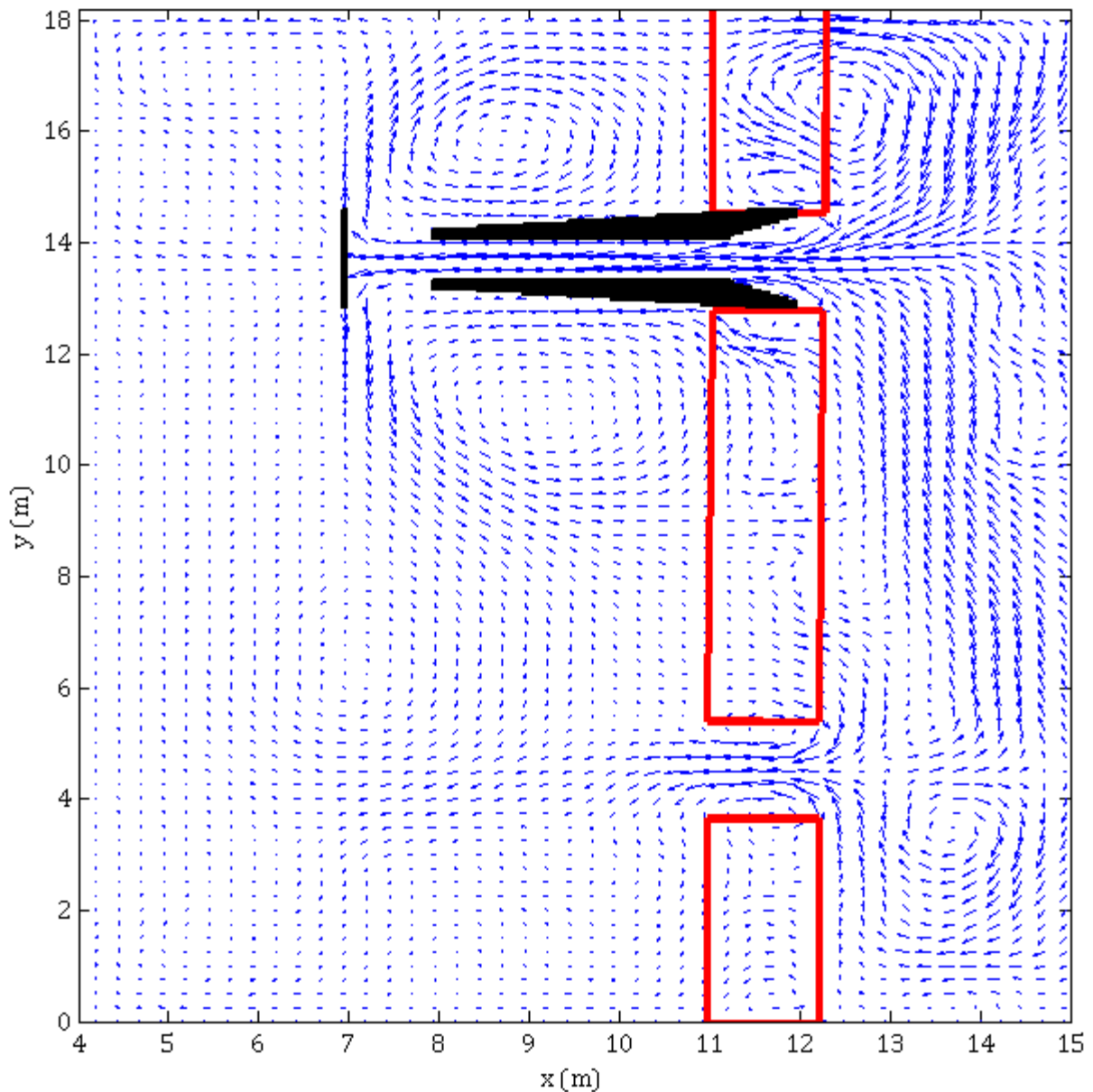


Figure A-1: Run averaged flow field with amended topography

In the above figure one can see that more velocity vectors behind the breaker bar are directed towards the upper rip channel. This results in a higher mass flux through the channel and due to the narrower channel the velocities are therefore even higher still. In Figure A-2 the cross-shore currents at the longshore sections at the offshore side of the breaker bar and more seaward from the bar are compared to the results from the simulation without the amended topography. It can be seen that the mean cross-shore current between the walls in the rip channel has significantly increased compared to the mean current without the walls. Also, at the more seaward section, the mean current is still much higher due to the inability of the current to meander. This can be seen in Figure A-3 where the wave averaged flow velocities are shown together with the vorticity.

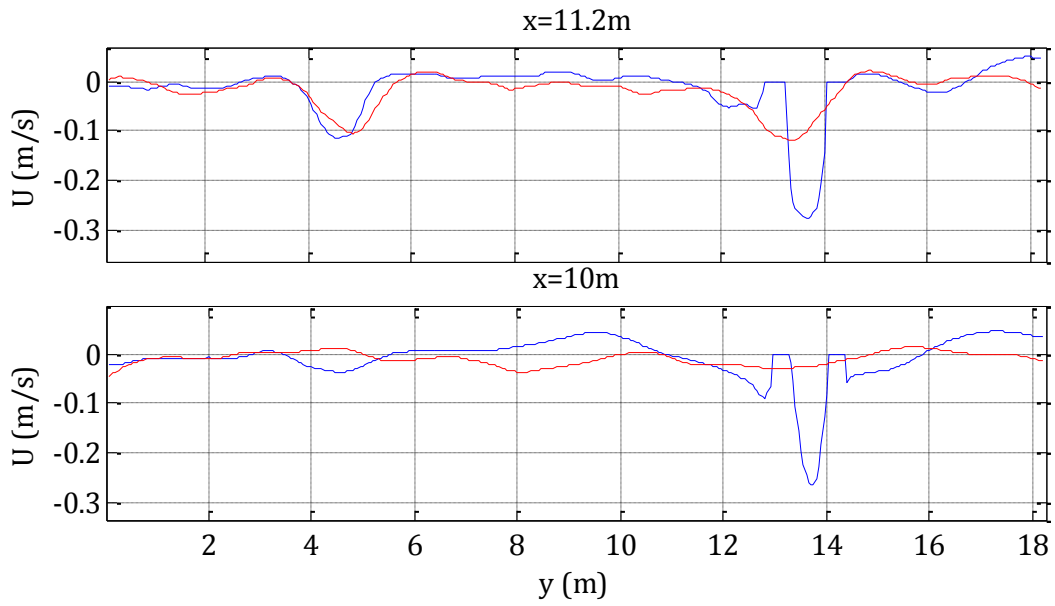


Figure A-2: Comparison of time-averaged modelled cross-shore currents with amended topography (blue line) to modelled cross-shore currents with original topography (red line)

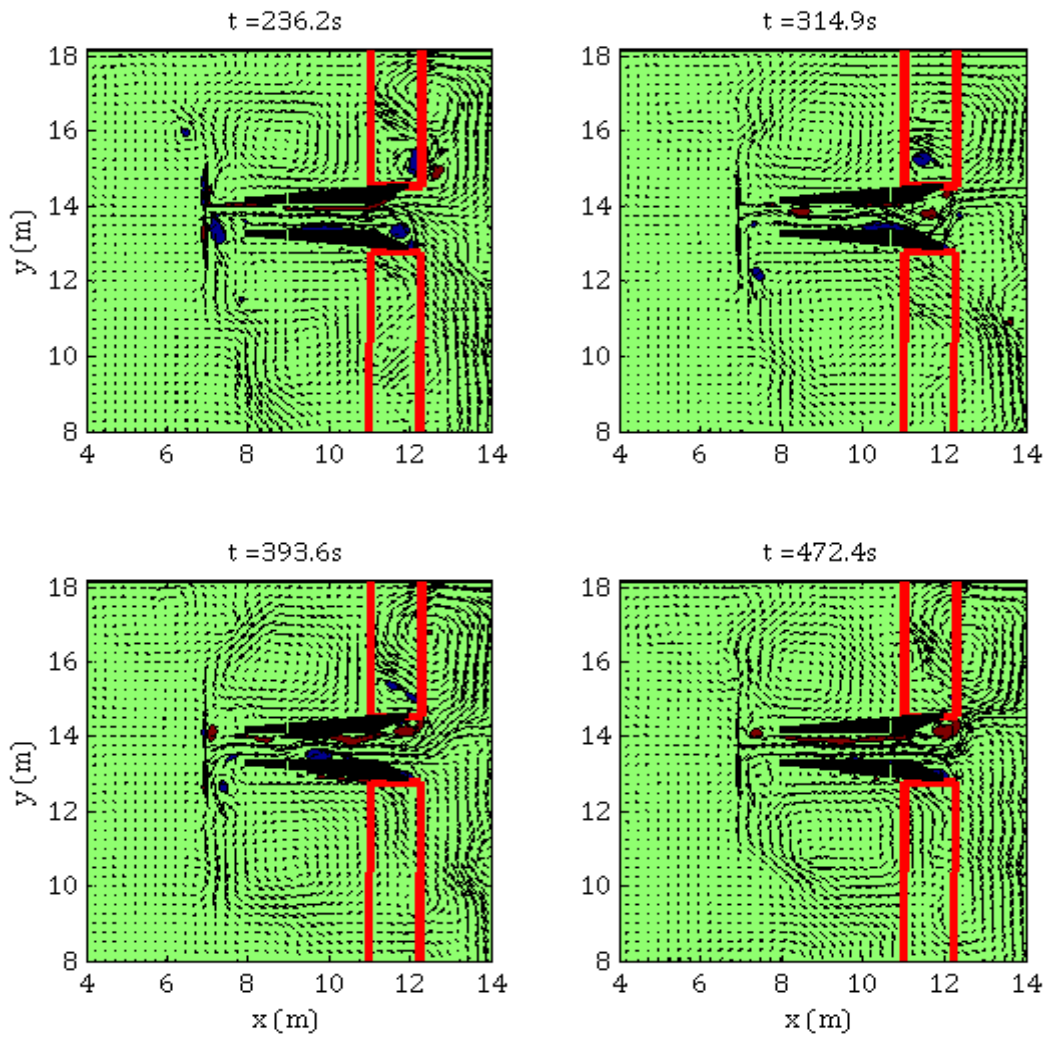


Figure A-3: Snapshots of vorticity and velocity vectors averaged over two wave periods from the simulation. Red represents negative and blue represents positive vorticity. Only the upper half of the computational domain is shown

It can be seen from Figure A-3 that the flow is steadier and that the vorticity in the flow field is mainly present in the rip channel. Therefore the vortex shedding of the flow is contained within the channel. This results in a higher mass flux through the channel due to the fact that less water is flowing back over the breaker bar.

In Figure A-4 the longshore currents with the amended topography are much higher and are more directed towards the upper rip channel. This thus indicates that more water mass is being fed into the rip channel resulting in a higher mass flux through the channel.

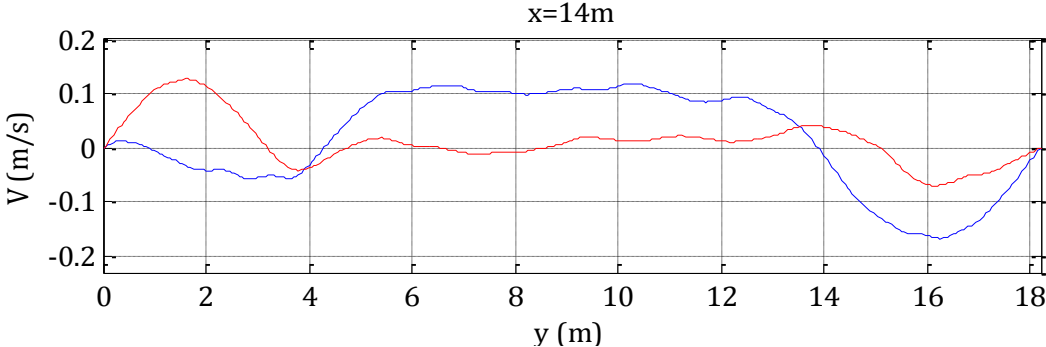


Figure A-4: Comparison of time averaged modelled longshore currents with amended topography (blue line) to modelled longshore currents with original topography (red line)

In Figure A-5 a comparison is made between the mean wave height at the longshore sections at the offshore side of the breaker bar and more seaward from the bar. It can clearly be seen that the waves are blocked due to the walls and thus reducing the wave height in the channel. Due to the gap at both sides diffraction will cause the waves to impinge into the channel. Thus the wave current interaction is still present in the rip channel, however due to lower wave height in the channel the mechanism is substantially reduced.

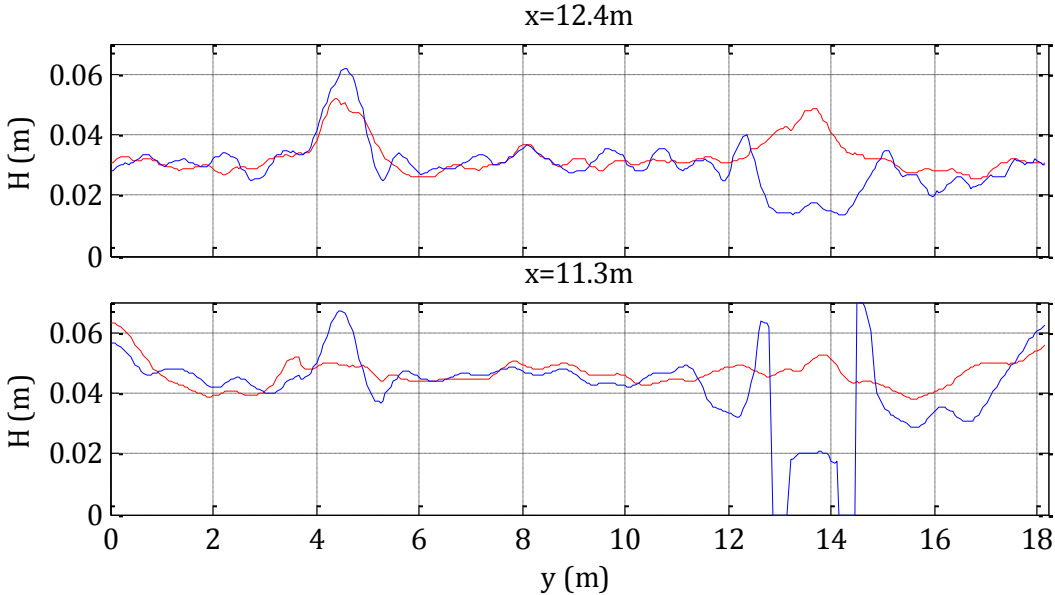


Figure A-5: Comparison of time-averaged modelled wave height with amended topography (blue line) to modelled wave height with original topography (red line)

Spacing of the rip current is also of importance for its strength. If the spacing between two rip channels is increased a stronger current is usually induced. In Figure A-6 the average flow field is shown with a single channel instead of two, thus increasing the length of the breaker bar of which the mass flux that is transported over the bar is directed back through the rip channel. In Figure A-7, however, one can see that the flow velocity is not increased compared to the case with two channels.

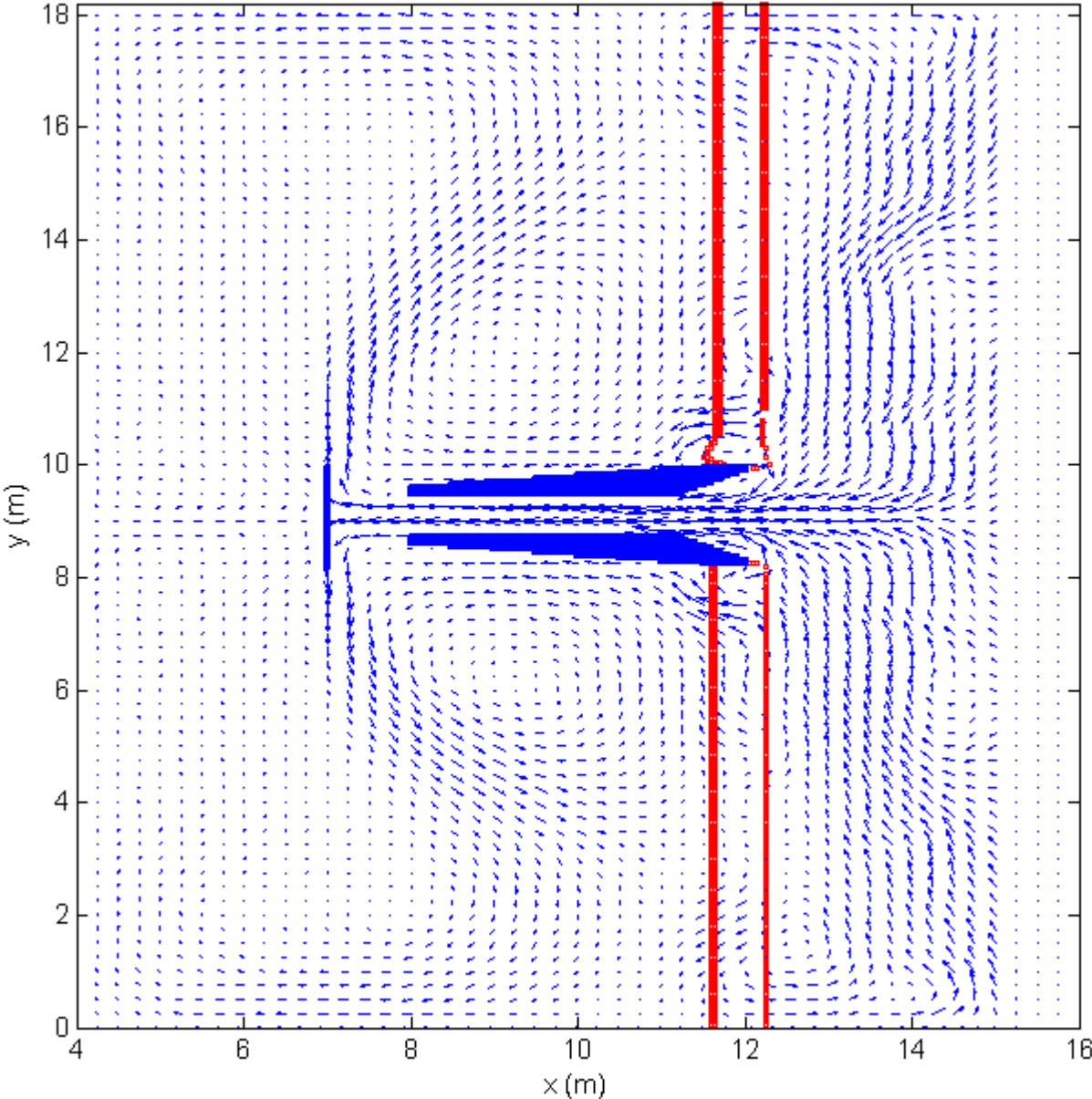


Figure A-6: run averaged flow with single rip channel

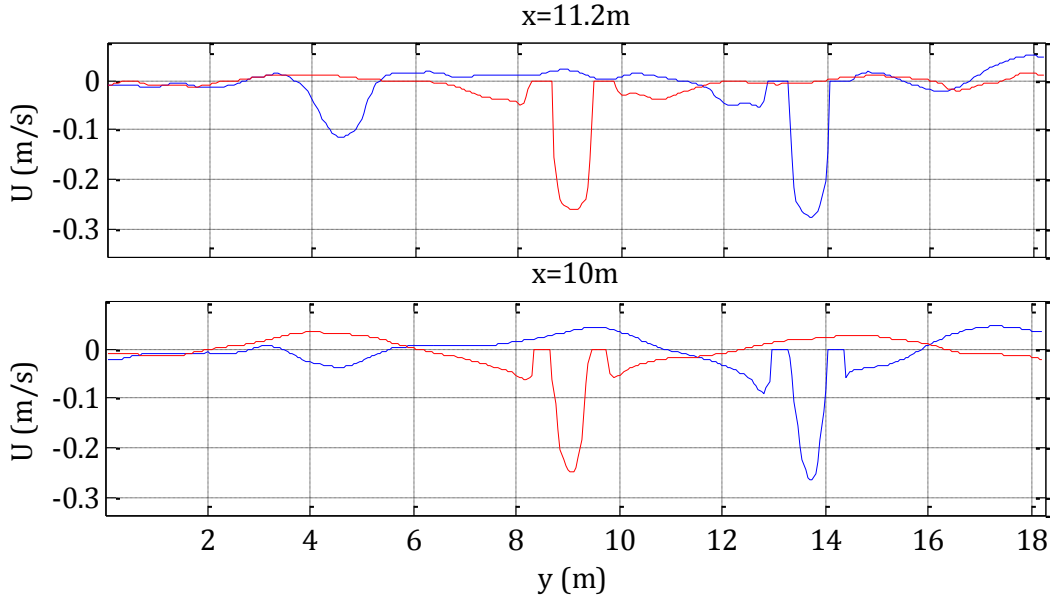


Figure A-7: Comparison of time-averaged modelled cross-shore currents with amended topography with two channels (blue line) to modelled cross-shore currents with single channel (red line)

It should be noted that the above results are for a comparison with the experiments of *Haller et al.* (2002) and that in real situations the waves are not monochromatic. Furthermore, the tides change the water level and thus the dynamics of the rip current system.

A part of the kinetic energy that is present in the rip current could be extracted with the help of a turbine. The energy available in the rip current can be expressed as:

$$P = \frac{\rho A V^3}{2} \quad (\text{A.1})$$

Where P = the power generated (in watts), ρ = the density of the water (in kg/m^3), A = the sweep area of the turbine (in m^2) and U = the velocity of the flow.

In the case above with a single rip channel and a wave height of 4.75 cm at the seaward boundary the available power in the rip channel is about 0.82 watt. This is not much, however this is a scaled down rip current system in a wave basin. If we consider the experiment, and thus the computation, as an undistorted Froude model of field conditions with a length scale ratio of 1/50, then the conditions correspond to a rip spacing of 450 m, rip channel width of 90 m, breaking wave heights of 1.3 – 3.8 m, wave periods of 5.7 – 7.1 s, and a mean rip velocity of about 1.5 m/s in the first case, and with the amended topography the mean rip velocity turns out to be about 4 m/s. The potential power in the rip channel then amounts to more than 3 MW. However, only a part can be extracted but it can be worthwhile to further investigate the energy potential in a rip current system.

In Table 1 one can see the scales of rip current systems in the field. We have seen that the mean rip velocity can be more than doubled with the strategic placement of walls that reduce the vortex shedding and the wave current interaction. The rip current can be further increased with tapered walls reducing the width of the rip channel to increase the flow rate in the channel.

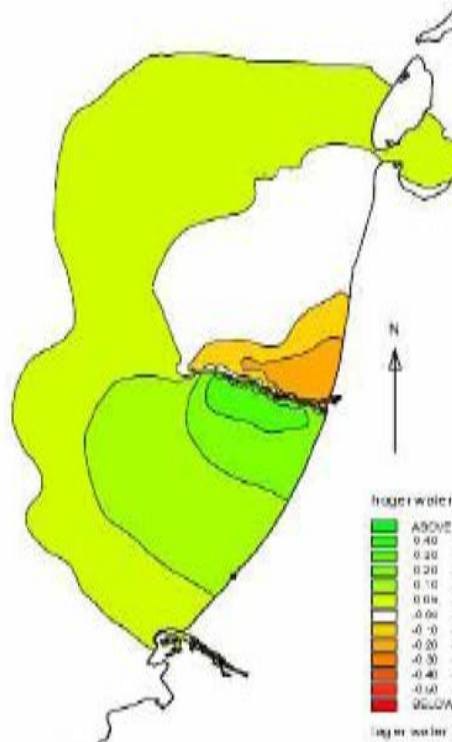
Taking the field characteristics of the rip current system at Palm Beach, Australia and reducing the width of the channel to 5 m instead of 60 m gives a mean flow velocity of about 5 m/s. The available power in such a channel will be about 550 kW. However there are still many uncertainties if this is realizable. Nonetheless it could be worthwhile to investigate this further and use numerical models to see if these flow rates can be achieved. It could be a good way of harnessing the power of the ocean waves.

A.3 Tidal power

Another form of hydropower from the ocean is tidal power which converts the energy of tides into electricity. Although not yet widely used, tidal power has potential for future electricity generation. A new concept for tidal power, invented and patented in 1997 by Dutch coastal engineers Kees Hulsbergen and Rob Steijn, called Dynamic Tidal Power (DTP), involves the construction of very long dams of about 30 to 50 km, extending from the coast straight out into the ocean, with a perpendicular barrier at the far end, forming a large 'T' shape. This long T-dam interferes with coast-parallel oscillating tidal waves which run along the coasts of continental shelves. The oscillating pattern in which these tidal currents flow every day will naturally cause the water level to rise significantly on the one side of the dam and to drop on the other side. Later in the day the situation reverses. The maximum water level differential will be about 2–3 meters in a typical coastal region, mainly depending on the length of the dam, and the level of acceleration of the local tidal currents. The head is converted into power using a long series of turbines installed in the dam.

These Dynamic Tidal Power dams can also utilize the short wave energy that is available along the dam by focusing the wave-setup into the turbines. The head that is created due to the wave-setup is in addition to the head created by the tidal wave, but only if the wind waves propagate approximately in the same direction as the tidal wave. This way the DTP dam can be made more profitable. Furthermore, wind turbines can be placed alongside the dam, where wind is more constant and stronger than onshore, and, in contrast to offshore wind farms, the wind turbines would be easier to maintain and operate.

Economic viability is estimated to be reached for dam lengths of about 30 km. In Figure A-8 the results are shown of a numerical study undertaken by UNESCO-IHE for a DTP dam at IJmuiden perpendicular to the coastline into the North Sea. The information about this dam is taken from <http://www.ca-oe.org>.



Dynamic Tidal Power (DTP) at IJmuiden

- Installed power 1000 MW (440 turbines)
- Annual production 4.6 TWh
- Turbines € 1000 /kW
- Caissons (for turbines) € 1500 /kW
- Dam section (without turbines) € 3 billion
- Development cost 10%
- Interest during construction 10%
- 'Green' interest 4% per year
- Write off in 30 years
- Net internal rate of return 10% per year
- Subsidy 20% ('Kyoto and beyond')
- Exploitation cost € 0.015/kWh

Figure A-8: Water level differences due to presence of a 30 km long dam at IJmuiden during MHW and spring tide (UNESCO-IHE)

A.4 Conclusion

From the investigation in A.2 can be concluded that the mean current velocity can significantly be increased by reducing the negative feedback mechanisms. By doing this a more steady flow can be realized. Also the mean current velocity is substantially increased. However if rip currents can be utilized for electricity generation is still questionable. A quick calculation shows that existing rip current systems have an energy potential of more than 1 MW and from the simulation it was even deduced that the rip current could contain more than 3 MW. However the viability of this idea is questionable. Further investigation should be undertaken to answer these questions.

Wave induced could supplement existing tidal power dams by creating a higher water level differential due to the wave setup of the short waves, which will increase the profitability of these dams. Further investigation and modelling is needed if this can significantly increase power output. Also rip currents can be made much stronger by changing the bathymetry in the rip current system. However, extensive modelling is needed to know if these currents provide for an economic viable power plant. The next step would be to model a real world rip current. Subsequently it can be investigated if this rip current can be made steady and strong enough. One should also take into consideration the morphological processes that play a role in these systems. The numerical model XBeach could also be used for this consideration.

In the coming years numerical models can be used for the research of ocean and wave energy systems, wherein a power take system is implemented. Numerical modelling is also needed to optimize the structures of these systems. However tests in a hydraulic laboratory are still required to verify numerical calculations with these new implementations.

B Derivation of the depth averaged equations

B.1 Introduction

Two physical principles are used for the derivation of the underlying equations of fluid flow in the field of fluid mechanics. Those two principles are the conservation of momentum and mass. The conservation of momentum leads to the well known Navier-Stokes equations and the conservation of mass leads to the continuity equation.

B.2 Navier-Stokes equations

The Navier–Stokes equations describe the motion of substances that can flow. These equations arise from applying Newton's second law to fluid motion, together with the assumption that the fluid stress is the sum of a diffusing viscous term (proportional to the gradient of velocity), plus a pressure term.

It is assumed that the reader has seen the derivation of the Navier-Stokes equations many times and it is therefore not repeated here.

The Navier-Stokes equations are given by:

$$\begin{aligned}\frac{\partial \rho u}{\partial t} + \frac{\partial \rho u^2}{\partial x} + \frac{\partial \rho v u}{\partial y} + \frac{\partial \rho w u}{\partial z} &= -\frac{\partial P}{\partial x} + \eta \Delta u \\ \frac{\partial \rho v}{\partial t} + \frac{\partial \rho u v}{\partial x} + \frac{\partial \rho v^2}{\partial y} + \frac{\partial \rho w v}{\partial z} &= -\frac{\partial P}{\partial y} + \eta \Delta v \\ \frac{\partial \rho w}{\partial t} + \frac{\partial \rho u w}{\partial x} + \frac{\partial \rho v w}{\partial y} + \frac{\partial \rho w^2}{\partial z} &= -\frac{\partial P}{\partial z} + \eta \Delta w - \rho g\end{aligned}\tag{B.1}$$

Where u , v and w denote the velocity components in the x -, y - and z -direction respectively, ρ the fluid density, P the pressure, η the dynamic viscosity, g is the gravitational acceleration (which only acts in the z -direction) and Δ the Laplacian.

The Navier-Stokes equations are usually accompanied with the conservation of mass equation. This equation is described as follows.

$$\frac{\partial \rho}{\partial t} + \frac{\partial(\rho u)}{\partial x} + \frac{\partial(\rho v)}{\partial y} + \frac{\partial(\rho w)}{\partial z} = 0\tag{B.2}$$

Equations (B.1) and (B.2) describe a wide range of flows found, for both gases and fluids. But these equations are highly non-linear and very difficult (read computationally very expensive) to solve.

B.3 Simplifications

A less accurate but computationally less expensive way of solving (approximating) the Navier-Stokes equations and the continuity equation is to simplify the equations with some basic

assumptions that can be justified for the case at hand. Our area of interest lies in the coastal zone of oceans and seas. This justifies some assumptions with regard to the fluid. The fluid density is relatively constant in this relatively small region of the oceans and seas, and therefore the assumption can be made that the fluid is homogeneous. Secondly the fluid is almost incompressible and therefore the second assumption is an incompressible fluid. These two assumptions can already greatly simplify the equations, and thus make it more manageable to find approximate solutions for these equations in the nearshore zone with grid sizes up to 1 million nodes.

When the flow is steady, ρ does not change with respect to time, and when the flow is incompressible, ρ is constant and does not change with respect to space. The conservation of mass reduces to the conservation of volume. The following equation will be referred to as the local continuity equation:

$$\frac{\partial u}{\partial x} + \frac{\partial v}{\partial y} + \frac{\partial w}{\partial z} = 0 \quad (\text{B.3})$$

And using the assumptions outlined in this paragraph we are also able to simplify the Navier-Stokes equations in (B.1) to the following equations. Treating the density as a constant in space and time leads to the incompressible Navier-Stokes equations

$$\frac{D\mathbf{u}}{Dt} = -\frac{1}{\rho} \nabla P + \nu \Delta \mathbf{u} - \mathbf{g} \quad (\text{B.4})$$

In equation (B.4) ν is the kinematic viscosity defined as the ratio between the dynamic viscosity and the density. The vector \mathbf{u} and \mathbf{g} are defined as follows.

$$\mathbf{u} = \begin{pmatrix} u \\ v \\ w \end{pmatrix}, \quad \mathbf{g} = \begin{pmatrix} 0 \\ 0 \\ g \end{pmatrix}$$

B.4 Pressure decomposition

In equation (B.4) the total pressure is used. This pressure consists of a hydrostatic component and a hydrodynamic component. In deep water the hydrostatic component is by far the larger part of the total pressure. In shallow water, however, the depth is not that large and the hydrodynamic component, due to the waves, has a larger contribution to the total pressure. As we are interested in the surf zone dynamics, we cannot afford to lose this component in our equations. To include the hydrodynamic component we can decompose the total pressure into the hydrostatic and the hydrodynamic part.

$$P = p_h + p_d = \rho g(\zeta - z) + \rho p \quad (\text{B.5})$$

Where p_d is the dynamic pressure, p_h is the hydrostatic part of the pressure, ζ is the free surface and p is the dynamic pressure normalized with the density ρ . The pressure at the surface is zero in (B.5). Substituting (B.5) into (B.4) gives:

$$\begin{aligned}
\frac{Du}{Dt} &= -g \frac{\partial \zeta}{\partial x} - \frac{\partial p}{\partial x} + \nu \Delta u \\
\frac{Dv}{Dt} &= -g \frac{\partial \zeta}{\partial y} - \frac{\partial p}{\partial y} + \nu \Delta v \\
\frac{Dw}{Dt} &= \frac{\partial p}{\partial z} + \nu \Delta w
\end{aligned}
\tag{B.6}$$

Except for the dynamic pressure component and the viscous terms in these equations, they are the same as the well known non-linear shallow water equations.

B.5 Free surface equation

The model has to describe the free surface and the depth integrated velocity. The approach to describe the free surface is to use a single valued function for the free surface. This does not allow for the overturning of waves, and the dissipation effect of this phenomenon is considered as a subgrid effect that has to be captured by a proper conservation principle. In this approach the following coordinate system is used, where from the $z = 0$ line ζ is the value of the free surface positive upwards, d is the value of the bottom positive downwards and H is the total water depth defined by $H = \zeta + d$ (See Figure B-9).

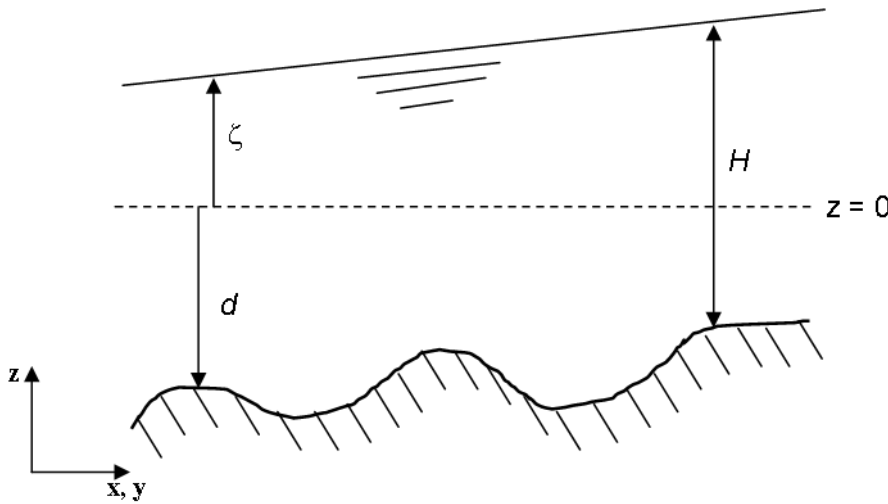


Figure B-9: Coordinate system used

To obtain the free surface equation the continuity equation is integrated over the total depth:

$$\int_{-d}^{\zeta} \nabla \cdot \mathbf{u} dz = \int_{-d}^{\zeta} \frac{\partial u}{\partial x} dz + \int_{-d}^{\zeta} \frac{\partial v}{\partial y} dz + w(x, y, \zeta, t) - w(x, y, -d, t) = 0
\tag{B.7}$$

It is assumed that the water surface always consists of the same particles. This assumption is justified when no overturning of waves, due to wave breaking is considered. This is not the case when plunging waves occur but nevertheless it is a necessary assumption for this numerical scheme to work. With the overturning of waves very complex shapes of water surface can occur, and, due to the mixing of water and air, it is also hard to define the exact interface between water and air. Therefore this assumption is applied. It is however possible to allow for the

overturning of waves and to include the effect of the mixing of air and water, but then different numerical models should be used. These models are usually based on the Marker and Cell scheme (e.g. *Harlow and Welsh, 1965; Tome and Mckee, 1994*) or the Volume of Fluid method (e.g. *Hirt and Nichols, 1981*), however they have to resolve very small scales in both time and space. This makes large scale application impossible and therefore the above method is chosen.

The vertical velocity of a particle located at the free surface is equal to the material derivative of the free surface elevation:

$$w(x, y, \zeta, t) = \frac{D\zeta}{Dt} = \frac{\partial\zeta}{\partial t} + u \frac{\partial\zeta}{\partial x} + v \frac{\partial\zeta}{\partial y} \quad (\text{B.8})$$

The vertical velocity of a particle at the bottom is equal to the material derivative of the bottom elevation. However, the time derivative of the bottom elevation is zero because it is assumed that the bottom does not change over time. This is not the case when morphological processes are considered, but even in this case the changes in time of the bottom profile are very slow compared to the changes in time of the surface profile due to the large difference in timescale of the two processes. The kinematic boundary condition at the bottom is given by

$$w(x, y, -d, t) = -u \frac{\partial d}{\partial x} - v \frac{\partial d}{\partial y} \quad (\text{B.9})$$

When equations (B.8) and (B.9) are substituted into equation (B.7) and use is made of the Leibniz rule of integration, the integrated continuity equation is written as follows

$$\frac{\partial\zeta}{\partial t} + \frac{\partial UH}{\partial x} + \frac{\partial VH}{\partial y} = 0 \quad (\text{B.10})$$

Where U and V are the depth averaged velocities given by

$$U = \frac{1}{H} \int_{-d}^{\zeta} u dz, V = \frac{1}{H} \int_{-d}^{\zeta} v dz \quad (\text{B.11})$$

Equation (B.10) is the global continuity equation for the depth averaged model, which gives a relation between the surface elevation and the velocity.

B.6 Depth averaged momentum equations

The depth averaged momentum equations are derived by means of integration of the momentum equations (B.6) over the water depth H . Because the procedure for each of the three momentum equations is very similar only the u -momentum equation will be described in detail.

The u -momentum equation in component form is written as follows

$$\underbrace{\frac{\partial u}{\partial t}}_{\text{time derivative}} + \underbrace{\left(\frac{\partial u^2}{\partial x} + \frac{\partial uv}{\partial y} + \frac{\partial uw}{\partial z} \right)}_{\text{advective terms}} = -\underbrace{g \left(\frac{\partial\zeta}{\partial x} - \frac{\partial p}{\partial x} \right)}_{\text{pressure terms}} + \underbrace{\frac{1}{\rho} \left(\frac{\partial\tau_{xx}}{\partial x} + \frac{\partial\tau_{yx}}{\partial y} + \frac{\partial\tau_{zx}}{\partial z} \right)}_{\text{turbulent stress terms}} \quad (\text{B.12})$$

This equation is integrated over the depth and for clarity we can consider the following contributions separately: (i) the time derivative, (ii) the advective terms, (iii) the pressure terms, (iv) the turbulent stress terms. First the time derivative will be integrated.

$$\int_{-d}^{\zeta} \frac{\partial u}{\partial t} dz = \frac{\partial}{\partial t} (HU) - u \frac{\partial \zeta}{\partial t} + u \frac{\partial d}{\partial t} \quad (\text{B.13})$$

The second and third term on the right hand side are a result of the movement of the free surface and the bottom in time. In our case the bottom is stationary and will not change in time, so the third term is zero. Integrating the advective terms gives:

$$\int_{-d}^{\zeta} \left(\frac{\partial u^2}{\partial x} + \frac{\partial uv}{\partial y} + \frac{\partial uw}{\partial z} \right) dz = \frac{\partial}{\partial x} \left(HU^2 - \int_{-d}^{\zeta} (u-U) dz \right) - \frac{\partial}{\partial y} \left(HUV - \int_{-d}^{\zeta} (u-U)(v-V) dz \right) - u \left[u \frac{\partial z}{\partial x} + v \frac{\partial z}{\partial y} + w \right]_{z=-d}^{z=\zeta} \quad (\text{B.14})$$

The terms on the right side of the equation with the integrals are dispersion terms due to the non-uniformities in the flow in the vertical. When the vertical distribution of the flow is close to uniform and therefore does not deviate much from the average flow velocity, these contributions are small. The dispersion terms will give diffusion to the momentum equations because the vertical distribution is unknown in a depth averaged model. The last term is due to the application of the Leibniz rule and when combined with (B.13) these boundary terms cancel out.

The integration of the hydrostatic pressure term is straightforward and is as follows

$$\int_{-d}^{\zeta} \left(g \frac{\partial \zeta}{\partial x} \right) dz = gH \frac{\partial \zeta}{\partial x} \quad (\text{B.15})$$

The vertical integration of the dynamic pressure term was already treated in Chapter 4.

Finally integrating the turbulent stress terms results in

$$\frac{1}{\rho} \int_{-d}^{\zeta} \left(\frac{\partial \tau_{xx}}{\partial x} + \frac{\partial \tau_{yx}}{\partial y} + \frac{\partial \tau_{zx}}{\partial z} \right) dz = \frac{1}{\rho} \frac{\partial}{\partial x} (H \bar{\tau}_{xx}) + \frac{1}{\rho} \frac{\partial}{\partial y} (H \bar{\tau}_{yx}) + \frac{\tau_{sx}}{\rho} - \frac{\tau_{bx}}{\rho} \quad (\text{B.16})$$

The stresses at the surface and bottom are included in τ_{sx} and τ_{bx} respectively. The stress term at the surface τ_{sx} due to e.g. wind was not used and is therefore left out of the following equations. In equation (B.14) the terms involving the integral and the terms involving the vertical gradient of the horizontal flow are unknown in the depth averaged model, and are therefore left out of the equation. Then by combining the equations (B.13), (B.14), (B.15) and (B.16) the depth integrated u -momentum equation reads in conservative form:

$$\begin{aligned} \frac{\partial}{\partial t}(HU) + \frac{\partial}{\partial x}(HU^2) + \frac{\partial}{\partial y}(HUV) + gH \frac{\partial \zeta}{\partial x} + \int_{-d}^{\zeta} \frac{\partial p}{\partial x} dz = \\ + \frac{1}{\rho} \frac{\partial}{\partial x}(H\bar{\tau}_{xx}) + \frac{1}{\rho} \frac{\partial}{\partial y}(H\bar{\tau}_{yx}) - \frac{\tau_{bx}}{\rho} \end{aligned} \quad (\text{B.17})$$

This equation can be written in non-conservative form with the velocity in x-direction as the primitive variable. This is required to calculate the velocity in the velocity points. To show that the non-conservative form is fully equivalent to the conservative form, the non-conservative u -momentum equation is derived from (B.17).

Making use of the product rule, equation (B.17) is written with only the time derivative and advective terms as

$$H \frac{\partial U}{\partial t} + U \frac{\partial H}{\partial t} + HU \frac{\partial U}{\partial x} + U \frac{\partial HU}{\partial x} + HV \frac{\partial U}{\partial y} + U \frac{\partial HV}{\partial y} = \text{Rest terms} \quad (\text{B.18})$$

The continuity equation (B.10) is then substituted into equation (B.18) and the equation is divided by H . The full u -momentum in non-conservative form then reads

$$\frac{\partial U}{\partial t} + U \frac{\partial U}{\partial x} + V \frac{\partial U}{\partial y} + g \frac{\partial \zeta}{\partial x} + \frac{1}{H} \int_{-d}^{\zeta} \frac{\partial p}{\partial x} dz = \frac{1}{\rho H} \frac{\partial H\bar{\tau}_{xx}}{\partial x} + \frac{1}{\rho H} \frac{\partial H\bar{\tau}_{xy}}{\partial y} - \frac{\tau_{bx}}{\rho H} \quad (\text{B.19})$$

The terms on the right hand side of the equation involving the derivatives of τ_{xx} and τ_{yx} are the viscous contributions. Using a similar derivation as for the x-direction the depth integrated equations in the y- and z-direction read in conservative form:

$$\begin{aligned} \frac{\partial}{\partial t}(HV) + \frac{\partial}{\partial x}(HUV) + \frac{\partial}{\partial y}(HV^2) + gH \frac{\partial \zeta}{\partial x} + \int_{-d}^{\zeta} \frac{\partial p}{\partial x} dz = \\ + \frac{1}{\rho} \frac{\partial}{\partial x}(H\bar{\tau}_{xy}) + \frac{1}{\rho} \frac{\partial}{\partial y}(H\bar{\tau}_{yy}) + \frac{\tau_{sy}}{\rho} - \frac{\tau_{by}}{\rho} \end{aligned} \quad (\text{B.20})$$

$$\frac{\partial}{\partial t}(HW) + \frac{\partial}{\partial x}(HUW) + \frac{\partial}{\partial y}(H VW) + (p|_{\zeta} - p|_{-d}) = \frac{1}{\rho} \frac{\partial}{\partial x}(H\bar{\tau}_{xz}) + \frac{1}{\rho} \frac{\partial}{\partial y}(H\bar{\tau}_{yz}) \quad (\text{B.21})$$

And again using the product rule equations (B.20) and (B.21) read in non-conservative form, as they are given in Chapter 4:

$$\frac{\partial V}{\partial t} + V \frac{\partial V}{\partial x} + U \frac{\partial V}{\partial y} + g \frac{\partial \zeta}{\partial y} + \frac{1}{H} \int_{-d}^{\zeta} \frac{\partial p}{\partial y} dz = \frac{1}{\rho H} \frac{\partial H\bar{\tau}_{yx}}{\partial x} + \frac{1}{\rho H} \frac{\partial H\bar{\tau}_{yy}}{\partial y} - \frac{\tau_{bx}}{\rho H} \quad (\text{B.22})$$

$$\frac{\partial W}{\partial t} + U \frac{\partial W}{\partial x} + V \frac{\partial W}{\partial y} + \frac{1}{H} (p|_{\zeta} - p|_{-d}) = \frac{1}{\rho H} \frac{\partial H\bar{\tau}_{xz}}{\partial x} + \frac{1}{\rho H} \frac{\partial H\bar{\tau}_{yz}}{\partial y} \quad (\text{B.23})$$

C Discretisation

This Appendix is concerned with the description of the numerical approximation of the depth averaged model XBeach.

C.1 Global continuity equation

As was outlined in Appendix B.5 the global continuity equation, which describes the relation between the free surface and the depth averaged discharge, is given by

$$\frac{\partial \zeta}{\partial t} + \frac{\partial}{\partial x}(UH) + \frac{\partial}{\partial y}(VH) = 0 \quad (\text{C.1})$$

A simple discretisation of (C.1) using central differences for the space derivatives and using the Hansen scheme for the time derivative gives:

$$\frac{\zeta_{i,j}^{n+1} - \zeta_{i,j}^n}{\Delta t} + \frac{{}^x q_{i+\frac{1}{2},j}^n - {}^x q_{i-\frac{1}{2},j}^n}{\Delta x} + \frac{{}^y q_{i,j+\frac{1}{2}}^n - {}^y q_{i,j-\frac{1}{2}}^n}{\Delta y} = 0 \quad (\text{C.2})$$

With ${}^x q_{i+\frac{1}{2},j}^n = U_{i+\frac{1}{2},j}^{n+\frac{1}{2}} H_{i+\frac{1}{2},j}^n$, ${}^y q_{i,j+\frac{1}{2}}^n = V_{i,j+\frac{1}{2}}^{n+\frac{1}{2}} H_{i,j+\frac{1}{2}}^n$. The water depth is not defined at the velocity points and thus needs to be interpolated from surrounding points. We use a simple first order accurate upwind interpolation

$$H_{i+\frac{1}{2},j}^n = \begin{cases} \zeta_{i,j}^n + \max(d_i, d_{i+1}) & \text{if } U_{i+\frac{1}{2},j}^{n+\frac{1}{2}} > 0 \\ \zeta_{i+1,j}^n + \max(d_i, d_{i+1}) & \text{if } U_{i+\frac{1}{2},j}^{n+\frac{1}{2}} < 0 \\ \max(\zeta_{i,j}^n, \zeta_{i+1,j}^n) + d_{i+\frac{1}{2}} & \text{if } U_{i+\frac{1}{2},j}^{n+\frac{1}{2}} = 0 \end{cases} \quad (\text{C.3})$$

This makes the scheme first order accurate due to the first order accurate upwind interpolations and continuity equation. To increase the accuracy of the scheme $\zeta_{i,j}^{n+1}$ can be set to $\zeta_{i,j}^{n*}$. The first order prediction will then be corrected using the MacCormack scheme. The corrector step reads

$$\frac{\zeta_{i,j}^{n+1} - \zeta_{i,j}^{n*}}{\Delta t} + \frac{{}^x \Delta q_{i+\frac{1}{2},j}^n - {}^x \Delta q_{i-\frac{1}{2},j}^n}{\Delta x} + \frac{{}^y \Delta q_{i,j+\frac{1}{2}}^n - {}^y \Delta q_{i,j-\frac{1}{2}}^n}{\Delta y} = 0 \quad (\text{C.4})$$

In which ${}^x \Delta q_{i+\frac{1}{2},j}^n = U_{i+\frac{1}{2},j}^{n+\frac{1}{2}} \Delta H_{i+\frac{1}{2},j}^{n*}$ and $\Delta H_{i+\frac{1}{2},j}^{n*}$ is given by

$$\Delta H_{i+\frac{1}{2},j}^{n*} = \begin{cases} \frac{1}{2}\psi \left(\frac{\zeta_{i,j}^{n*} - \zeta_{i-1,j}^n}{\zeta_{i+1,j}^{n*} - \zeta_{i,j}^n} \right) (\zeta_{i+1,j}^{n*} - \zeta_{i,j}^n) & \text{if } U_{i+\frac{1}{2},j}^{n+\frac{1}{2}} > 0 \\ \frac{1}{2}\psi \left(\frac{\zeta_{i+2,j}^n - \zeta_{i+1,j}^{n*}}{\zeta_{i+1,j}^n - \zeta_{i,j}^{n*}} \right) (\zeta_{i+1,j}^n - \zeta_{i,j}^{n*}) & \text{if } U_{i+\frac{1}{2},j}^{n+\frac{1}{2}} < 0 \\ 0 & \text{if } U_{i+\frac{1}{2},j}^{n+\frac{1}{2}} = 0 \end{cases} \quad (\text{C.5})$$

In here ψ denotes the minmod limiter, which is defined as

$$\psi(r) = \begin{cases} \min(r, 1) & \text{if } r > 0 \\ 0 & \text{if } r \leq 0 \end{cases} \quad (\text{C.6})$$

In which r is the ratio of the upwind and downwind gradient of the free surface. A more comprehensive description of the minmod limiter can be found in *Hirsch (2007)*.

The predictor-corrector set is second order accurate in areas where the solution is smooth and where discontinuities occur the method reduces to first order accurate.

C.2 Local continuity equation

The depth averaged local continuity equation is given by

$$\frac{\partial HU}{\partial x} + \frac{\partial HV}{\partial y} + w \Big|_{z=\zeta} - U \frac{\partial z}{\partial x} \Big|_{z=\zeta} - V \frac{\partial z}{\partial y} \Big|_{z=\zeta} = 0 \quad (\text{C.7})$$

This equation is discretized using a central difference scheme

$$\frac{H_{i+\frac{1}{2},j}^{n+1} U_{i+\frac{1}{2},j}^{n+\frac{1}{2}} - H_{i-\frac{1}{2},j}^{n+1} U_{i-\frac{1}{2},j}^{n+\frac{1}{2}}}{\Delta x} + \frac{H_{i,j+\frac{1}{2}}^{n+1} V_{i,j+\frac{1}{2}}^{n+\frac{1}{2}} - H_{i,j-\frac{1}{2}}^{n+1} V_{i,j-\frac{1}{2}}^{n+\frac{1}{2}}}{\Delta y} - w_{i,j,s}^{n+\frac{1}{2}} - \bar{U}_{i,j}^{n+\frac{1}{2}} \frac{\zeta_{i+\frac{1}{2},j}^{n+1} - \zeta_{i-\frac{1}{2},j}^{n+1}}{\Delta x} - \bar{V}_{i,j}^{n+\frac{1}{2}} \frac{\zeta_{i,j+\frac{1}{2}}^{n+1} - \zeta_{i,j-\frac{1}{2}}^{n+1}}{\Delta y} = 0 \quad (\text{C.8})$$

The surface elevation variables at the cell faces are approximated with upwind interpolations. The local continuity equation is used to setup a discrete set of Poisson-type equations in which the pressures are the only unknown quantities.

C.3 Horizontal momentum equations

The discretisation of the depth-averaged horizontal momentum equations can be done with an upwind approach which makes the scheme first order accurate. However, to improve accuracy, a correction step according to the MacCormack scheme (*MacCormack, 1969*) can be used to make the method second order accurate. The hydrostatic pressure is integrated using a midpoint rule and central differences, while the source terms are integrated using an explicit Euler time integration. We will only treat the u -momentum equation in detail as the procedure for the momentum equations in the other two directions is very similar.

Predictor step

The depth averaged horizontal u -momentum equation is discretized as follows

$$\begin{aligned} & \frac{(HU)_{i+\frac{1}{2},j}^* - (HU)_{i+\frac{1}{2},j}^{n+\frac{1}{2}}}{\Delta t} + \frac{x \bar{q}_{i+1,j}^{n+\frac{1}{2}} U_{i+1,j}^{n+\frac{1}{2}} - x \bar{q}_{i,j}^{n+\frac{1}{2}} U_{i,j}^{n+\frac{1}{2}}}{\Delta x} + \frac{y \bar{q}_{i+\frac{1}{2},j+\frac{1}{2}}^{n+\frac{1}{2}} U_{i+\frac{1}{2},j+\frac{1}{2}}^{n+\frac{1}{2}} - y \bar{q}_{i+\frac{1}{2},j-\frac{1}{2}}^{n+\frac{1}{2}} U_{i+\frac{1}{2},j-\frac{1}{2}}^{n+\frac{1}{2}}}{\Delta y} \\ & + g \frac{(H^2)_{i+1,j}^{n+1} - (H^2)_{i,j}^{n+1}}{2\Delta x} = g \bar{H}_{i+\frac{1}{2},j}^n \frac{d_{i+\frac{1}{2},j} - d_{i-\frac{1}{2},j}}{\Delta x} + {}^u \text{Pr}_{i+\frac{1}{2},j}^{n+\frac{1}{2}} + {}^u S_{i+\frac{1}{2},j}^{n+\frac{1}{2}} + {}^u T_{i+\frac{1}{2},j}^{n+\frac{1}{2}} \end{aligned} \quad (\text{C.9})$$

The discretisation of the dynamic pressure is denoted by Pr , in T the effects of the viscosity are included and S includes all other source terms. The discretisation of the viscosity terms are done by central differences:

$$\begin{aligned} {}^u T_{i+\frac{1}{2},j}^{n+\frac{1}{2}} = & \frac{2}{\Delta x_{i+\frac{1}{2}}} \left[v_{i+\frac{1}{2},j}^n H_{i+\frac{1}{2},j}^{n+1} \frac{U_{i+1\frac{1}{2},j}^{n+\frac{1}{2}} - U_{i+\frac{1}{2},j}^{n+\frac{1}{2}}}{\Delta x_{i+1}} - v_{i-\frac{1}{2},j}^n H_{i-\frac{1}{2},j}^{n+1} \frac{U_{i+\frac{1}{2},j}^{n+\frac{1}{2}} - U_{i-\frac{1}{2},j}^{n+\frac{1}{2}}}{\Delta x_i} \right] \\ & + \frac{1}{\Delta y_j} \left[\bar{v}_{i+\frac{1}{2}}^n \bar{H}_{i+\frac{1}{2},j}^{n+1} \frac{U_{i+1\frac{1}{2},j}^{n+\frac{1}{2}} - U_{i+\frac{1}{2},j}^{n+\frac{1}{2}}}{\Delta y_{i+\frac{1}{2}}} - \bar{v}_{i-\frac{1}{2},j}^n \bar{H}_{i-\frac{1}{2},j}^{n+1} \frac{U_{i+1\frac{1}{2},j}^{n+\frac{1}{2}} - U_{i-\frac{1}{2},j}^{n+\frac{1}{2}}}{\Delta y_{i-\frac{1}{2}}} \right] \\ & + \frac{1}{\Delta x_j} \left[\bar{v}_{i+\frac{1}{2}}^n \bar{H}_{i+\frac{1}{2},j}^{n+1} \frac{V_{i+1,j+\frac{1}{2}}^{n+\frac{1}{2}} - V_{i,j+\frac{1}{2}}^{n+\frac{1}{2}}}{\Delta x_{i+\frac{1}{2}}} - \bar{v}_{i-\frac{1}{2},j}^n \bar{H}_{i-\frac{1}{2},j}^{n+1} \frac{V_{i+1,j-\frac{1}{2}}^{n+\frac{1}{2}} - V_{i,j-\frac{1}{2}}^{n+\frac{1}{2}}}{\Delta x_{i+\frac{1}{2}}} \right] \end{aligned} \quad (\text{C.10})$$

Here $\bar{v}_{i+\frac{1}{2},j}^n$ and $\bar{H}_{i+\frac{1}{2},j}^{n+1}$ are obtained by interpolation from surrounding points.

Equation (C.9) is formulated with the depth averaged momentum as the primitive variable and not the velocity. To formulate (C.9) in terms of U the method by *Steling and Duinmeijer (2003)* is used.

The u -momentum equation is then written as

$$\begin{aligned} & \frac{U_{i+\frac{1}{2},j}^* - U_{i+\frac{1}{2},j}^{n+\frac{1}{2}}}{\Delta t} + \frac{x \bar{q}_{i+1,j}^{n+\frac{1}{2}} U_{i+1,j}^{n+\frac{1}{2}} - x \bar{q}_{i,j}^{n+\frac{1}{2}} U_{i,j}^{n+\frac{1}{2}}}{\bar{H}_{i+\frac{1}{2},j}^{n+1} \Delta x} + \frac{y \bar{q}_{i,j+\frac{1}{2}}^{n+\frac{1}{2}} U_{i,j+\frac{1}{2}}^{n+\frac{1}{2}} - y \bar{q}_{i,j}^{n+\frac{1}{2}} U_{i,j}^{n+\frac{1}{2}}}{\bar{H}_{i+\frac{1}{2},j}^{n+1} \Delta y} - \frac{U_{i+\frac{1}{2},j+\frac{1}{2}}^{n+\frac{1}{2}}}{\bar{H}_{i+\frac{1}{2},j}^{n+1}} \frac{x \bar{q}_{i+1,j}^{n+\frac{1}{2}} - x \bar{q}_{i,j}^{n+\frac{1}{2}}}{\Delta x} \\ & - \frac{U_{i+\frac{1}{2},j-\frac{1}{2}}^{n+\frac{1}{2}}}{\bar{H}_{i+\frac{1}{2},j}^{n+1}} \frac{y \bar{q}_{i,j+\frac{1}{2}}^{n+\frac{1}{2}} - y \bar{q}_{i,j}^{n+\frac{1}{2}}}{\Delta y} + g \frac{\zeta_{i+1,j}^{n+1} - \zeta_{i,j}^{n+1}}{\Delta x} = \frac{{}^u \text{Pr}_{i+\frac{1}{2},j}^{n+\frac{1}{2}} + {}^u S_{i+\frac{1}{2},j}^{n+\frac{1}{2}} + {}^u T_{i+\frac{1}{2},j}^{n+\frac{1}{2}}}{\bar{H}_{i+\frac{1}{2},j}^{n+1}} \end{aligned} \quad (\text{C.11})$$

In which $\bar{H}_{i+\frac{1}{2},j}^{n+1} = \frac{1}{2}(H_{i+1,j}^{n+1} + H_{i,j}^{n+1})$ and $\bar{q}_{i,j}^{n+\frac{1}{2}} = \frac{1}{2}(q_{i+\frac{1}{2},j}^{n+\frac{1}{2}} + q_{i-\frac{1}{2},j}^{n+\frac{1}{2}})$

The dynamic pressure term Pr does not have a separate evolution equation in time, as such the pressure term cannot be calculated explicitly using values from the previous time level. However to improve accuracy of the predictor step the pressure term is included explicitly. The pressure term is decomposed into two terms as:

$$p_{i,j}^{n+\frac{1}{2}} = p_{i,j}^{n+\frac{1}{2}} + \Delta p_{i,j}^{n+\frac{1}{2}} \quad (\text{C.12})$$

In the predictor step the pressure term is included using $p_{i,j}^{n+\frac{1}{2}}$. In the corrector step the Poisson equation is solved for $\Delta p_{i,j}^{n+\frac{1}{2}}$. The pressure term in the predictor step is given by:

$${}^u \text{Pr}_{i+\frac{1}{2},j}^{n+\frac{1}{2}} = \frac{H_{i+1,j}^{n+1} \bar{p}_{i+1,j}^{n+\frac{1}{2}} - H_{i,j}^{n+1} \bar{p}_{i,j}^{n+\frac{1}{2}}}{\Delta x} - p_{i+\frac{1}{2},j}^{n+\frac{1}{2}} \frac{d_{i+\frac{1}{2},j} - d_{i-\frac{1}{2},j}}{\Delta x} = \frac{(\zeta_{i+1,j}^{n+1} + d_{i,j}^{n+1}) p_{i+1,j}^{n+\frac{1}{2}} - (\zeta_{i,j}^{n+1} + d_{i+1,j}^{n+1}) p_{i,j}^{n+\frac{1}{2}}}{2\Delta x} \quad (\text{C.13})$$

Here $\bar{p}_{i+1,j}^{n+\frac{1}{2}}$ represents the average pressure over the vertical which is approximated with $\bar{p}_{i+1,j}^{n+\frac{1}{2}} = \frac{1}{2} p_{i+1,j}^{n+\frac{1}{2}}$, in which $p_{i+1,j}^{n+\frac{1}{2}}$ is the pressure at the bottom. Furthermore $p_{i+\frac{1}{2},j}^{n+\frac{1}{2}}$ is defined as $p_{i+\frac{1}{2},j}^{n+\frac{1}{2}} = \frac{1}{2} (p_{i+1,j}^{n+\frac{1}{2}} + p_{i,j}^{n+\frac{1}{2}})$.

Corrector step

The corrector step is used to make the scheme second order accurate. First order accuracy suffers from significant numerical damping, which is fine in regions where damping due to turbulence is expected like e.g. in the surf zone, but outside the surf zone, in deeper water, waves propagate without much energy loss and here numerical damping is not at all wanted.

The corrector step formulated in terms of average velocity is given by:

$$\begin{aligned} & \frac{U_{i+\frac{1}{2},j}^{n+\frac{1}{2}} - U_{i+\frac{1}{2},j}^{n*}}{\Delta t} + \frac{x \bar{q}_{i+1,j}^{n+\frac{1}{2}} \Delta U_{i+1,j}^{n*} - x \bar{q}_{i,j}^{n+\frac{1}{2}} \Delta U_{i,j}^{n*}}{\bar{H}_{i+\frac{1}{2},j}^{n+1} \Delta x} + \frac{y \bar{q}_{i,j+1}^{n+\frac{1}{2}} \Delta U_{i,j+1}^{n*} - y \bar{q}_{i,j}^{n+\frac{1}{2}} \Delta U_{i,j}^{n*}}{\bar{H}_{i+\frac{1}{2},j}^{n+1} \Delta y} + \dots \\ & \dots + \frac{(\zeta_{i+1,j}^{n+1} + d_{i+1,j}^{n+1}) \Delta p_{i+1,j}^{n+\frac{1}{2}} - (\zeta_{i,j}^{n+1} + d_{i,j}^{n+1}) \Delta p_{i,j}^{n+\frac{1}{2}}}{2\bar{H}_{i+\frac{1}{2},j}^{n+1} \Delta x} = 0 \end{aligned} \quad (\text{C.14})$$

The values of $\Delta U_{i,j}^{n*}$ are obtained with minmod limiter equivalent to equation (C.5)

C.4 Vertical momentum equation

The vertical momentum equation is discretized in a similar manner to the horizontal equations using the MacCormack scheme. In terms of the depth averaged vertical velocity the predictor step is:

$$\begin{aligned} & \frac{\bar{W}_{i,j}^* - \bar{W}_{i,j}^{n+\frac{1}{2}}}{\Delta t} + \frac{x q_{i+\frac{1}{2},j}^{n+\frac{1}{2}} \bar{W}_{i+\frac{1}{2},j}^{n+\frac{1}{2}} - x q_{i-\frac{1}{2},j}^{n+\frac{1}{2}} \bar{W}_{i-\frac{1}{2},j}^{n+\frac{1}{2}}}{H_{i,j}^{n+1} \Delta x} - \frac{\bar{W}_{i,j}^{n+\frac{1}{2}}}{H_{i,j}^{n+1}} \frac{x q_{i+\frac{1}{2},j}^{n+\frac{1}{2}} - x q_{i-\frac{1}{2},j}^{n+\frac{1}{2}}}{\Delta x} - \frac{y q_{i,j+\frac{1}{2}}^{n+\frac{1}{2}} \bar{W}_{i,j+\frac{1}{2}}^{n+\frac{1}{2}} - y q_{i,j-\frac{1}{2}}^{n+\frac{1}{2}} \bar{W}_{i,j-\frac{1}{2}}^{n+\frac{1}{2}}}{H_{i,j}^{n+1} \Delta y} \\ & \frac{\bar{W}_{i,j}^{n+\frac{1}{2}}}{H_{i,j}^{n+1}} \frac{y q_{i,j+\frac{1}{2}}^{n+\frac{1}{2}} - y q_{i,j-\frac{1}{2}}^{n+\frac{1}{2}}}{\Delta y} + \frac{p_{i,j,s}^{n+\frac{1}{2}} - p_{i,j,b}^{n+\frac{1}{2}}}{H_{i,j}^{n+1}} = \frac{w S_{i,j}^{n+\frac{1}{2}} + w T_{i,j}^{n+\frac{1}{2}}}{H_{i,j}^{n+1}} \end{aligned} \quad (\text{C.15})$$

The pressures are defined at the cell faces and therefore do not have to be interpolated. Furthermore the pressure at the surface can exactly be set to zero. The vertical velocities are defined on the cell faces and therefore the depth averaged velocity $\bar{W}_{i,j}^{n+\frac{1}{2}}$ needs to be expressed in terms of the bottom and surface velocities. Using a simple central approximation gives

$$\bar{W}_{i,j}^{n+\frac{1}{2}} = \frac{1}{2}(\bar{W}_{i,j,s}^{n+\frac{1}{2}} - \bar{W}_{i,j,b}^{n+\frac{1}{2}}), \quad \bar{W}_{i,j}^* = \frac{1}{2}(\bar{W}_{i,j,s}^* - \bar{W}_{i,j,b}^*) \quad (\text{C.16})$$

At the bottom the kinematic boundary condition is used for the vertical velocity:

$$W_{i,j,b}^* = \frac{1}{2}(U_{i+\frac{1}{2},j}^* + U_{i-\frac{1}{2},j}^*) \frac{d_{i+\frac{1}{2},j} - d_{i-\frac{1}{2},j}}{\Delta x} + \frac{1}{2}(V_{i,j+\frac{1}{2}}^* + V_{i,j-\frac{1}{2}}^*) \frac{d_{i,j+\frac{1}{2}} - d_{i,j-\frac{1}{2}}}{\Delta y} \quad (\text{C.17})$$

A first order upwind approach is taken for the interpolation of $\bar{W}_{i+\frac{1}{2},j}^{n+\frac{1}{2}}$ and $\bar{W}_{i,j+\frac{1}{2}}^{n+\frac{1}{2}}$. The turbulent stresses are again approximated using a central difference scheme as

$$\begin{aligned} w \mathbf{T}_{i+\frac{1}{2},j}^{n+\frac{1}{2}} = & \frac{1}{\Delta x_i} \left[x \bar{V}_{i+\frac{1}{2},j}^n x \bar{H}_{i+\frac{1}{2},j}^{n+1} \frac{W_{i+1,j}^{n+\frac{1}{2}} - W_{i,j}^{n+\frac{1}{2}}}{\Delta x_{i+\frac{1}{2}}} - x \bar{V}_{i-\frac{1}{2},j}^n x \bar{H}_{i-\frac{1}{2},j}^{n+1} \frac{W_{i,j}^{n+\frac{1}{2}} - W_{i-1,j}^{n+\frac{1}{2}}}{\Delta x_{i+\frac{1}{2}}} \right] \\ & + \frac{1}{\Delta y_i} \left[y \bar{V}_{i,j+\frac{1}{2}}^n y \bar{H}_{i,j+\frac{1}{2}}^{n+1} \frac{W_{i,j+1}^{n+\frac{1}{2}} - W_{i,j}^{n+\frac{1}{2}}}{\Delta x_{j+\frac{1}{2}}} - y \bar{V}_{i,j-\frac{1}{2}}^n y \bar{H}_{i,j-\frac{1}{2}}^{n+1} \frac{W_{i,j}^{n+\frac{1}{2}} - W_{i,j-1}^{n+\frac{1}{2}}}{\Delta y_{j+\frac{1}{2}}} \right] \end{aligned} \quad (\text{C.18})$$

By combining (C.15), (C.16) and (C.17) explicit expression for $W_{i,j,s}^*$ and $W_{i,j,b}^*$ obtained.

Corrector

The predicted values are again corrected using a MacCormack scheme and including the pressure difference implicitly gives the corrector step:

$$\frac{\bar{W}_{i,j}^{n+\frac{1}{2}} - \bar{W}_{i,j,s}^*}{\Delta t} + \frac{x q_{i+\frac{1}{2},j}^{n+\frac{1}{2}} \Delta \bar{W}_{i+\frac{1}{2},j}^* - x q_{i-\frac{1}{2},j}^{n+\frac{1}{2}} \Delta \bar{W}_{i-\frac{1}{2},j}^*}{H_{i,j}^{n+1} \Delta x} + \frac{y q_{i,j+\frac{1}{2}}^{n+\frac{1}{2}} \Delta \bar{W}_{i,j+\frac{1}{2}}^* - y q_{i,j-\frac{1}{2}}^{n+\frac{1}{2}} \Delta \bar{W}_{i,j-\frac{1}{2}}^*}{H_{i,j}^{n+1} \Delta y} - \frac{\Delta p_{i,j}^{n+\frac{1}{2}}}{H_{i,j}^{n+1}} = 0 \quad (\text{C.19})$$

Where $\Delta W_{i+\frac{1}{2},j}^*$ and $\Delta W_{i,j+\frac{1}{2}}^*$ are obtained using a similar relation as in (C.5).

The discrete vertical momentum balance of (C.15) and (C.19) looks very different from the relations found in *Zijlema and Stelling* (2005; 2008). This is mainly due to the application of the MacCormack scheme for the advection. The discretisation of the pressure term is equivalent to the Keller box scheme as used in *Zijlema and Stelling* (2005; 2008)